Measurement of the triple gauge boson couplings from W pair production in ALEPH[1]

Gonzalo Merino
Universitat Autònoma de Barcelona
Departament de Física
Edifici Cn E-08193 Bellaterra (Barcelona)

July 2000

[1]Ph.D. Dissertation

Contents

List of Figures

List of Tables

Chapter 1

Introduction

Since the electromagnetic and weak forces were first combined in a consistent theory in the 60s by Glashow, Weinberg and Salam [1], the predictions of the Standard Model (SM) of electroweak interactions have been tested and confirmed by several experiments. During the past decade, two electron-positron colliders dramatically improved our understanding of electroweak interactions. The LEP storage ring at CERN, which produced millions of Z^0 bosons during its first operational phase (LEP1) from 1989 to 1995, and the SLC linear collider at SLAC, which produced fewer Z^0 bosons but it allowed experiments with polarised beams. For the first time it was possible to perform precision measurements of the fundamental parameters of the SM, which could then be used to test the very fundamental structure of the SM as a quantum field theory.

A second phase in the experimental programme of LEP (LEP2) started in the summer of 1996, when the centre of mass energy was increased up to the W pair production threshold in order to study the details of the SM bosonic sector. One of the main goals of LEP2 is the precise measurement of the W mass, since it can be used to constrain the allowed values of the mass of the Higgs boson in the context of the SM. W pair production provides also very important information of the structure of the predicted interactions among the electroweak gauge bosons, which are the most fundamental signature of a non-abelian gauge symmetry. These interactions are described by the triple gauge boson vertices γWW and ZWW and an accurate measurement of their associated couplings represents an essential test of the SM. The boson pair production reactions which take place at LEP2 are very sensitive to these couplings, and this sensitivity gets higher as the centre of mass energy increases.

In this thesis, the triple gauge boson couplings (TGC) are measured using semileptonic (electron and muon) as well as purely hadronic W pair decays selected from the data

sample collected by ALEPH during the year 1998 at a centre of mass energy of 189 GeV. Anomalous TGCs affect both the total W pair production cross section and the shape of the differential cross section as a function of the polar W^- production angle. The relative contributions of each W pair helicity state are also changed, which in turn affects the distributions of their decay products. Therefore, two independent types of information are combined when performing the measurement, namely the observed event rate of the studied processes and the kinematics of the detected decay products. In the analysis of the latter, the information contained in the multi-dimensional phase space has been treated by using integrated optimal observables.

The outline of this thesis is as follows: The SM theoretical framework, which is being tested with this analysis, is reviewed in Chapter 2. In Chapter 3 the main parts of the experimental apparatus used for the data taking, i.e. the LEP collider and the ALEPH detector, are briefly described. At the end of this chapter, those standard ALEPH reconstruction procedures which are more relevant for this analysis are also described. The fitting method which is used to extract the TGCs from the selected data sample is introduced in Chapter 4. In Chapter 5, the event selection and reconstruction procedures are described and their performance is tested using simulated events. The TGC measurement results are finally presented in Chapter 6 and the summary and conclusions are given in Chapter 7.

Chapter 2

Theoretical framework

2.1 The Standard Model

A "standard model" is a theoretical framework, built from the observation, which predicts physics phenomena. The Standard Model (SM) of particle physics provides a unified description of the electromagnetic, weak and strong forces in the language of quantum field theories (QFT) which has been experimentally verified to a high degree of accuracy over a wide range of energies and processes.

The SM is a quantum field gauge theory based on the symmetry group $\mathrm{SU}(3)_C \times \mathrm{SU}(2)_T \times \mathrm{U}(1)_Y$ [1, 2] which is characterized in part by the spectrum of elementary fields shown in Table 2.1. The matter fields are spin-$\frac{1}{2}$ fermions and their anti-particles. There are three families of fermion fields that are identical in every attribute except their masses. The first family contains the constituents of the stable matter we are used to observe in nature. It includes the up (u) and down (d) quarks (that are the constituents of nucleons, pions and other mesons) as well as the electron (e) and the electron-neutrino (ν_e). The quarks of of the other two families are constituents of heavier short-lived particles. They and their companion charged leptons rapidly decay to the quarks and leptons of the first family via the weak force.

The interaction among fermions is mediated by spin-1 gauge bosons: one massless photon (γ) and eight massless gluons ($g_1, \ldots, g_8$) for the electromagnetic and strong interactions respectively, and three massive bosons ($\mathrm{W}^{\pm}$ and Z^0) for the weak interaction.

Electrically charged particles interact due to the exchange of photons. The fact that the γ is massless accounts for the long range of the electromagnetic force.

LEPTONS

$$\begin{pmatrix} \nu_{e_L} \\ e_L \end{pmatrix}_{Y=-\frac{1}{2}} \quad \begin{pmatrix} \nu_{\mu_L} \\ \mu_L \end{pmatrix}_{Y=-\frac{1}{2}} \quad \begin{pmatrix} \nu_{\tau_L} \\ \tau_L \end{pmatrix}_{Y=-\frac{1}{2}}$$
$$(e_R)_{Y=-1} \quad (\mu_R)_{Y=-1} \quad (\tau_R)_{Y=-1}$$

QUARKS

$$\begin{pmatrix} u_L \\ d'_L \end{pmatrix}_{Y=\frac{1}{6}} \quad \begin{pmatrix} c_L \\ s'_L \end{pmatrix}_{Y=\frac{1}{6}} \quad \begin{pmatrix} t_L \\ b'_L \end{pmatrix}_{Y=\frac{1}{6}}$$
$$(u_R)_{Y=+\frac{2}{3}} \quad (c_R)_{Y=+\frac{2}{3}} \quad (t_R)_{Y=+\frac{2}{3}}$$
$$(d'_R)_{Y=-\frac{1}{3}} \quad (s'_R)_{Y=-\frac{1}{3}} \quad (b'_R)_{Y=-\frac{1}{3}}$$

GAUGE BOSONS

$$\gamma, Z^0, W^{\pm}, g_1, \ldots, g_8$$

Table 2.1: Standard Model fields. The $SU(2)_T \times U(1)_Y$ group representation of the fermion fields is explicitly shown.

Quarks carry a quantum number called *colour* which can take three different values. Coloured particles interact strongly through the exchange of gluons. Opposite to the electrically neutral photon, gluons possess colour charge and hence couple to one another. This makes the strong force between two coloured particles increase with increasing distance. As a consequence, quarks and gluons cannot appear as free particles, but exist only inside composite particles with no net colour charge, called hadrons.

Both quarks and leptons carry *weak isospin* ($\vec{T}$) and *weak hypercharge* (Y) quantum numbers which define their transformation properties under the $SU(2)_T \times U(1)_Y$ group. The $W^{\pm}$ and Z^0 bosons couple to these "weak charges". As shown in Table 2.1, the left-(right-)handed fields transform as weak isospin doublets(singlets). As a consequence, Ws couple only to left-handed fermions (with spin oriented opposite to the direction of motion).

The $[d', s', b']$ weak isospin eigenstates are lineal combinations of the $[d, s, b]$ mass eigenstates. The unitary matrix relating both is the Cabbibo-Kobayashi-Maskawa matrix, which depends on three angles and a phase, all of them being fundamental parameters of

the SM. This phase provides the only mechanism within the SM that can account for the observed violation of CP.

The spin-1 fields mediating the interactions result from the local gauge invariance of the SM lagrangian. Such a high degree of symmetry makes initially the theory unphysical. If the symmetries of the SM lagrangian were fully respected in nature, we would not distinguish an electron from a neutrino or a proton from a neutron. Moreover, the local invariance prevents the gauge bosons to have mass, while we know that for a realistic theory we need massive weak vector bosons. These problems are solved if we consider that the $SU(2)_T \times U(1)_Y$ symmetry is *spontaneously broken*.

The spontaneous symmetry breaking (SSB) is a general phenomenon which happens when the symmetric solutions of a theory are unstable and the ground state of the system is degenerated. An important point is that in a spontaneously broken gauge theory, the symmetry is, in a sense, still present; it is only "hidden" by the choice of ground state, and the theory can be shown to remain renormalisable [3]. The renormalisability ensures that once a few parameters are determined experimentally, quantitative predictions can be calculated to arbitrary accuracy as a perturbative expansion in the coupling constant.

Therefore, in the SM the masses of the gauge fields (as well as the fermions) are generated by SSB, ensuring that one of them (the photon) remains massless. The latter is attained by choosing a vacuum (the ground state in a QFT) which only possesses $U(1)_{EM}$ symmetry. As a result of the SSB mechanism, the existence of a physical scalar particle is predicted in the minimal version of the SM, the so called Higgs boson.

The Higgs boson has not been observed experimentally yet. The electroweak precision measurements made at LEP1, SLD and ν-Nucleon experiments have some sensitivity to the $\log(M_H)$ through loop corrections, and allow to constrain $\log(M_H)$ to be $1.88^{+0.28}_{-0.30}$ at 68% confidence level [4]. Direct searches at LEP provide a lower limit: $M_H > 89.7$ GeV/c^2 at 95% confidence level [6].

The Electroweak Lagrangian

The lagrangian density of the electroweak interactions, once the SSB scalar sector has been included, can be written in the unitary gauge (where the physics content of the theory is explicit) as

$$\begin{aligned}\mathcal{L}_{EW} &= \sum_f (\overline{f}_L i\gamma^\mu D_\mu f_L + \overline{f}_R i\gamma^\mu D_\mu f_R) \\ &\quad - \frac{1}{4}\vec{\mathcal{W}}_{\mu\nu}\cdot\vec{\mathcal{W}}^{\mu\nu} - \frac{1}{4}\mathcal{B}_{\mu\nu}\mathcal{B}^{\mu\nu} \\ &\quad + (D_\mu\Phi)^\dagger(D^\mu\Phi) - V(\Phi) \\ &\quad - G_e(\overline{f}_L\Phi f_R + \overline{f}_R\Phi f_L)\,. \end{aligned} \tag{2.1}$$

The two first terms account for the fermion (denoted as $f_{L,R}$) kinetic energies and their interactions with the gauge bosons. These interactions appear through the covariant derivative D_μ

$$D_\mu = \partial_\mu - ig\vec{\mathcal{T}}\cdot\vec{\mathcal{W}}_\mu - ig'\mathcal{Y}\mathcal{B}_\mu\,, \tag{2.2}$$

where $[g, \vec{\mathcal{T}}, \vec{\mathcal{W}}]$ and $[g', \mathcal{Y}, \mathcal{B}_\mu]$ are are the coupling constant, generators and gauge bosons associated to the SU(2) and U(1) groups, respectively.

The third and fourth terms in Eq. (2.1) account for the gauge bosons kinetic energies and self-interactions. The field strength tensors appearing in these terms are given by

$$\vec{\mathcal{W}}_{\mu\nu} \equiv \partial_\mu\vec{\mathcal{W}}_\nu - \partial_\nu\vec{\mathcal{W}}_\mu + g\vec{\mathcal{W}}_\mu\times\vec{\mathcal{W}}_\nu\,, \tag{2.3}$$

$$\mathcal{B}_{\mu\nu} \equiv \partial_\mu\mathcal{B}_\nu - \partial_\nu\mathcal{B}_\mu\,. \tag{2.4}$$

The last term in Eq. (2.3) arises from the non-abelian character of the SU(2) group (i.e. the $\mathcal{T}_i$'s do not commute with each other). This term is the one generating the trilinear and quadrilinear self-couplings of the $\vec{\mathcal{W}}_\mu$ fields, which are the subject of this analysis.

The SSB mechanism is introduced through the scalar field Φ appearing in the last terms of Eq. (2.1). This field is a weak isospin doublet and can be written in the unitary gauge as

$$\Phi = \frac{1}{\sqrt{2}}\begin{pmatrix} 0 \\ v+H \end{pmatrix}\,, \tag{2.5}$$

where the Higgs field (H) appears explicitly.

The mass terms of the gauge bosons appear from their interaction with the Higgs field, in the fifth term of Eq. (2.1). Their explicit form is

$$\frac{v^2}{8}(\mathcal{W}_{1\mu},\mathcal{W}_{2\mu},\mathcal{W}_{3\mu},\mathcal{B}_\mu)\left(\begin{array}{cc|cc} g^2 & 0 & 0 & 0 \\ 0 & g^2 & 0 & 0 \\ \hline 0 & 0 & g^2 & -gg' \\ 0 & 0 & -gg' & g^2 \end{array}\right)\left(\begin{array}{c}\mathcal{W}_{1\mu}\\ \mathcal{W}_{2\mu}\\ \mathcal{W}_{3\mu}\\ \mathcal{B}_\mu\end{array}\right) . \tag{2.6}$$

The off-diagonal terms in Eq. (2.6) indicate that the $\mathcal{W}_{3\mu}$ and $\mathcal{B}_\mu$ fields are not mass eigenstates. By diagonalising this matrix and requiring that the charge of the $\mathrm{W}^\pm$ bosons is well defined, the physical $\mathrm{W}^\pm, \mathrm{Z}^0$ and γ bosons appear as a linear combination of the original $\vec{\mathcal{W}}$ and $\mathcal{B}$ fields

$$\left(\begin{array}{c}\mathrm{Z}^0{}_\mu\\ \mathrm{A}_\mu\end{array}\right) = \left(\begin{array}{cc}\cos\theta_W & -\sin\theta_W\\ \sin\theta_W & \cos\theta_W\end{array}\right)\left(\begin{array}{c}\mathcal{W}_{3\mu}\\ \mathcal{B}_\mu\end{array}\right) , \tag{2.7}$$

$$\left(\begin{array}{c}\mathrm{W}^+{}_\mu\\ \mathrm{W}^-{}_\mu\end{array}\right) = \frac{1}{\sqrt{2}}\left(\begin{array}{cc}1 & -i\\ 1 & i\end{array}\right)\left(\begin{array}{c}\mathcal{W}_{1\mu}\\ \mathcal{W}_{2\mu}\end{array}\right) , \tag{2.8}$$

where θ_W is the so called *weak mixing angle*, defined by

$$\tan\theta_W \equiv \frac{g'}{g} . \tag{2.9}$$

2.2 Triple Gauge Boson Couplings

The term in the electroweak lagrangian giving rise to the gauge boson self-interactions can be written in terms of the physical gauge boson fields, thus the two triple (ZWW and γWW) and four quartic (ZZWW, $\gamma\gamma$WW, ZγWW and WWWW) gauge boson couplings

(TGCs and QGCs) predicted by the SM appear explicitly

$$
\begin{aligned}
-\frac{1}{4}\vec{\mathcal{W}}_{\mu\nu}\cdot\vec{\mathcal{W}}^{\mu\nu} - \frac{1}{4}\mathcal{B}_{\mu\nu}\mathcal{B}^{\mu\nu} = \\
&-\frac{1}{4}\mathrm{A}_{\mu\nu}\mathrm{A}^{\mu\nu} - \frac{1}{2}\mathrm{W}^{+}_{\mu\nu}\mathrm{W}^{-\mu\nu} - \frac{1}{4}\mathrm{Z}_{\mu\nu}\mathrm{Z}^{\mu\nu} \\
&-ig(\mathrm{W}^{-\mu\nu}\mathrm{W}^{+}_{\nu} - \mathrm{W}^{+\mu\nu}\mathrm{W}^{-}_{\nu})(\cos\theta_W\mathrm{Z}_{\mu} + \sin\theta_W\mathrm{A}_{\mu}) \\
&-ig(\cos\theta_W\mathrm{Z}^{\mu\nu} + \sin\theta_W\mathrm{A}^{\mu\nu})\mathrm{W}^{+}_{\mu}\mathrm{W}^{-}_{\nu} \\
&-g^2\cos^2\theta_W[(\mathrm{Z}_{\mu}\mathrm{Z}^{\mu})(\mathrm{W}^{+}_{\nu}\mathrm{W}^{-\nu}) - (\mathrm{Z}_{\mu}\mathrm{W}^{+\mu})(\mathrm{Z}_{\nu}\mathrm{W}^{-\nu})] \\
&-g^2\sin^2\theta_W[(\mathrm{A}_{\mu}\mathrm{A}^{\mu})(\mathrm{W}^{+}_{\nu}\mathrm{W}^{-\nu}) - (\mathrm{A}_{\mu}\mathrm{W}^{+\mu})(\mathrm{A}_{\nu}\mathrm{W}^{-\nu})] \\
&+g^2\sin^2\theta_W\cos^2\theta_W[(\mathrm{A}_{\mu}\mathrm{W}^{+\mu})(\mathrm{Z}_{\nu}\mathrm{W}^{-\nu}) + (\mathrm{Z}_{\mu}\mathrm{W}^{+\mu})(\mathrm{A}_{\nu}\mathrm{W}^{-\nu}) \\
&\qquad -2(\mathrm{Z}_{\mu}\mathrm{A}^{\mu})(\mathrm{W}^{+}_{\nu}\mathrm{W}^{-\nu})] \\
&-\frac{g^2}{2}[(\mathrm{W}^{+}_{\mu}\mathrm{W}^{-\mu})(\mathrm{W}^{+}_{\nu}\mathrm{W}^{-\nu}) - (\mathrm{W}^{+}_{\mu}\mathrm{W}^{+\mu})(\mathrm{W}^{-}_{\nu}\mathrm{W}^{-\nu})]\,, \qquad (2.10)
\end{aligned}
$$

where the following notation has been used:

$$
G_{\mu\nu} \equiv \partial_{\mu}G_{\nu} - \partial_{\nu}G_{\mu}\ ;\ (G = \mathrm{A}, \mathrm{Z}, \mathrm{W}^{\pm})\,. \qquad (2.11)
$$

From Eq. (2.10) it can be seen that the electroweak coupling constants appear at second order in the QGC terms, thus the strength of these interactions will be smaller than that in the triple gauge boson or fermion-boson vertices. As a consequence, the limits in the QGCs that might be set at LEP2 will be much weaker than those in the TGCs.

In order to study the TGCs we need a parameterisation of the vector gauge boson interactions that goes beyond the SM. The most general of such parameterisations which is Lorentz and $\mathrm{U}(1)_{EM}$ invariant is given by

$$
\begin{aligned}
\mathcal{L}_{TGC} &= \sum_{\mathrm{V}=\gamma,\mathrm{Z}} g_{\mathrm{VWW}}[-i(g_1^{\mathrm{V}}(\mathrm{V}_{\mu}\mathrm{W}^{-\mu\nu}\mathrm{W}^{+}_{\nu} - \mathrm{V}_{\mu}\mathrm{W}^{+\mu\nu}\mathrm{W}^{-}_{\nu}) \\
&+ \kappa_{\mathrm{V}}\mathrm{V}_{\mu\nu}\mathrm{W}^{+\mu}\mathrm{W}^{-\nu}) \\
&- i\frac{\lambda_{\mathrm{V}}}{m^2_{\mathrm{W}}}\mathrm{V}_{\mu\rho}\mathrm{W}^{+\rho\nu}\mathrm{W}^{-\mu}_{\nu} \\
&+ g_5^{\mathrm{V}}\epsilon_{\mu\nu\rho\sigma}((\partial^{\rho}\mathrm{W}^{-\mu})\mathrm{W}^{+\nu} - (\partial^{\rho}\mathrm{W}^{+\nu})\mathrm{W}^{-\mu})\mathrm{V}^{\sigma} \\
&+ g_4^{\mathrm{V}}\mathrm{W}^{+}_{\nu}\mathrm{W}^{-}_{\mu}(\partial^{\mu}\mathrm{V}^{\nu} + \partial^{\nu}\mathrm{V}^{\mu}) \\
&+ i\frac{\tilde{\kappa_{\mathrm{V}}}}{2}\mathrm{W}^{+}_{\nu}\mathrm{W}^{-}_{\mu}\epsilon^{\mu\nu\rho\sigma}\mathrm{V}_{\rho\sigma} \\
&+ i\frac{\tilde{\lambda}_{\mathrm{V}}}{2m^2_{\mathrm{W}}}\mathrm{W}^{+\mu}_{\nu}\mathrm{W}^{-}_{\rho\nu}\epsilon^{\nu\rho\alpha\beta}\mathrm{V}_{\alpha\beta}]\,, \qquad (2.12)
\end{aligned}
$$

where the overall couplings are taken as $g_{\gamma \mathrm{WW}} = e$ and $g_{\mathrm{ZWW}} = e \cot \theta_W$, for convenience.

As it can be seen by comparing Eqs. (2.10) and (2.12), in the SM (at tree level) we have $g_1^\gamma = g_1^\mathrm{Z} = \kappa_\gamma = \kappa_\mathrm{Z} = 1$ while the rest of parameters vanish.

For the photon couplings, the first coefficient in Eq. (2.12) determines the charge of the W and hence is fixed to $g_1^\gamma = 1$, the second and third terms (κ_γ and λ_γ) are related to the magnetic moment μ_W and electric quadrupole moment Q_W of the W^+ by

$$\mu_\mathrm{W} = \frac{e}{2m_\mathrm{W}}(1 + \kappa_\gamma + \lambda_\gamma) \,, \tag{2.13}$$

$$Q_\mathrm{W} = -\frac{e}{m_\mathrm{W}^2}(\kappa_\gamma - \lambda_\gamma) \,. \tag{2.14}$$

It should be noted that the seven operators in Eq. (2.12) are sufficient to parameterise the VWW vertex due to the fact that only seven out of the nine helicity states of the W pair are accessible by s-channel vector boson exchange ($J = 1$). The other two helicity combinations have both W spins pointing in the same direction and thus have $J \geq 2$ (see Sect. 2.3.1).

With no extra assumptions, we are left with 13 parameters to parameterise the VWW vertex. Given the expected statistics of LEP2 ($\sim 10^4$ W pairs per experiment), a simultaneous extraction of all these couplings from a multi-parameter fit to the data is out of reach. Therefore, a reduction of the number of parameters is needed. To do this, we will first classify the seven operators of Eq. (2.12) according to their transformation properties under the discrete symmetries C and P. Three out of these seven terms conserve C and P separately ($g_1^\mathrm{V}, \kappa_\mathrm{V}$ and λ_V), one violates C and P separately but conserves CP (g_5^V) and three violate CP ($g_4^\mathrm{V}, \tilde{\kappa_\mathrm{V}}$ and $\tilde{\lambda_\mathrm{V}}$).

Based on very general theoretical assumptions [5], the possibility of observation of C, P or CP violation at LEP2 is strongly disfavoured. For this reason, the present analysis concentrates on C and P conserving couplings only.

Effective Lagrangian Approach

The deviation from the SM TGCs can be parameterised in a manifestly gauge-invariant way by using the *effective lagrangian* approach. Effective lagrangians are often used to describe the low energy effects of physics beyond the SM. They are always associated with a cutoff Λ which measures the scale of the new physics. Hence, this approach has a limited energy range and cannot be applied for energies above Λ.

The effective lagrangian is defined as the most general object which obeys certain symmetries and contains a given set of fields. If SU(2)×U(1) gauge invariant operators involving the gauge bosons and the Higgs field are built, one needs to consider operators with dimension up to twelve in order to generate all kinds of TGC appearing in Eq. (2.12). The effects of such new interactions on low energy observables can be described as a power series in $1/\Lambda$. Hence, the dominant terms will be those with dimension six.

An effective lagrangian inducing triple gauge boson interactions can be written by using SU(2)×U(1)-invariant operators of dimension six which conserve CP as

$$\begin{aligned}\mathcal{L}_{TGC}^{d=6} &= ig'\frac{\alpha_{\mathrm{B}\Phi}}{m_W^2}(D_\mu\Phi)^\dagger\mathcal{B}^{\mu\nu}(D_\nu\Phi) \\ &+ ig\frac{\alpha_{\mathrm{W}\Phi}}{m_W^2}(D_\mu\Phi)^\dagger\vec{\tau}\cdot\vec{\mathcal{W}}^{\mu\nu}(D_\nu\Phi) \\ &+ g\frac{\alpha_{\mathrm{W}}}{6m_W^2}\vec{\mathcal{W}}_\nu^\mu\cdot(\vec{\mathcal{W}}_\rho^\nu\times\vec{\mathcal{W}}_\mu^\rho)\,, \end{aligned} \tag{2.15}$$

where the τ_i represent the Pauli spin matrices. Replacing the Higgs doublet field by (2.5) yields non-vanishing anomalous TGCs in (2.12)

$$\Delta g_1^{\mathrm{Z}} = \frac{\alpha_{\mathrm{W}\Phi}}{\cos^2\theta_W}\,, \tag{2.16}$$

$$\Delta\kappa_\gamma = -\frac{\cos^2\theta_W}{\sin^2\theta_W}(\Delta\kappa_{\mathrm{Z}}-\Delta g_1^{\mathrm{Z}}) = \alpha_{\mathrm{W}\Phi}+\alpha_{\mathrm{B}\Phi}\,, \tag{2.17}$$

$$\lambda_\gamma = \lambda_{\mathrm{Z}} = \alpha_{\mathrm{W}}\,, \tag{2.18}$$

where the TGCs have been expressed in terms of their deviations from the (tree level) SM values, which is convenient when searching for possible anomalous contributions

$$\Delta g_1^{\mathrm{Z}} \equiv g_1^{\mathrm{Z}} - 1 \;\;;\;\; \Delta\kappa_\gamma \equiv \kappa_\gamma - 1 \;\;;\;\; \Delta\kappa_{\mathrm{Z}} \equiv \kappa_{\mathrm{Z}} - 1\,. \tag{2.19}$$

At this stage we are left with three independent TGCs ($\Delta g_1^{\mathrm{Z}}, \Delta\kappa_\gamma$ and λ_γ), which are the ones considered in this analysis for their experimental determination. It should be noticed that the SU(2)×U(1) gauge invariance requirement alone has not provided any constraint on the TGCs. Instead, it is a low energy approximation (neglecting operators of dimension greater than six) which leads to relations among the various TGCs.

2.3 W pair production

LEP2 provides the first opportunity to have experimental access to the process $e^+e^- \to \mathrm{W}^+\mathrm{W}^-$. To lowest order, this process takes place via the Feynman diagrams

of Fig. 2.1, known as the CC03 diagram family. It represents an ideal benchmark where to study the TGCs, since they appear already at tree level. However, the sensitivity of the total cross section to anomalous couplings at LEP2 energies is too weak to yield stringent bounds and one is forced to use the differential cross section information to improve them. In general, radiative corrections tend to distort the angular distributions (hence mimicking the effect of anomalous couplings). It is therefore mandatory to have them into account in order not to obtain biased measurements.

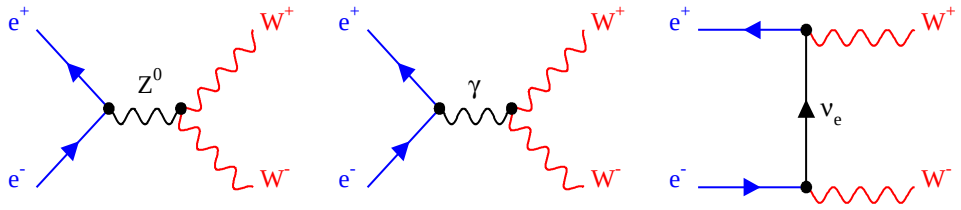

Figure 2.1: Feynman diagrams for the process $e^+e^- \to \mathrm{W}^+\mathrm{W}^-$.

In this section, several theoretical aspects of W pair production in e^+e^- collisions which are relevant for the TGCs extraction are reviewed. First, on-shell W pairs are considered in Sect. 2.3.1, since most of the effects of anomalous couplings can already be understood at this level. Second, in Sect. 2.3.2 the complete four-fermion production process is analysed.

2.3.1 On-shell W pair production and Helicity Analysis

We consider the reaction

$$e^+(p_+, \frac{\sigma_+}{2}) + e^-(p_-, \frac{\sigma_-}{2}) \to \mathrm{W}^+(k_+, \lambda_+) + \mathrm{W}^-(k_-, \lambda_-) \tag{2.20}$$

where $p_\pm, k_\pm$ and $\frac{\sigma_\pm}{2}, \lambda_\pm$ denote the momenta and helicities of the respective particles. The total helicity amplitude for this process can be written as a sum of the s-channel photon and Z^0 exchange and of t-channel neutrino exchange

$$\mathcal{M}(\sigma, \lambda_-, \lambda_+) = \mathcal{M}_\gamma + \mathcal{M}_\mathrm{Z} + \mathcal{M}_\nu \ , \tag{2.21}$$

where $\sigma \equiv \sigma_- = -\sigma_+$, since we consider the leptons massless.

It is instructive to factorise the leading angular dependence of the helicity amplitudes, which can be written in terms of the *d-functions* [6]. Hence, in the centre of mass frame,

with the e^- momentum along the z-axis and the W^- transverse momentum pointing along the x-axis, the helicity amplitudes are given by

$$\mathcal{M}(\sigma, \lambda_-, \lambda_+; \Theta) = \sqrt{2}\sigma e^2 \tilde{\mathcal{M}}_{\sigma,\lambda_-\lambda_+}(\Theta) d^{J_0}_{\sigma,\lambda_- -\lambda_+}(\Theta) \; , \tag{2.22}$$

where Θ represents the polar angle of the outgoing W^-.

Using helicity conservation arguments, it can be immediately seen that:

- For $|\lambda_- - \lambda_+| = 2$, only t-channel neutrino exchange contributes, and the incoming electron must be left-handed.
- $|\lambda_- - \lambda_+| = 0, 1$ are the only possible final states for s-channel photon and Z^0 exchange.

The different contribution reduced amplitudes ($\tilde{\mathcal{M}}$) for the latter can be written as:

$$\begin{aligned}
\tilde{\mathcal{M}}_\gamma &= -\beta A^\gamma_{\lambda_-\lambda_+} \\
\tilde{\mathcal{M}}_Z &= +\beta A^Z_{\lambda_-\lambda_+} \left[1 - \delta_{\sigma,-1} \frac{1}{2\sin^2\theta_W}\right] \frac{s}{s - m_Z^2} \\
\tilde{\mathcal{M}}_\nu &= +\delta_{\sigma,-1} \frac{1}{2\beta\sin^2\theta_W} \left[B_{\lambda_-\lambda_+} - \frac{1}{1 + \beta^2 - 2\beta\cos\Theta} C_{\lambda_-\lambda_+}\right]
\end{aligned} \tag{2.23}$$

where $\beta = \sqrt{1 - \frac{4m_W^2}{s}}$ is the $W^\pm$ velocity and s is the e^+e^- centre of mass energy squared. The terms A^V, B and C are given in Table 2.2.

$\lambda_-\lambda_+$	$A^V_{\lambda_-\lambda_+}$	$B_{\lambda_-\lambda_+}$	$C_{\lambda_-\lambda_+}$	$d^{J_0}_{\sigma,\lambda_- -\lambda_+}$
$++$	$g_1^V + 2\gamma^2\lambda_V + \frac{i}{\beta}(\tilde{\kappa}_V + \tilde{\lambda}_V - 2\gamma^2\tilde{\lambda}_V)$	1	$1/\gamma^2$	$-\sigma\sin\Theta/\sqrt{2}$
$--$	$g_1^V + 2\gamma^2\lambda_V - \frac{i}{\beta}(\tilde{\kappa}_V + \tilde{\lambda}_V - 2\gamma^2\tilde{\lambda}_V)$	1	$1/\gamma^2$	$-\sigma\sin\Theta/\sqrt{2}$
$+0$	$\gamma(f_3^V - ig_4^V + \beta g_5^V + \frac{i}{\beta}(\tilde{\kappa}_V - \tilde{\lambda}_V))$	2γ	$2(1+\beta)/\gamma$	$(1+\sigma\cos\Theta)/2$
$0-$	$\gamma(f_3^V + ig_4^V + \beta g_5^V - \frac{i}{\beta}(\tilde{\kappa}_V - \tilde{\lambda}_V))$	2γ	$2(1+\beta)/\gamma$	$(1+\sigma\cos\Theta)/2$
$0+$	$\gamma(f_3^V + ig_4^V - \beta g_5^V + \frac{i}{\beta}(\tilde{\kappa}_V - \tilde{\lambda}_V))$	2γ	$2(1-\beta)/\gamma$	$(1-\sigma\cos\Theta)/2$
-0	$\gamma(f_3^V - ig_4^V - \beta g_5^V - \frac{i}{\beta}(\tilde{\kappa}_V - \tilde{\lambda}_V))$	2γ	$2(1-\beta)/\gamma$	$(1-\sigma\cos\Theta)/2$
00	$g_1^V + 2\gamma^2\kappa_V$	$2\gamma^2$	$2/\gamma^2$	$-\sigma\sin\Theta/\sqrt{2}$

Table 2.2: Sub-amplitudes for $J_0 = 1$ helicity combinations of the process $e^-e^+ \to W^-W^+$. The abbreviation $f_3^V = g_1^V + \kappa_V + \lambda_V$ is used and $\gamma = \sqrt{s}/2m_W$.

It can be noticed from Table 2.2 that the individual contributions from each of the diagrams of Fig. 2.1 grows with energy for longitudinally polarised Ws and hence violate

unitarity. Within the SM, where the only non-vanishing TGCs appearing in Table 2.2 are $g_1^V = \kappa_V = 1$ and $f_3^V = 2$ $(V = \gamma, \mathrm{Z}^0)$, the sum of the three diagrams contains the needed cancellations to preserve this unitarity.

The presence of anomalous couplings destroys these cancellations properties and therefore, makes the cross section diverge in the high energy limit. As a consequence, the sensitivity to the TGCs increases with increasing centre of mass energy. Instead, for centre of mass energies close to the W pair production threshold, the sensitivity to the TGCs goes to zero, because of the β suppression factors in $\tilde{\mathcal{M}}_\gamma$ and $\tilde{\mathcal{M}}_Z$.

Only seven $\mathrm{W}^+\mathrm{W}^-$ helicity combinations contribute to the $J_0 = 1$ channel , as shown in Table 2.2. This explains why exactly seven coupling constants are needed to parameterise the most general WWV vertex, as discussed in Sect. 2.2. As shown in Fig. 2.2, each of these helicity combinations contributes to the angular distribution of the produced Ws $(d\sigma/d\cos\Theta)$ in a different way. In addition, the TGCs combination entering in each helicity state vary from one to the other , as seen in Table 2.2. Therefore, it will be possible to extract information on the TGCs by separating the various $\mathrm{W}^+\mathrm{W}^-$ polarisation states.

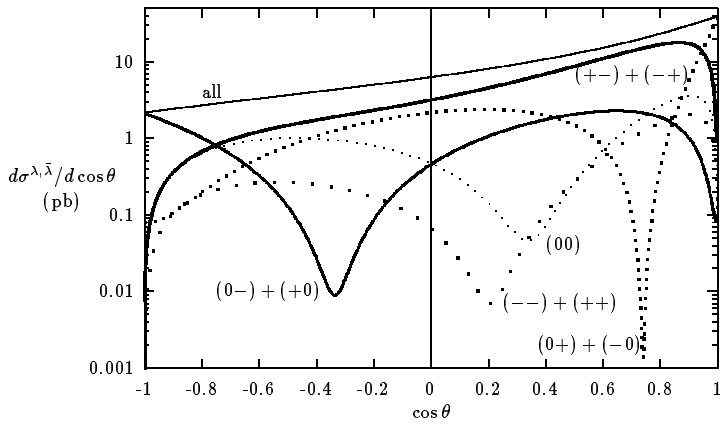

Figure 2.2: Contributions from different $\mathrm{W}^+\mathrm{W}^-$ helicity states to the W^- production angle distribution in $e^+e^- \to \mathrm{W}^+\mathrm{W}^-$. SM TGCs are assumed and $\sqrt{s} = 190\mathrm{GeV}$.

The $V - A$ structure of the W-fermion vertices allows to obtain information on the polarisation of the Ws from the angular distributions of their decay products. Therefore, a separation of the different $\mathrm{W}^+\mathrm{W}^-$ helicity states can be obtained by analysing the five-fold differential angular distribution which determines completely the event kinematics, assuming massless fermions. This can be written for on-shell Ws in terms of helicity

amplitudes as

$$\begin{aligned}\frac{d^5\sigma\ (e^-e^+ \to W^-W^+ \to f_1\bar{f}_2\ f_3\bar{f}_4)}{d\cos\Theta\ \ d\cos\theta_1\ d\,\phi_1\ \ d\cos\theta_2\ d\,\phi_2} &= \frac{\beta}{128\pi s}\left(\frac{3}{8\pi}\right)^2 B(W\to f_1\bar{f}_2)\ B(W\to f_3\bar{f}_4) \\ &\times \sum_{\sigma,\lambda_-,\lambda_+,\lambda'_-,\lambda'_+} \mathcal{M}(\sigma,\lambda_-,\lambda_+)\mathcal{M}^*(\sigma,\lambda'_-,\lambda'_+) \\ &\times D_{\lambda_-,\lambda'_-}(\theta_1,\phi_1)D_{\lambda_+,\lambda'_+}(\pi-\theta_2,\phi_2+\pi)\ , \quad (2.24)\end{aligned}$$

where the terms $B(W \to f\bar{f})$ account for the W decay branching ratios and (θ_i, ϕ_i) are the fermion (anti-fermion) angles in the W^- (W^+) rest frame. This rest frame is defined by a boost of the e^+e^- centre of mass frame along the W^+W^- production direction. The information on the angular distribution of the W decay products is contained in the $D_{\lambda,\lambda'}$ functions

$$D_{\lambda,\lambda'}(\theta,\phi) = \ell_\lambda(\theta,\phi)\ \ell^*_{\lambda'}(\theta,\phi)\ , \quad (2.25)$$

where

$$\ell_-(\theta,\phi) = \frac{1}{\sqrt{2}}(1+\cos\theta)\ \mathrm{e}^{-i\phi}\ , \quad (2.26)$$

$$\ell_0(\theta,\phi) = -\sin\theta\ , \quad (2.27)$$

$$\ell_+(\theta,\phi) = \frac{1}{\sqrt{2}}(1-\cos\theta)\ \mathrm{e}^{i\phi}\ . \quad (2.28)$$

In this way the θ angle distribution of the fermions in the W rest frame will provide information about its parent W helicity state. A non trivial dependence on ϕ also appears due to interference between the possible W polarisations. In particular, the interference with the large $\mathcal{M}_{\pm\mp}$ amplitudes (coming only from neutrino t-channel exchange) might amplify the effect of anomalous couplings in the ϕ distributions.

2.3.2 Off-shell W pair production

The simplest extension of on-shell W pair production to the off-shell case consists in the convolution

$$\sigma^{CC03}(s) = \int_0^s dk_+^2\,\rho_W(k_+^2)\int_0^{(\sqrt{s}-|k_+|)^2} dk_-^2\,\rho_W(k_-^2)\,\sigma_0^{CC03}(s;k_+^2,k_-^2), \quad (2.29)$$

of a hard-scattering off-shell cross section (σ_0^{CC03}) for the W production stage, with the Breit-Wigner distribution

$$\rho_W(k_\pm^2) = \frac{1}{\pi}\frac{M_W,\ _W}{|k_\pm^2 - M_W^2 + iM_W,\ _W|^2} \times B_{f_i\bar{f}_j} \ \overrightarrow{\Gamma_W\to 0}\ \delta(k_\pm^2 - M_W^2) \times B_{f_i\bar{f}_j}, \quad (2.30)$$

W for the decay stage [7]. Here , $_W$ denotes the decay width of the W boson, and $B_{f_i\bar{f}_j}$ the branching ratio for W $\to f_i\bar{f}_j$. For , $_W \to 0$ the on-shell cross section is recovered. The explicit expression for the twofold differential cross section σ_0^{CC03} can be found in reference [7].

This approach does not lead to gauge-invariant results because of two reasons:

- Not all the diagrams for the process $e^+e^- \to f_1\bar{f}_2f_3\bar{f}_4$ are taken into account, but only the doubly resonant ones which factorise into production and decay.
- The inclusion of finite width effects goes beyond a pure perturbative expansion and introduces some gauge dependence in the results.

Four-Fermion Production

In general, all diagrams contributing to a given final state have to be taken into account in order to obtain a manifestly gauge-independent result. For the process $e^+e^- \to f_1\bar{f}_2f_3\bar{f}_4$ the full set of diagrams contains, in addition to the CC03 family, the so called *background diagrams* (with only one or even no resonant W boson). The complete set of possible Feynman diagrams contributing to a four-fermion final state is shown in Fig. 2.3.

All four-fermion final states can be classified according to the topologies of the Feynman graphs entering the process [8]. They are usually separated into three classes:

CC Processes with final states of type $f_1^u\bar{f}_1^df_2^u\bar{f}_2^d$ are called *charged current processes.*

NC Processes with final states of type $f_1\bar{f}_1f_2\bar{f}_2$ are called *neutral current processes.*

`mix` Processes which may be considered as both CC and NC types are called *mixed processes.* An example for a mixed process is the production of $u\bar{d}d\bar{u} \equiv u\bar{u}d\bar{d}$.

	$\bar{d}u$	$\bar{s}c$	$\bar{e}\nu_e$	$\bar{\mu}\nu_\mu$	$\bar{\tau}\nu_\tau$
$\bar{d}u$	*43*	**11**	20	**10**	**10**
$\bar{e}\nu_e$	20	20	*56*	18	18
$\bar{\mu}\nu_\mu$	**10**	**10**	18	*19*	**9**

Table 2.3: Number of Feynman diagrams contributing to the four-fermion processes with WW-like final states.

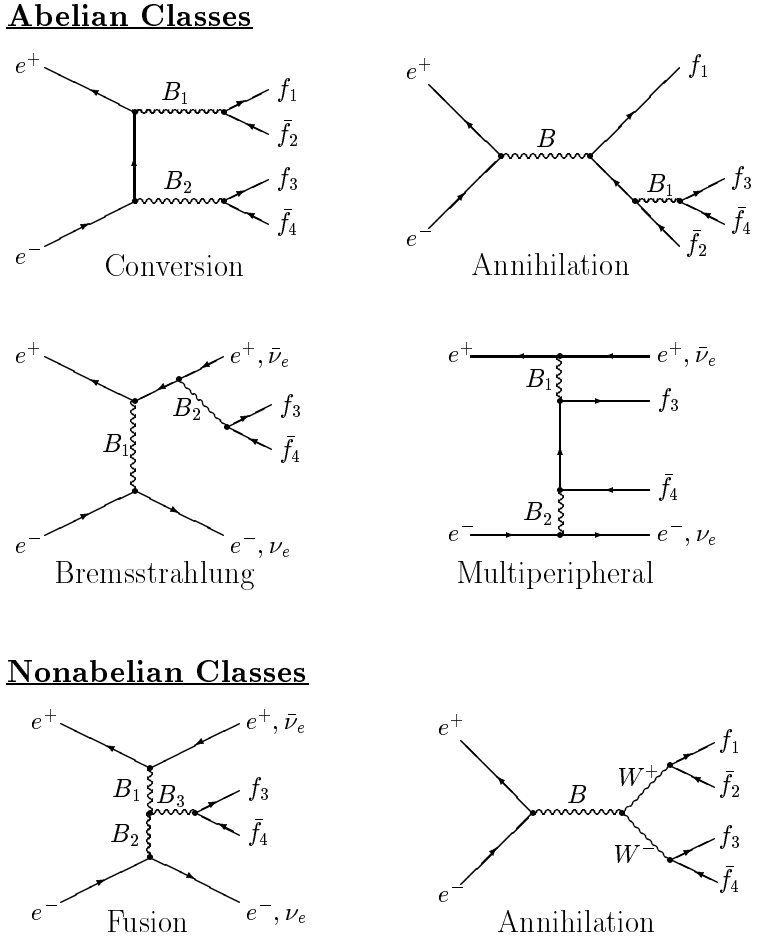

Figure 2.3: Four-fermion production Feynman diagrams.

The number of diagrams contributing to WW-like four-fermion final states is shown in Table. 2.3. Three different event classes might be distinguished, all of them containing the CC03 process as a subset:

- The CC11 process (boldface numbers in Table 2.3).
  The two fermion pairs produced are different and the final state does not contain electrons nor electron-neutrinos. It is fully covered by diagrams containing only doubly- and singly-resonating W bosons. There are less diagrams if neutrinos are

produced (CC10 and CC09).

- The CC20 process (roman numbers in Table 2.3).
  Additional diagrams must be taken into account if electrons or electron-neutrinos are produced (see Fig. 2.3). There are less diagrams for a purely leptonic final state (CC20 and CC18).

- The `mix56` process (italic numbers in Table 2.3).
  If the final state contains two mutually charge conjugated fermion pairs, it can also be reached through intermediate Z pair production, leading to extra Feynman diagrams families. There are less diagrams if no electrons are produced (`mix43`) or if the final state contains neutrinos (`mix19`).

Finite W width inclusion

The W boson propagators entering in the matrix element for W pair production involve poles at $k_{\pm}^2 = M_W^2$. These have to be cured by introducing the finite width in one way or another, while at the same time preserving gauge invariance and unitarity through a proper high energy behaviour. In field theory, such widths arise naturally from the imaginary parts of higher order diagrams describing the boson self-energies, resumed to all orders. This procedure was successfully used in LEP1 to describe the Z^0 resonance to very high numerical accuracy. However, in doing Dyson summation of self-energy graphs, only a small subset of all the possible higher order diagrams is singled out, so that it is not surprising that the result is not gauge invariant.

Several shemes have been proposed for the introduction of finite decay widths in amplitudes which preserve gauge-invariance (e.g. the so called *fermion loop scheme* [9]). However, such schemes often imply an increase in the complexity of the matrix elements and a consequent slowing down of the numerical calculations, therefore they are not suited for a Monte Carlo code. In practice, although not being theoretically justified, two more "intuitive" ways of introducing the finite W width are used:

- *Constant width scheme*: It consists of systematically replacing the W propagator

$$\frac{1}{k_{\pm}^2 - M_W^2} \rightarrow \frac{1}{k_{\pm}^2 - M_W^2 + iM_W,\ _W} \,. \tag{2.31}$$

  Since in perturbation theory the propagator for space-like momenta does not develop

an imaginary part, the introduction of a finite width also for $k^2 < 0$ has no physical motivation and in fact violates unitarity.

- *Running width scheme*: To improve on unitarity, the constant width can be replaced by a running one

$$, _W(k_\pm^2) = \frac{k_\pm^2}{M_W^2}, _W \ . \tag{2.32}$$

However, the gauge non-invariance problem remains.

After all, the question that should be addressed is whether the gauge breaking occurring in these naive schemes is relevant or, like the gauge breaking in the LEP1 analysis, negligible for all practical purposes. The answer to this question is that a naive introduction of a running width without a proper inclusion of fermionic corrections to the three-boson vertex, which breaks $\mathrm{U}(1)_{EM}$ gauge invariance, leads to completely unreliable results for processes such as $e^+e^- \to e^-\bar{\nu}_e u\bar{d}$, where collinear singularities are present coming from the electromagnetic gauge-breaking terms. On the contrary, the $\mathrm{U}(1)_{EM}$-preserving constant width scheme gives numerical results close to the ones obtained with the fermion loop scheme.

2.3.3 Radiative Corrections

The complete set if $\mathcal{O}(\alpha)$ next to leading order corrections to W pair production have been performed for the on-shell case only. Owing to its complexity, a complete calculation of the $\mathcal{O}(\alpha)$ electroweak corrections for the off-shell case is still not available. So far only universal leading corrections are included in the Monte Carlo codes for off-shell W pair production.

The on-shell calculations can be used as a guide to predict some of the largest effects. It has been shown that the leading contributions to the radiative corrections have three origins:

- Initial state radiation.
- Coulomb singularity.
- Leading higer order terms via $\Delta\alpha$ and Δr.

Initial State Radiation

Collinear initial state radiation (ISR) off the incoming electrons and positrons yield large corrections of $\mathcal{O}(\alpha^n \log^n(s/m_e^2))$ after the cancellation of infrared singularities coming from the emission of virtual and soft real photons when including hard photon radiation. These leading logarithms can be resummed to all orders and incorporated in the cross section using a *flux function* or a *structure function* approach. Common to these two approaches is the assumption that ISR factorises [10]

$$\sigma(s) = \int_0^1 \int_0^1 dx_1 dx_2 \Phi(x_1)\Phi(x_2)\sigma_0(x_1 x_2 s) \,, \tag{2.33}$$

where $x_{1,2}$ represents the the radiated energy from the $e^{\pm}$, σ_0 is the non-radiative cross section and Φ is the energy distribution of a fermion after radiation. An explicit expression for the function Φ can be found in [10]. The effect of ISR is to reduce the effective centre of mass energy at which the electron and positron collide. This causes a reduction of the cross section (see Fig. 2.4) as well as a distortion of the W production angle distribution, as discussed in Sect. 2.3.4

Coulomb Singularity

Near threshold the long range of the Coulomb interaction between the two slowly moving W bosons causes large universal corrections, which are proportional to the Born cross section

$$\delta\sigma_{\mathrm{Coul}} \;\widetilde{\beta\to 0}\; \frac{\alpha\pi}{2\beta}\sigma_{\mathrm{B}} \,, \tag{2.34}$$

where β is the velocity of the W bosons in their centre of mass system. The singular behaviour of this correction for $\beta \to 0$ is a peculiarity of the on-shell approximation, which assumes stable W bosons. This singularity is regularised when a finite W width is introduced, since the range of the interaction is effectively truncated by the W decay. For the off-shell case, the correction can be written as [11]

$$\delta\sigma_{\mathrm{Coul}} = \sigma^{CC03}\,\frac{\alpha\pi}{2\bar{\beta}}\left[1 - \frac{2}{\pi}\arctan\left(\frac{|\beta_{\mathrm{M}}|^2 - \bar{\beta}^2}{2\bar{\beta}\,\mathfrak{Im}(\beta_{\mathrm{M}})}\right)\right] \,, \tag{2.35}$$

with σ^{CC03} denoting the doubly resonant part of the Born cross section,

$$\bar{\beta} \;=\; \sqrt{1 - 2(k_+^2 + k_-^2)/s + (k_+^2 - k_-^2)^2/s^2} \tag{2.36}$$

being the average velocity of the W bosons in their centre of mass system and

$$\beta_M \;=\; \sqrt{1-4(M_W^2 - iM_W,\ _W)/s}. \tag{2.37}$$

The maximal effect of $\sim 6\%$ is reached at threshold, while this correction still amounts $\sim 1.8\%$ at 190 GeV.

Improved Born Approximation

The dominant part of the electroweak radiative corrections (apart from photon radiation) can be incorporated by introducing effective couplings in the Born level expressions. This is referred to as the Improved Born Approximation (IBA).

The Born amplitude of the process $e^+e^- \to W^-W^+$ can be decomposed in a different way than that given by Eqs. (2.22) and (2.23) in such a way that unitarity cancellations between the different contributions are absent

$$\mathcal{M}_B^\sigma = \frac{e^2}{2\sin^2\theta_W}\mathcal{M}_I^\sigma \delta_{\sigma,-1} + e^2\mathcal{M}_Q^\sigma\ , \tag{2.38}$$

where $\mathcal{M}_I^\sigma$ defines the *isospin part* with the associated coupling $\frac{e}{\sin\theta_W}$, and $\mathcal{M}_Q^\sigma$ the *electromagnetic part* with the coupling e.

The definition of the eeγ coupling e in the low energy limit leads to large universal corrections to processes which involve energies at the electroweak scale. These corrections can be accounted for by substituting the fine structure constant $\alpha(0) = e^2/4\pi$ by the running electromagnetic coupling $\alpha(s)$. In the limit of a large top quark mass m_t one gets leading corrections proportional to $\alpha m_t^2/M_W^2$, which enter in the isospin part via the renormalisation of the W and Z masses (or equivalently $\sin^2\theta_W$), therefore are identical to those in the quantity Δr [12] and can be absorved substituting $\frac{e^2}{\sin^2\theta_W}$ by $4\sqrt{2}G_\mu M_W^2$.

The following IBA can then be defined

$$\mathcal{M}_{IBA}^\sigma = 2\sqrt{2}G_\mu M_W^2 \mathcal{M}_I^\sigma \delta_{\sigma,-1} + 4\pi\alpha(s)\mathcal{M}_Q^\sigma\ , \tag{2.39}$$

as proposed in [13], which incorporates these leading corrections. As it has been studied in [13], heavy mass contributions proportional to $\alpha\log m_t$ and $\alpha\log M_H$ that are not covered by Eq. (2.39) have a negligible impact in the approximation. A comparison between the IBA prediction and the exact $\mathcal{O}(\alpha)$ correction shows that, at LEP2 energies, they are compatible at the 1-2% level.

2.3.4 Γ_W, four-fermion and radiative corrections effect on TGCs

In the helicity amplitude analysis described in section 2.3.1, the W bosons were considered to have zero width. This procedure might neglect some important effects, however, and the corresponding physics issues will be discussed in this subsection. These are the influence of a finite W width, of radiative corrections (dominated by ISR) and the inclusion of four-fermion graphs in addition to those in the CC03 family.

When measuring the TGCs, information is extracted from both the total and differential cross sections for the process $e^+e^- \to \mathrm{W}^+\mathrm{W}^- \to f_1\bar{f}_2 f_3 \bar{f}_4$. Therefore, the effects of the above mentioned mechanisms on both observables have to be considered.

The distortion of the W pair production cross section caused by the sequential inclusion of the mentioned mechanisms is shown in Fig. 2.4. Note that both the ISR and the finite width smear the sharp threshold behaviour of the on-shell cross section at $\sqrt{s} = 2M_W$.

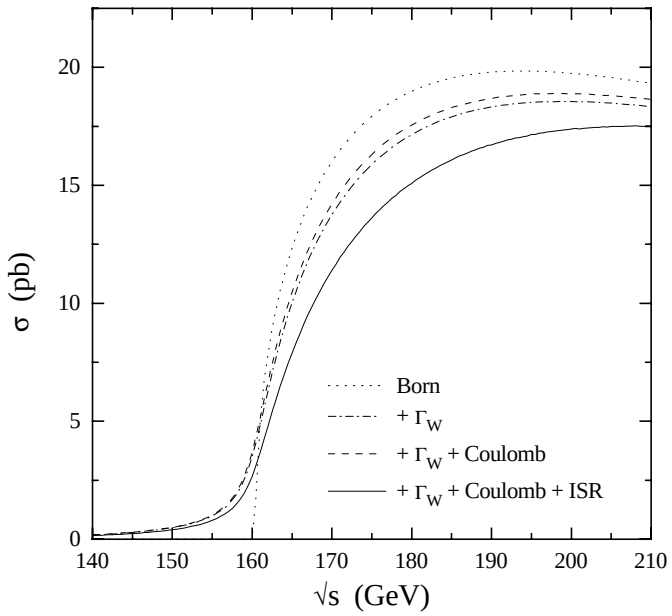

Figure 2.4: Effect of different higher order corrections on the cross-section for $e^+e^- \to W^+W^-$.

At the same time, these physical mechanisms could influence the angular distribution of the produced Ws and thus simulate the effect of anomalous couplings. The `GENTLE` program version 2.02 [15] has been used to compute the impact of some of these mechanisms on the $d\sigma/d\cos\Theta$ distribution, where Θ is the production angle of one of the W

bosons. The results are shown in Fig. 2.5, where the effects of a finite W width, ISR and `CC11` four-fermion background graphs are shown. It is seen from the figure that both the inclusion of a finite W width and of ISR tend to flatten the $d\sigma/d\cos\Theta$ distribution by a sizeable amount, as it happens for negative TGC parameters. ISR, for instance, lowers the available $\sqrt{s}$ of the event and hence reduces the forward peak of the W^- production cross section. On the other side, the inclusion of finite width allows the W bosons mass fluctuate around its nominal value. This fluctuation is not symmetrical due to the phase space limit given by the available centre of mass energy. As a consequence, the average momentum of the Ws increases thereby modifying the different helicity amplitudes contributions. Finally, it is also seen that the inclusion of the four-fermions background graphs of the `CC11` family varies the cross section by less than 0.5% in the whole range of scattering angle.

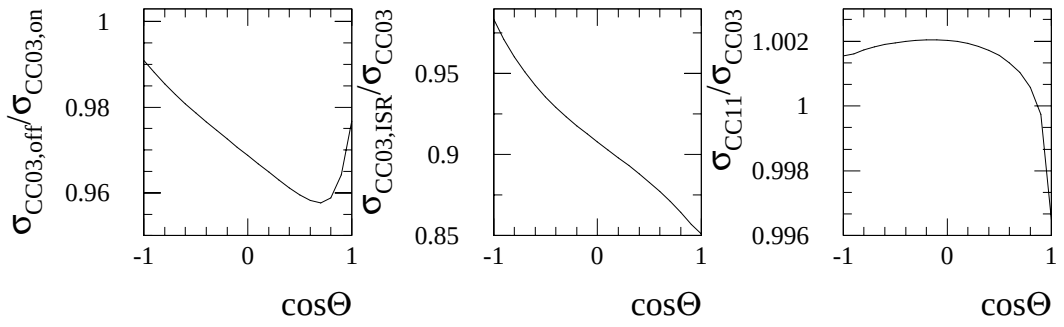

Figure 2.5: Effect of different higher order corrections on the $d\sigma/d\cos\Theta$ distribution. From left to right: effect of taking $\Gamma_W \neq 0$, of including ISR and of considering all the diagrams corresponding to the four-fermion `CC11` process.

2.3.5 Final state interactions

Given the large width of the W boson, its typical decay time is of the order $\tau \sim 1/\Gamma_W \sim$ 0.1 fm, i.e. less than a typical hadronic size of 0.1 fm. Thus the hadronic decay systems of the two W bosons overlap, so that the final state may no longer be considered just the sum of two independent decays. Three different regimes may be distinguished for such interconnection:

- Perturbative: It is supressed for gluon energies $\omega > \Gamma_W$, thus only soft gluons feel the joint action of all four quarks colour charges.

- Non-perturbative in the hadron formation process: Usually modeled by a colour rearrangement between the quarks produced in the two W decays and in the subsequent parton showers.

- Non-perturbative in the purely hadronic phase: Bose-Einstein effects would be included in this regime.

So far, studies have mainly been performed in the context of the W mass measurements at LEP2. They show [16] that the expected effect from colour reconnection within the non-perturbative hadronisation phase may dominate over the one from the perturbative phase. Colour reconnection is not understood from first principles, but several models have been proposed to reproduce its effects [16, 17].

The Bose-Einstein effect is a type of short range (space distances about 1 fm) positive correlation in the momentum space among identical low-momentum bosons (typically pions). It is related to a quantum mechanical interference effect in the unknown multipion wave function in the quark hadronisation process. This effect is absent from typical hadronisation Monte Carlo event generators, which are typically based on probabilistic models without any quantum mechanical interference. Several models exist which try to reproduce the effects of Bose-Einstein correlations. In some of them [18], global weights are assigned to the Monte Carlo events which depend on the momentum distribution of the final state bosons, while in some other [19] the four-momentum of the bosons produced in the hadronisation phase is shifted "by hand" and energy and momentum conservation is restored a-posteriori by an ad-hoc rescaling of the particle momenta.

Chapter 3

Description of the experiment

The analysis presented in this thesis has been carried out using the data produced from e^+e^- collisions at $\sqrt{s} = 189$ GeV in the LEP accelerator (Large Electron Positron collider) at the European Laboratory for Particle Physics (CERN) and collected by the ALEPH detector during the year 1998. In this chapter the LEP collider and the ALEPH detector are briefly described, stressing those points which are more relevant for the TGC measurement using e/μ semileptonic and fully hadronic WW decays.

3.1 The LEP collider

The LEP collider [20, 21] is an e^+e^- storage ring with a 27 Km perimeter sited at CERN near Geneva, Switzerland. It is located in a tunnel 50 to 150 m underground, spanning the French and Swiss territories (see Fig. 3.1).

The reason for such large dimension is the synchrotron radiation. A charged particle moving along a curved path radiates photons which cause an energy loss proportional to $\frac{E^4}{m^4\rho}$, where E and m are the energy and mass of the particle, respectively, and ρ is the bending radius. At LEP the energy loss of a 100 GeV electron is about 3 GeV per turn, which has to be compensated by the acceleration system.

The LEP injection chain (which is shown in Fig. 3.1) starts with a linear accelerator (LINAC) which accelerates electrons and positrons in two stages. In the first stage, the electrons are accelerated up to an energy of 200 MeV. Then, part of these electrons are used to produce positrons by collision with a tungsten target. In the second stage, both electrons and positrons are accelerated up to an energy of 600 MeV. The particles are then

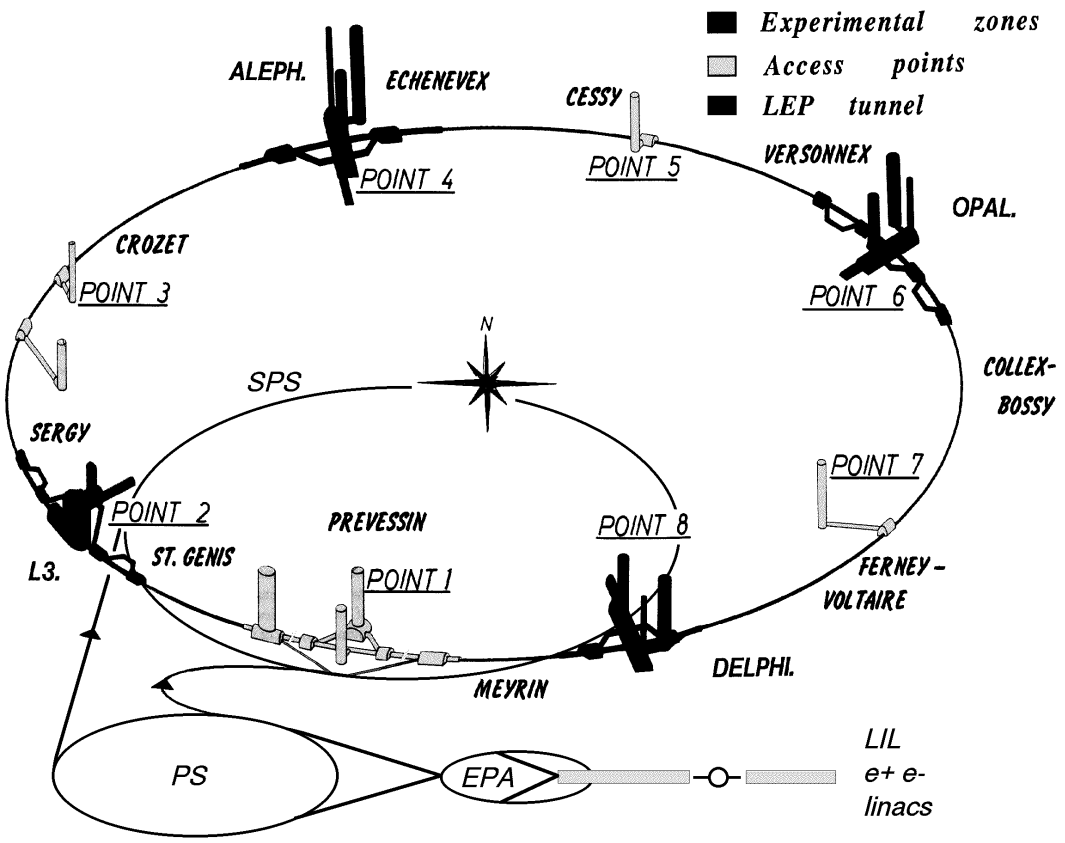

Figure 3.1: Schematic view of the LEP collider, the injector chain and the four interaction points.

injected into a small storage ring (the Electron Positron Accumulator, EPA) where they are separated into bunches and accumulated until the beam intensities achieve nominal values. Afterwards, the leptons are first injected into the Positron Synchrotron (PS) and then into the Super Proton Synchrotron (SPS) storage ring, where they are accelerated up to an energy of 20 GeV. Finally, the particles are injected into the LEP main ring and accelerated until they reach the collision energy.

During the first phase of the accelerator programme (LEP1), finished in 1995, LEP was operated at a centre of mass energy corresponding to the Z^0 production peak ($\sim$91 GeV). During this phase, each experiment collected around four million visible Z^0 decays. The second phase (LEP2) started in summer 1996, when the centre of mass energy reached

the W pair production threshold (∼161 GeV). Since then, the beam energy has been progressively increasing every run in order to study the bosonic sector of the SM and to search for new physics.

3.2 The ALEPH detector

ALEPH (A detector for LEp PHysics) is one of the four detectors at the LEP collider. In this section a brief description of its main subdetectors as well as a summary of the performance underlying the data analysis is presented. The reader may refer to [22, 23, 24] for further details.

ALEPH is a general purpose particle detector, designed to cover as much of the 4π solid angle as possible. It consists of a series of subdetectors, each one specialised in a different task, arranged in an onion-like structure (see Fig. 3.2). A large tracking system immersed in a 1.5 T magnetic field parallel to the beam axis allows to reconstruct the direction and momentum of charged particles with very good resolution. The electromagnetic and hadronic calorimeters measure the energy of charged and neutral particles. Electrons are identified by means of a highly segmented electromagnetic calorimeter, as well as ionisation measurement in the tracking system. Muons are identified using the muon chambers and the final planes of the hadron calorimeter, which provide continuous tracking inside sufficient iron absorber to eliminate the hadrons. There are also highly segmented electromagnetic calorimeters situated at low angle which are dedicated to the integrated luminosity measurement, very important for precise cross section measurements. The trigger system has the purpose of identifying interesting events while keeping the background rate low. Finally, the data acquisition system (DAQ) is the one which puts all the information coming from the subdetectors together and builds events which are then stored for further analysis.

3.2.1 Subdetectors

A short description of the ALEPH subdetectors follows, mainly stressing those characteristics which are relevant to this analysis:

- **Silicon Vertex detector (VDET):** The VDET is a double-sided silicon strip detector with two layers of strips parallel ($r\phi$) and and perpendicular (z) to the beam direction arranged in two coaxial cylinders around the beam pipe. The inner

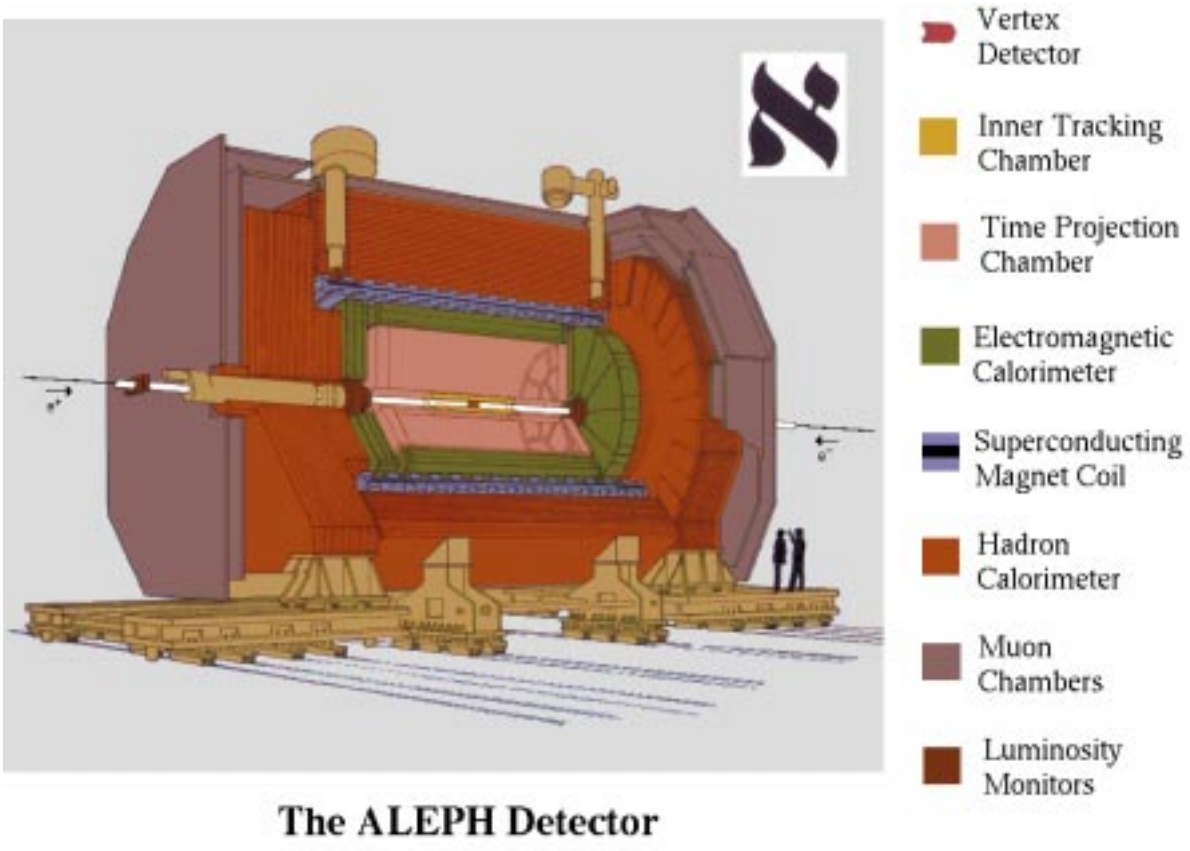

Figure 3.2: The ALEPH detector.

and outer layers have an average radii of 6.5 and 11.3 cm, respectively. The angular acceptance is $| cos\theta | \leq 0.95$ for tracks required to pass through at least one VDET layer.

The VDET measures with high precision the charged particle trajectories very close to the interaction point. It plays a very important role in the identification of long-lived particles, like hadrons containing b or c quarks and τ leptons, by tagging the displaced vertices of their decay products. The VDET hits are also used to provide additional precision for tracks already reconstructed in the outer tracking.

- **Inner Tracking Chamber (ITC):** It is a cylindrical multi-wire drift chamber. It provides up to eight coordinates per track in the $r\phi$ plane by measuring the time taken for ionisation electrons to drift to the sense wires, with an average accuracy

of 150 μm per coordinate. The z coordinate is also determined by measuring the difference in arrival time of the signals at each end of the wires. This has a resolution of a few cm and is not used for tracking.

The ITC provides the only tracking information that is used by the first level trigger (see Sect. 3.2.2) which consists of two (the $r\phi$ projection) and three dimensional charged particle trajectories. This information is available within 3 μs after the beam crossing.

- **Time Projection Chamber (TPC):** It is the main tracking detector in ALEPH and provides up to 21 three-dimensional coordinates per track. It has a cylindrical structure with its axis parallel to the magnetic field. The electric drift field extends from each end plate towards the central membrane that divides the chamber into two halves. When a charged particle traverses the chamber, the electrons produced by ionisation drift towards one end-plate, where their arrival position and time are measured by multi-wire chambers.

  Because of the magnetic field, the trajectory of a charged particle inside the TPC is a helix, and its projection onto the end-plate is an arc of a circle. By measuring the curvature of such arc, the transverse momentum (p_T) of tracks is determined. The inner and outer radii of the TPC are 0.31 and 1.8 m, respectively. Such a large lever arm allows to achieve very good resolution in p_T. The TPC alone has a resolution of $\sigma(1/p_T) = 1.2 \times 10^{-3}(\mathrm{GeV/c})^{-1}$ at 45 GeV. However, $\sigma(1/p_T) = 0.6 \times 10^{-3}(\mathrm{GeV/c})^{-1}$ when the tracking information from VDET, ITC and TPC is combined. The TPC performance is illustrated by Fig. 3.3, where the raw data signals left in the TPC by a hadronic event are shown. The excellent TPC resolution makes possible to *see* the charged particle tracks before any track finding algorithm has been applied.

  In addition to its role as a tracking device, the TPC also contributes to the charged particle identification by measuring their energy loss by ionisation per unit distance (dE/dx), as the size of the signal in the sense-wires (up to 340 for tracks traversing the full radial range) is proportional to this magnitude. Since the dE/dx depends only on the particle velocity for a given material, a combination of dE/dx and momentum measurements allows the mass , and thus the identity, of the charged particle to be deduced. The dE/dx measurement is important for the identification of electrons and also provides useful information to distinguish among pions, kaons and protons in the relativistic rise region.

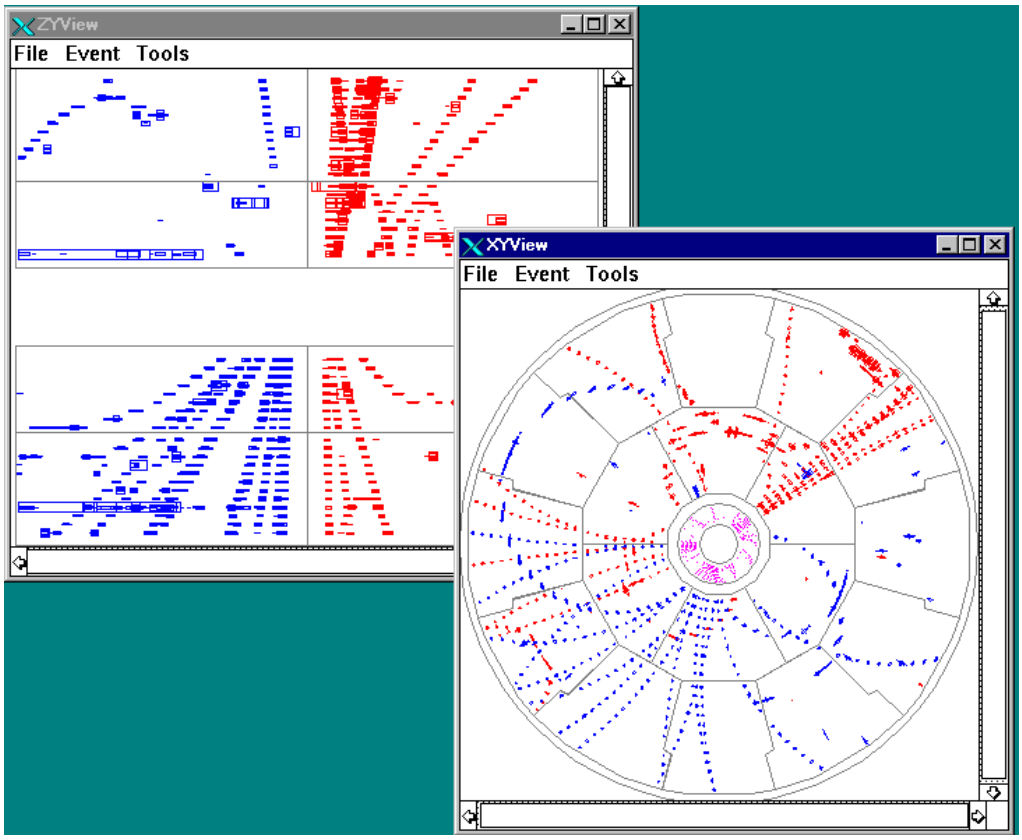

Figure 3.3: An hadronic event from the TPC online event display.

- **Electromagnetic Calorimeter (ECAL):** It is a lead/proportional wire chamber sampling calorimeter of a nominal thickness of 22 radiation lengths. It is formed of a barrel surrounding the TPC, closed at each end by an end-cap. The energy and position of each shower are read out using small cathode pads, which are connected internally to form *towers* which point to the interaction point and provide an average granularity of $0.9^\circ \times 0.9^\circ$. This fine segmentation is important in the identification of photons, electrons and neutral pions. The energy resolution has been parameterised as $\sigma(E)/E = 0.18/\sqrt{E/\mathrm{GeV}} + 0.009$.

- **Hadronic Calorimeter (HCAL):** It is a sampling calorimeter consisting of 23 layers of plastic streamer tubes separated by 5 cm thick iron slabs. It serves two purposes (apart from being the main mechanical support of the ALEPH detector and acting as the return yoke of the magnet): it is used to measure hadronic energy deposits (together with the ECAL), and it is part of the muon identification system.

As in ECAL, cathode pads are connected into projective towers that point towards the interaction point, each with an angular coverage of about $3.7^\circ \times 3.7^\circ$. In addition, a digital signal is recorded for each of the streamer tubes, providing a two-dimensional ($r\phi$) projection of the energy deposition. This is used in the identification of muons.

The energy resolution of the hadron calorimeter for pions at normal incidence is $\sigma(E)/E = 0.85/\sqrt{E/\mathrm{GeV}}$.

- **Muon Chambers:** Muon identification is completed by the muon chambers, which are located beyond the HCAL and consist of two planes of double-layer streamer tubes separated by 40 to 50 cm. The tubes have only a digital readout, giving a measurement of the x and y coordinates for tracks traversing the chambers. The typical accuracy of the muon exit angle is 10 mrad.

The measurement of the luminosity of the colliding electron and positron beams is a vital issue when monitoring the performance of LEP and providing the normalisation for measurements of cross sections. There are three detectors in ALEPH which are specialised in the luminosity measurement by counting small angle Bhabha events:

- **Luminosity Calorimeter (LCAL):** It is a lead/proportional wire chamber sampling calorimeter similar to ECAL in its operation. It consists of two pairs of semicircular modules placed around the beam pipe at each end of the detector whose acceptance in polar angle goes from 45 to 160 mrad. The LCAL Bhabha cross section at 189 GeV is about 4.3 nb, which means that the rate of Bhabha events detected in LCAL at this energy is of the order of 0.3 Hz assuming an instantaneous luminosity of $10^{31}\mathrm{cm}^{-2}\mathrm{s}^{-1}$.

- **Silicon Luminosity Calorimeter (SiCAL):** It is a tungsten/silicon sampling calorimeter whose nominal polar angle coverage goes from 24 to 58 mrad. SiCAL provided the most precise integrated luminosity measurement in ALEPH since it was installed (September 1992) until the end of the LEP1 phase, as it improved the statistical precision of LCAL by covering smaller polar angles. At LEP2, the SiCAL luminosity measurement is not used anymore, because it is partially shadowed by the tungsten masks installed to protect the central detectors from the synchrotron radiation. Instead, it is used to extend the ALEPH acceptance at very low angle (down to 34 mrad).

- **Bhabha Calorimeter (BCAL):** It is a tungsten/plastic scintillator sampling calorimeter consisting of two pairs of semi-circular modules placed around the beam pipe at 7.7 m from the interaction point, behind the focusing quadrupoles. Its polar angle coverage goes from 5 to 9 mrad and it is used for the online luminosity monitoring.

Other devices are installed in the ALEPH detector to monitor the radiation (ARBLIS and RADMON) and the beam background conditions (SAMBA).

3.2.2 Trigger system

Every time an event is recorded by ALEPH, the information from all the subdetectors (more than 500000 electronic channels) has to be read out, collected and combined to make a complete picture of the event. A trigger system is needed to filter the events in order not to exceed the storage information capacity, to minimise the dead time due to the detector read out, and to reduce the time that the TPC gate is open.

The primary purpose of the ALEPH trigger is to identify all events coming from electron-positron annihilation while reducing the rate of background events to a low level. Such background is mainly due to the collision of beam particles with residual gas in the beam pipe, bremsstrahlung radiation photons, off-momentum beam electrons which have hit the beam pipe walls, and cosmic rays traversing the detector top to bottom.

These requirements have led to the development of a three-level trigger scheme. The "lowest" levels are implemented by hardware, to give a fast answer, while the "highest" is implemented by software:

- **Level-1 Trigger:** Delivers a decision within 5 μs, which is fast compared to the beam-crossing rate (22 μs). Its purpose is to identify whether there is a good charged track (from the ITC) and/or particle energy (from the calorimeters) to justify waiting for the TPC trigger signals.

  An important task of the Level-1 trigger is to keep the TPC operational, by deciding when the gate should be kept open for the full drift time ($\sim$ 45 μs).

  Semileptonic and hadronic WW decays, studied in this analysis , are selected with almost 100% efficiency by one or more of the following triggers:

  - Total-energy trigger: Energy deposits in ECAL, demanding at least 6 GeV in the barrel, 3 GeV in either end-cap, or 1.5 GeV in both end-caps.
  - Electron-track trigger: Track segments in the ITC pointing to ECAL deposits with more than 200 MeV.
  - Muon-track trigger: Track segments in the ITC pointing to hits in HCAL.

- **Level-2 Trigger:** Replaces the ITC track information with that from the TPC. It occurs about 50 μs after beam-crossing.

- **Level-3 Trigger:** Checks the Level-2 trigger decision using the data from the whole detector. Its purpose is to reduce the amount of recorded data by eliminating unwanted events before they are written to disk.

3.2.3 Data Acquisition System

Following a Level-2 YES decision from the trigger, the data acquisition system (DAQ) is in charge of handling the information from all the subdetectors. The ALEPH DAQ is organised in a tree structure, with a strong hierarchy, implying that components on the same level do not communicate with each other. The different subdetectors readout is performed in parallel and asynchronously. This information is collected in a microprocessor called the Main Event Builder, where it is synchronised. The data then is sent to a computer in the suface, where it is checked by the Level-3 software and finally it is written to disk.

Immediately after a run has been completed, the raw data is processed by a dedicated computer program named JULIA (Job to Understand Lep Interactions in ALEPH) which does the following:

- reconstructs charged tracks.
- calculates their dE/dx.
- reconstructs the primary vertex and V^0 candidates.
- clusters calorimeter energy and performs an energy flow analysis (see Sect. 3.3.3).
- identifies electrons, muons and photons (see Sect. 3.3.2).

3.3 Event Reconstruction

In this section, the reconstruction processes more relevant to the analysis such as track reconstruction and electron/muon identification are briefly described.

3.3.1 Track reconstruction

Tracks are reconstructed starting in the TPC. Nearby hits are linked to form track segments which are then connected to make tracks by requiring consistency with a helix hypothesis. These track candidates are extrapolated to the inner detectors where consistent hits are assigned. The final track fit, based on Kalman filter [25] techniques uses the coordinates errors and takes into account multiple scattering between each two measurements.

Monte Carlo studies on hadronic Z events show that 98.6% of the tracks that cross at least four pad rows in the TPC are successfully reconstructed. The efficiency of associating a vertex detector hit to an isolated track is about 94% per layer, within the geometrical acceptance. By selecting dimuon events at the Z^0 peak in the angular acceptance of $|\cos\theta| < 0.8$, a transverse momentum resolution of $\sigma(1/p_T) = 0.6 \times 10^{-3}$ $(\mathrm{GeV/c})^{-1}$ is measured. Since the error in the measurement of the polar angle is small, the relative error on the momentum coincides with that on the transverse momentum.

3.3.2 Particle Identification: e and μ

Electron identification

The electron identification is performed using two independent measurements: the dE/dx measurement from the TPC and the energy deposition measured in ECAL, compared to the track momentum and the expected shape of the shower. These two measurements are complementary since dE/dx is more effective at low momentum and the shape of showers in ECAL at high momentum. This information is expressed in terms of normally distributed estimators, which are defined here:

- dE/dx estimator: It is calculated by comparing the measured ionisation (I) to that expected for an electron ($\langle I \rangle$) normalised to the dE/dx resolution(σ_I) as

$$R_I = \frac{I - \langle I \rangle}{\sigma_I} \,. \tag{3.1}$$

- Transverse shower shape estimator: It is defined using the four towers in ECAL closest to the extrapolated track as

$$R_T = \frac{E_4/p - \langle E_4/p \rangle}{\sigma_{E_4/p}} , \tag{3.2}$$

where E_4 is the total energy deposited in the selected towers, p is the momentum of the charged track, $\langle E_4/p \rangle$ is the mean energy fraction deposited by an electron in the four central towers, and $\sigma_{E_4/p}$ is the resolution expected for this ratio.

The R_T estimator reflects the compactness of the electromagnetic shower and is the most efficient for hadron rejection when the momentum of the track is high.

- Longitudinal shower shape estimator: It is based on the inverse of the mean position of the longitudinal energy deposition in the shower, defined as

$$X_L = \frac{E_4}{\sum_{i=1}^{4} \sum_{j=1}^{3} E_i^j S_j} , \tag{3.3}$$

where E_i^j is the energy deposited in the tower i of segment j in depth of the calorimeter, and S_j is the mean depth of energy deposition in that segment. R_L is then defined as

$$R_L = \frac{X_L - \langle X_L \rangle}{\sigma_{X_L}} . \tag{3.4}$$

The use of these estimators for the $e\nu q\bar{q}$ selection performed in this analysis is discussed in section 5.2.1.

Muon identification

Muons are identified by using the tracking capabilities of HCAL and the information from the muon chambers.

Tracks are extrapolated (as if they were a muon) through the calorimeter material taking into account a detailed magnetic field map and estimated energy losses. A "road" is opened around the extrapolated track, with a width of three times the estimated extrapolation uncertainty due to multiple scattering. A calorimeter plane is said to be expected to fire if the extrapolated track intersects it within an active region, and the plane is said to have fired if a digital hit lies within the multiple scattering road. For a hit to be counted, the number of adjacent firing tubes must not be greater than three.

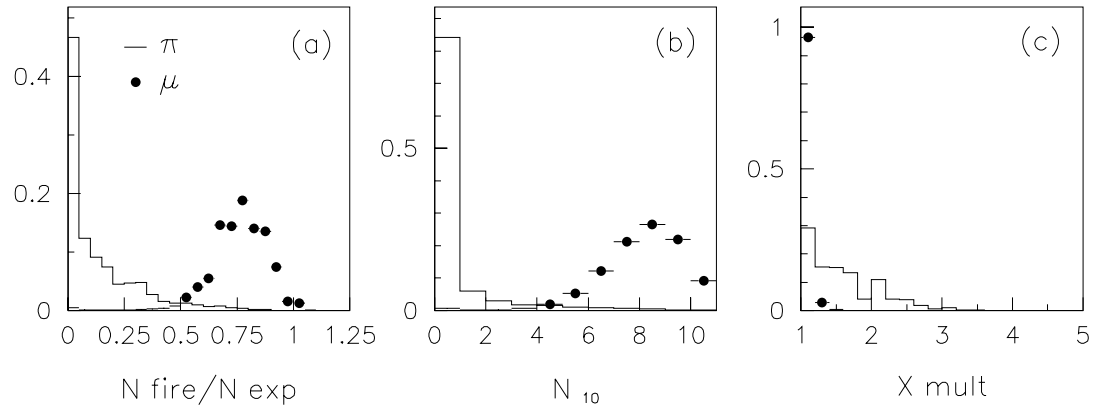

Figure 3.4: Distribution of (a) N_{fire}/N_{exp}, (b) N_{10} and (c) X_{mult}, for muons (points) and pions (solid line), with $N_{exp} > 10$. The plots have been normalised to equal areas and the vertical scale is arbitrary.

The cuts used to define a penetrating track are: $N_{fire}/N_{exp} \geq 0.4$, $N_{exp} \geq 10$, and $N_{10} > 4$, where N_{fire}, N_{exp} and N_{10} are the number of actually firing planes, the number of expected planes, and the number of firing planes within the last ten expected for the track, respectively. To enhance the rejection power against hadron background the average hit multiplicity per fired plane X_{mult} is used. The cut applied for muon identification is $X_{mult} < 1.5$. In Fig. 3.4 the distributions of N_{fire}/N_{exp}, N_{10} and X_{mult} for muons coming from $Z^0 \rightarrow \mu^+\mu^-$ events are compared to those of pions produced in τ decays.

A track is defined to have hit the muon chambers if at least one of the two chambers has a hit whose distance from the extrapolated track is less than four times the estimated standard deviation from multiple scattering. Monte Carlo simulations predict that while about 94% of the muons which have been identified in HCAL are associated to a muon chamber hit, only about 20% of the misidentified hadrons are associated. Hence, the requirement of associated hits in the muon chambers in addition to the HCAL criteria, is a powerful tool for background rejection.

The use of these estimators for the $\mu\nu q\bar{q}$ selection performed in this analysis is discussed in section 5.2.1.

3.3.3 Energy Flow determination

The Energy Flow algorithm is meant to improve the visible energy resolution in ALEPH by combining the measurements of track momenta, calorimeter energy deposits and particle identification. It builds a set of *energy flow objects* (electrons, muons, photons, charged and neutral hadrons) which should be a close representation of the stable particles actually produced in the collision.

First of all, a cleaning procedure is applied in order to reject badly reconstructed charged tracks and noise from the calorimeters. Then the charged particle tracks are extrapolated to the calorimeters, and groups of topologically connected tracks and clusters (called *calorimeter objects*) are formed. From these calorimeter objects the following pieces are then removed:

- charged tracks identified as electrons, together with the associated energy in ECAL (if the difference between this energy and the track momentum is larger than three times the expected resolution, it is assumed to come from a bremsstrahlung photon, and is counted as neutral electromagnetic energy).
- charged tracks identified as muons, together with a maximum of 1 GeV from the closest associated ECAL deposit (if any) and a maximum of 400 MeV per plane fired around the extrapolation of the muon track from the corresponding HCAL cluster.
- identified photons and π^0's (they are counted as neutral electromagnetic energy).

At this stage, the only particles left in the calorimeter object should be charged and neutral hadrons. Charged hadrons are identified as all the remaining charged tracks, and the pion mass is assumed for them. Neutral hadrons are then identified as a significant excess of calorimeter energy.

After using the energy flow algorithm, the energy resolution for hadronic Z decays is parameterised as

$$\frac{\sigma(E)}{E} = \frac{(0.59 \pm 0.03)}{\sqrt{E/\mathrm{GeV}}} + (0.6 \pm 0.3),$$

which represents a big improvement with respect to which what would be obtained from calorimeters alone.

Chapter 4

Description of the Method

Several statistical techniques have been proposed for the extraction of the TGCs in $e^+e^- \to W^-W^+$ [26]. All of them make use of both the total W pair cross section and the angular distributions of the fermions in the final state. However, the way the information on the TGCs is extracted from the angular distributions differs considerably from one method to the other.

The first section in this chapter is devoted to describe the analysis of the angular distributions. The method of the *optimal observables* is presented and its use in the context of this analysis is justified. Some studies using Monte Carlo events at the parton level are carried out to understand the impact of the physics and experimental effects on this extraction method. Finally, the analysis of the total event rate in terms of the TGCs is described in the second section.

4.1 Analysis of the angular distributions: Optimal observables

4.1.1 The simplest case

Assume there is a certain physics process whose probability density function (p.d.f.) can be written in terms of the phase space variables of each event $\vec{\Omega}$ as

$$\mathcal{P}(\vec{\Omega}|\alpha) = f(\vec{\Omega}) + \alpha\, g(\vec{\Omega}) \,, \tag{4.1}$$

where α represents some parameter to be determined experimentally, and the functions f and g satisfy that $\int f(\vec{\Omega})d\vec{\Omega} = 1$ and $\int g(\vec{\Omega})d\vec{\Omega} = 0$.

Given a sample of N events described by this p.d.f. $\{\vec{\Omega}_i; i = 1, N\}$, the α parameter can be estimated by maximising the likelihood $\mathcal{L}(\alpha, \{\vec{\Omega}_i\})$

$$\mathcal{L}(\alpha, \{\vec{\Omega}_i\}) \equiv \prod_{i=1}^{N} \mathcal{P}(\vec{\Omega}|\alpha) \,, \tag{4.2}$$

$$0 = \frac{\partial}{\partial\alpha} \log \mathcal{L} \Big|_{\alpha=\hat{\alpha}} = \sum_{i=1}^{N} \frac{g(\vec{\Omega}_i)}{f(\vec{\Omega}_i) + \hat{\alpha}\, g(\vec{\Omega}_i)} = \sum_{i=1}^{N} \frac{\omega(\vec{\Omega}_i)}{1 + \hat{\alpha}\, \omega(\vec{\Omega}_i)} \,, \tag{4.3}$$

which depends only on the kinematic variable defined by

$$\omega(\vec{\Omega}) \equiv \frac{g(\vec{\Omega})}{f(\vec{\Omega})}. \tag{4.4}$$

Therefore, a maximum likelihood fit of the one-dimensional distribution of the variable ω leads to the same equation and yields then the same result $\hat{\alpha}$ with the same error

$$\frac{1}{V(\hat{\alpha})} = -E\left[\frac{\partial^2 \log \mathcal{L}}{\partial\alpha^2}\right]_{\alpha=\hat{\alpha}} = N\left\langle \frac{\omega^2}{(1+\hat{\alpha}\omega)^2} \right\rangle \tag{4.5}$$

as the one provided by the multi-dimensional analysis of the full $\vec{\Omega}$ distribution. For this reason the observable defined in Eq. (4.4) is denoted as *optimal observable*.

Furthermore, it should be noticed from Eq. (4.3) that, for small values of $\hat{\alpha}$, the maximum likelihood estimator is essentially equivalent to the mean value $\langle\omega\rangle = \frac{1}{N}\sum_{i=1}^{N} \omega(\vec{\Omega}_i)$. Therefore, in the limit $\hat{\alpha} \to 0$, not only all the information in the multi-dimensional phase space $\vec{\Omega}$ can be projected into only one dimension $\omega(\vec{\Omega})$, but also this information is fully contained in the first moment of such variable.

Optimal observables of these kind have already been used in the past for physics analysis where the condition (4.1) held, for instance the tau polarisation measurement [27].

4.1.2 Optimal Observables and TGCs

Since the matrix element for the reaction $e^+e^- \to W^-W^+ \to f_1\bar{f}_2\ f_3\bar{f}_4$ depends linearly on the TGCs (see Table 2.2), the differential cross section for this process can be written as a second order polynomial in these couplings

$$\frac{d\sigma}{d\vec{\Omega}} = S_0(\vec{\Omega}) + \sum_i S_{1,i}(\vec{\Omega}) g_i + \sum_{i,j} S_{2,ij}(\vec{\Omega}) g_i g_j \,, \tag{4.6}$$

where the sums run over those TGCs which are allowed to deviate from their SM value (in this analysis $g_i \equiv \Delta g_1^Z, \Delta\kappa_\gamma$ and λ_γ, as discussed in chapter 2) and $\vec{\Omega}$ stands for the phase

space variables defining the final state. Assuming massless fermions and after applying energy and momentum conservation, all the kinematic information of a given event is contained in eight variables (See Fig. 4.1):

- The two W invariant masses: k_-^2 and k_+^2.
- The W^- polar and azimuthal production angles with respect to the incoming e^- in the e^+e^- rest frame: Θ and Φ.
- The polar and azimuthal decay angles of the fermion from the W^- decay, with respect to the flight direction of the W^-, measured in its rest frame: θ_-^* and ϕ_-^*.
- The polar and azimuthal decay angles of the anti-fermion from the W^+ decay, with respect to the flight direction of the W^+, measured in its rest frame: θ_+^* and ϕ_+^*.

The argument presented in Sect. 4.1.1 for the simplest case, in which the p.d.f. depends linearly on a given unknown parameter, can be extended [28] to having several parameters and observables with non-vanishing expectation values at $g_i = 0$. In general it can be shown [29] that, for a cross section like (4.6) showing a quadratic dependence with the couplings, all the phase space information is contained in the set of observables

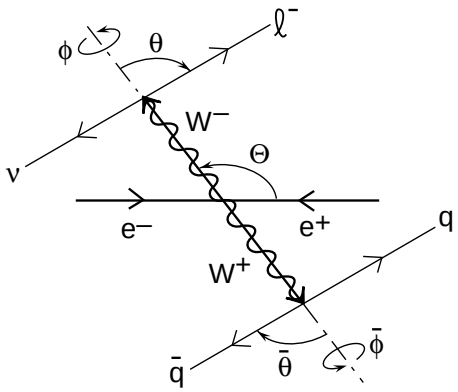

Figure 4.1: Kinematic variables defining an $e^+e^- \to W^+W^- \to \ell\nu q\bar{q}$ event.

$$\mathcal{O}_{1,i} \equiv \frac{S_{1,i}(\vec{\Omega})}{S_0(\vec{\Omega})}\,, \tag{4.7}$$

$$\mathcal{O}_{2,ij} \equiv \frac{S_{2,ij}(\vec{\Omega})}{S_0(\vec{\Omega})}\,, \tag{4.8}$$

hence denoted as *optimal observables*.

To have such phase space directions in which the full information is projected might be indeed very useful when the number of couplings g_i to be determined is small. However, if several couplings are simultaneously fitted, the number of observables soon exceeds that of the phase space variables.

As already pointed out in Sect. 4.1.1, it can be shown (a general proof in case of having several couplings and observables with non-vanishing expectation values for $g_i = 0$

can be found in [28]) that, in the limit of vanishing couplings, all the information of the optimal observable distributions is contained in their first moments. Then, if instead of considering the complete distributions, only the first moments are used as observables, it becomes straightforward to increase the dimensionality of the fit.

Two approaches might be considered to try to reach the limit in which all the information is contained in the first moment of the observable distributions:

i) Iterative method

In case the measurement yields values for the couplings which are different from zero $g_i = \tilde{g}_i \neq 0$, a set of optimal observables can still be found. In order to see this explicitly, the differential cross section (4.6) can be re-written as an expansion around the value $\tilde{g}_i$ of the couplings where the measurement happens to lie

$$\frac{d\sigma}{d\vec{\Omega}} = \tilde{S}_0(\vec{\Omega}) + \sum_i \tilde{S}_{1,i}(\vec{\Omega})(g_i - \tilde{g}_i) + \sum_{i,j} \tilde{S}_{2,ij}(\vec{\Omega})(g_i - \tilde{g}_i)(g_j - \tilde{g}_j) \,, \tag{4.9}$$

with

$$\tilde{S}_0(\vec{\Omega}) \equiv S_0(\vec{\Omega}) + \sum_i S_{1,i}(\vec{\Omega})\, \tilde{g}_i + \sum_{i,j} S_{2,ij}(\vec{\Omega})\, \tilde{g}_i \tilde{g}_j \,, \tag{4.10}$$

$$\tilde{S}_{1,i}(\vec{\Omega}) \equiv S_{1,i}(\vec{\Omega}) + 2 \sum_j S_{2,ij}(\vec{\Omega})\, \tilde{g}_j \,, \tag{4.11}$$

$$\tilde{S}_{2,ij}(\vec{\Omega}) \equiv S_{2,ij}(\vec{\Omega}) \,. \tag{4.12}$$

New observables can then be built

$$\tilde{\mathcal{O}}_{1,i} \equiv \frac{\tilde{S}_{1,i}(\vec{\Omega})}{\tilde{S}_0(\vec{\Omega})} \tag{4.13}$$

from (4.9) whose first moments will yield the smallest possible statistical errors on the estimated couplings, if the $\tilde{g}_i$ are equal to the measured values of the g_i. It can be shown [30] that, the set of observables given by (4.13) is the only set of n integrated observables that measures the n couplings with minimum error. There is hence no choice of observables that would be optimal for *all* values of the actual coupling parameters.

To approach this limit in which the estimated g_i coincide with $\tilde{g}_i$ an iterative method can be used, as suggested in [30].

The fact that the observable $\langle \tilde{\mathcal{O}}_1 \rangle$ is, after iteration, equivalent to the log-likelihood estimator can be visualised in Fig. 4.2a, where the results of several Monte Carlo

experiments are compared. In each of these experiments, Δg_1^Z has been extracted from a set of WW events at the generator level using both methods. In Fig. 4.2b the log-likelihood results are compared to those obtained by using $\langle \mathcal{O}_1 \rangle$ (i.e. without iteration). This time the estimators are only equivalent for those experiments whose measurement happened to lie at $\Delta g_1^Z = 0$, as expected.

ii) Using second order observables

A different strategy might be adopted to regain information in those cases where the measurement happens to lie at $g_i \neq 0$: to consider the mean values of both the first order (4.7) and second order (4.8) observables. This procedure avoids the complications that might appear when iterating, such as indefinite results due to oscillation around double-minima structures, by relying on the additional sensitivity to the couplings that the second order observable might incorporate.

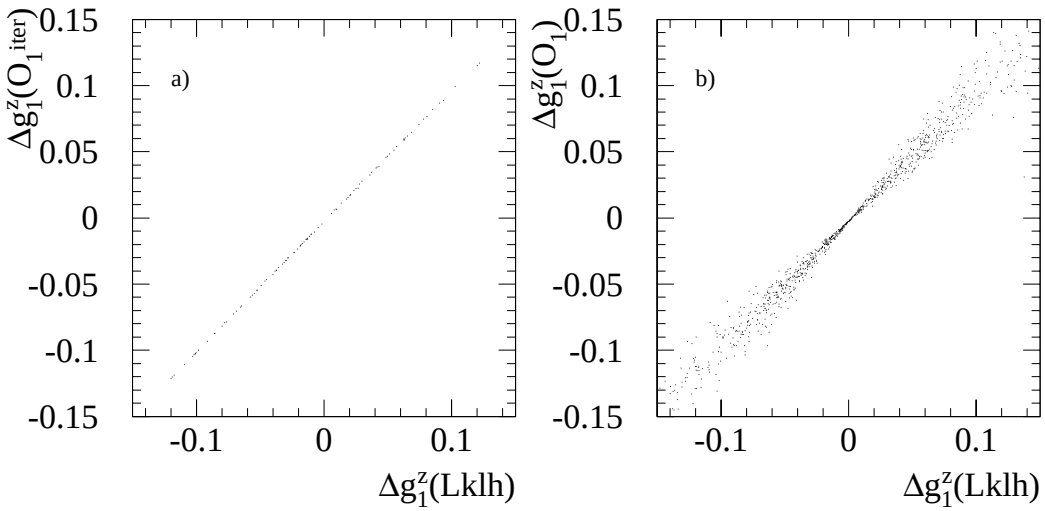

Figure 4.2: Comparison of log-likelihood, $\langle \tilde{\mathcal{O}}_1 \rangle$ and $\langle \mathcal{O}_1 \rangle$ estimators of Δg_1^Z for WW Monte Carlo events.

In order to extract the unknown couplings from the measured mean values of the optimal observables $\langle \mathcal{O}_i \rangle$, a prediction for the expected value of such observables as a function of the couplings is needed. The expected value of any function $f(\vec{\Omega})$ of the phase

space variables is given by

$$E[f(\vec{\Omega})] = \frac{\int f(\vec{\Omega}) \frac{d\sigma}{d\vec{\Omega}} d\vec{\Omega}}{\int \frac{d\sigma}{d\vec{\Omega}} d\vec{\Omega}} \,. \tag{4.14}$$

Thanks to the polynomial dependence of the cross section (4.6) with the couplings g_i, this expected value has a simple analytical expression in terms of the g_i

$$E[f] = E_0[f] + \frac{\sum_i c_{ij}\, g_j + \sum_{jk} q_{ijk}\, g_j g_k}{1 + \sum_j \sigma_{1,j}\, g_j + \sum_{jk} \sigma_{2,jk}\, g_j g_k} \,, \tag{4.15}$$

where the coefficients can be written as

$$\begin{aligned} c_{ij} &= V_0[f\,,\, S_{1,j}/S_0]\,, & q_{ijk} &= V_0[f\,,\, S_{2,jk}/S_0]\,, \\ \sigma_{1,j} &= E_0[S_{1,j}/S_0]\,, & \sigma_{2,jk} &= E_0[S_{2,jk}/S_0]\,, \end{aligned} \tag{4.16}$$

being $E_0[f] = (\int d\vec{\Omega} f S_0)/(\int d\vec{\Omega} S_0)$ the expectation value of the function $f(\vec{\Omega})$ and $V_0[f,g] = E_0[fg] - E_0[f]E_0[g]$ the covariance of $f(\vec{\Omega})$ and $g(\vec{\Omega})$, both at SM couplings.

Using (4.15) the expected values $E[\mathcal{O}_i]$ can be expressed in terms of the g_i, allowing then the couplings to be extracted from the measured $\langle \mathcal{O}_i \rangle$ by minimising

$$\chi^2(\vec{g}) = \sum_{ij} (\langle \mathcal{O}_i \rangle - E[\mathcal{O}_i])\; N V(\mathcal{O})^{-1}{}_{ij}\; (\langle \mathcal{O}_j \rangle - E[\mathcal{O}_j]) \,, \tag{4.17}$$

where N is the number of events in the data, and $V(\mathcal{O})_{ij}$ is the covariance matrix of the observables $\mathcal{O}_i$. Note that, in case of multi-dimensional fits where both the first and second order observables are included, the sum in (4.17) runs not only over couplings but also over observable type.

As seen from Eqs. (4.15) and (4.16), the prediction of the $E[\mathcal{O}_i]$ in terms of the g_i involves coefficients which are just first and second moments of certain functions of the phase space variables at vanishing couplings. Therefore, they can be readily computed using a reference set of Monte Carlo events generated with SM couplings. It is worth to note that this procedure is equivalent to the so called *reweighting technique*, in which the $E[\mathcal{O}_i](\vec{g})$ would be obtained as a weighted average

$$E[\mathcal{O}_i](\vec{g}) = \frac{\sum_{j=1}^{N_{MC}} \omega(\vec{\Omega}_j; \vec{g})\; \mathcal{O}_i(\vec{\Omega}_j)}{\sum_{j=1}^{N_{MC}} \omega(\vec{\Omega}_j; \vec{g})} \tag{4.18}$$

of the $\mathcal{O}_i$ values for the reference Monte Carlo events, where a weight

$$\omega(\vec{\Omega};\vec{g}) = \frac{\frac{d\sigma}{d\vec{\Omega}}(\vec{\Omega};\vec{g})}{\frac{d\sigma}{d\vec{\Omega}}(\vec{\Omega};\vec{g}=\vec{0})} \tag{4.19}$$

is given to each event in order to mimic the behaviour of a sample of events with non-zero couplings.

In this way, all those effects such as detector resolution or selection cuts are automatically taken into account in the $E[\mathcal{O}_i](\vec{g})$ prediction by using a reference sample of Monte Carlo events which include all them.

A set of 100000 Monte Carlo WW events generated at SM TGCs has been used to predict some of the optimal observables. These observables have been built by using the `KORALW-CC03` matrix element as defined in Eqs. (4.7) and (4.8). As an example, the expected values $E[\mathcal{O}_{1,\Delta g_1^Z}]$ and $E[\mathcal{O}_{2,\Delta g_1^Z}]$ as functions of the coupling Δg_1^Z are shown in Fig. 4.3. From this figure it is clear that, near the vanishing coupling region, the first order observable $\mathcal{O}_{1,\Delta g_1^Z}$ is maximally sensitive to Δg_1^Z while the $\mathcal{O}_{2,\Delta g_1^Z}$ dependence on the parameter is almost flat, as expected. On the other hand, as the coupling deviates from zero, the loss in sensitivity of the first order optimal observable is somehow compensated by a stronger dependence on the parameter of the second order one.

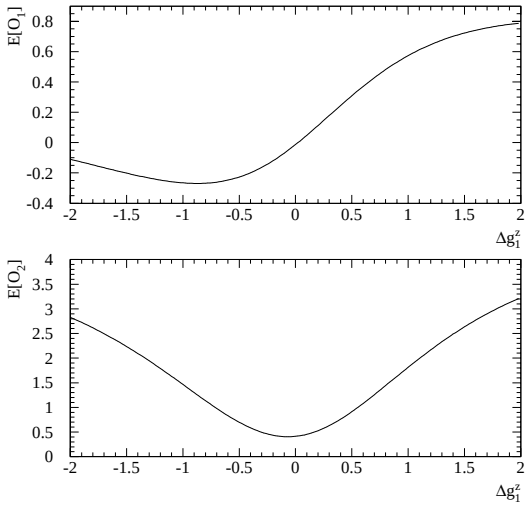

Figure 4.3: Dependence of the expected values of the $\mathcal{O}_{1,\Delta g_1^Z}$ and $\mathcal{O}_{2,\Delta g_1^Z}$ observables versus Δg_1^Z.

Sensitivity

To quantify the performance of the optimal observables it is useful to define their *sensitivity* $\mathcal{S}$ as the inverse of the uncertainty they yield for a given coupling, once the dependence on the statistics has been factorised. Hence, the sensitivity of the mean value of an optimal observable $\langle\mathcal{O}\rangle$ when measuring a coupling g can be defined as

$$\mathcal{S} \equiv \frac{\left|\frac{d\langle\mathcal{O}\rangle}{dg}\right|}{\sqrt{V(\mathcal{O})}} \,. \tag{4.20}$$

This sensitivity is then related to the coupling error δg in the regime in which the $\langle \mathcal{O} \rangle$ depends linearly on this coupling. This is the limit of vanishing δg or, equivalently, high statistics, where

$$\frac{1}{\delta g \sqrt{N}} \xrightarrow[N \to \infty]{} \mathcal{S} \, . \tag{4.21}$$

In this sense, $\mathcal{S}$ provides a *local* measurement of the power of $\langle \mathcal{O} \rangle$ in determining the coupling g.

When more than one observable is used, the global sensitivity can be determined from the general χ^2 in (4.17) and from (4.21), and turns to be

$$\mathcal{S} = \sqrt{\sum_{ij} \left| \frac{d\langle \mathcal{O}_i \rangle}{dg} \right| V(\mathcal{O})^{-1}{}_{ij} \left| \frac{d\langle \mathcal{O}_j \rangle}{dg} \right|} \, . \tag{4.22}$$

where the sum runs over those observables involved in the measurement.

The sensitivities of three different approaches using optimal observables have been computed for several Δg_1^Z values and are shown in Fig. 4.4. In the first approach, only the mean value of the first order observable $\langle \mathcal{O}_1 \rangle$ defined in (4.7) is used in the fit. In the second approach, the mean value of the second order observable $\langle \mathcal{O}_2 \rangle$ defined in (4.8) is added as well. The observables used in these first two approaches are built from the differential cross section (4.6) expanded around $g = 0$. Finally, the mean value of the first order observable $\langle \tilde{\mathcal{O}}_1 \rangle$ defined in (4.13) is used in the third approach. This observable is re-built, at every coupling value g, from the differential cross section (4.9) expanded around that particular value $\tilde{g} = g$.

Figure 4.4a shows the sensitivities of these three approaches when applied to Monte Carlo WW events at the generator level[1]. The solid line corresponds to the sensitivity of the observable $\langle \tilde{\mathcal{O}}_1 \rangle$. Since $\tilde{\mathcal{O}}_1$ is built using the differential cross section re-expanded around each coupling point, its definition is different at every point in the curve. As already discussed, this sensitivity is equivalent to that one reachable by a log-likelihood estimator, thus being maximal.

The dashed curve in Fig. 4.4a represents the sensitivity of the observable $\langle \mathcal{O}_1 \rangle$. Opposite to $\tilde{\mathcal{O}}_1$, the definition of this observable remains unchanged along the curve. The sensitivity is now maximal at $g = 0$, by definition, and equal to that one of $\langle \tilde{\mathcal{O}}_1 \rangle$, since

[1] Perfect flavour tagging for the four fermions in the final state and efficiency equal one have been assumed.

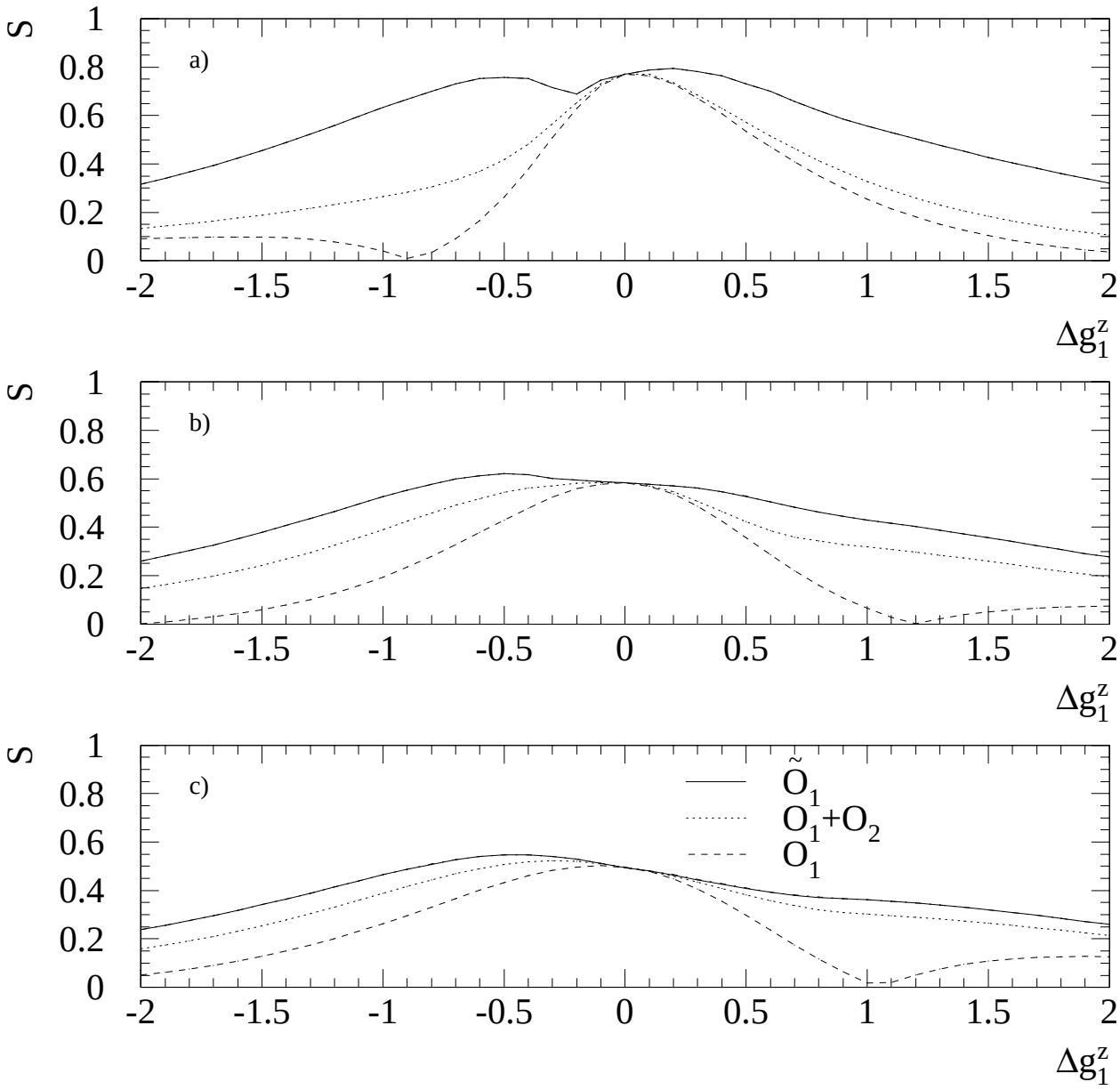

Figure 4.4: Comparison of the sensitivities for different optimal observables approaches in various conditions: a) Generator level, b) Including the two-fold ambiguity of semileptonic decays, c) Fully reconstructed $e\nu q\bar{q}$ events accepted by a selection.

both observables coincide at this point. The sensitivity of $\langle \mathcal{O}_1 \rangle$ drops fairly rapidly away from $g = 0$ and even vanishes in some coupling region.

Finally, the sensitivity of the $\langle \mathcal{O}_1 \rangle$ and $\langle \mathcal{O}_2 \rangle$ observables combined is shown in Fig. 4.4a as a dotted line. Again, it equals that of the two previous approaches at $g = 0$. This reflects the fact that the information added by the second order observable vanishes at this point. Nevertheless, it helps in incorporating additional sensitivity in the rest of the parameter space.

Figures 4.4b and 4.4c illustrate how this picture changes when experimental effects are successively included. In Fig. 4.4b, the two-fold ambiguity due to the uncertainty in the quark flavours tagging (see Sect. 4.1.3) has been included, assuming that the measurement is performed using a sample of W pairs decaying semileptonically. The sensitivities in Fig. 4.4c have been computed using a fully reconstructed sample of four-fermion Monte Carlo events accepted by the $e\nu q\bar{q}$ selection described in Sect. 5.2.1, therefore incorporating detector resolution and acceptance effects.

What should be noticed from the plot sequence in Fig. 4.4 is that the more experimental effects are taken into account, the smaller the difference between the $\langle \tilde{\mathcal{O}}_1 \rangle$ and $\langle \mathcal{O}_1 \rangle + \langle \mathcal{O}_2 \rangle$ sensitivities tends to be. However, even after including experimental resolution effects, the $\langle \mathcal{O}_1 \rangle + \langle \mathcal{O}_2 \rangle$ sensitivity is always slightly worse than the optimal one, specially in the coupling regions far from zero. In the vicinity of vanishing coupling, both approaches become equivalent, therefore one expects that in the high statistics limit the sensitivity difference becomes effectively negligible. In order to see if this limit holds for the cases studied in this analysis, the selection and reconstruction procedures described in Chapter 5 have been applied to signal and background Monte Carlo events, which have been used to build several samples with the size of the data collected in 1998 ($\int \mathcal{L} = 174.2$ pb^{-1}). The TGCs have then been extracted from each sample by using both the iterative procedure with only one observable $\langle \tilde{\mathcal{O}}_1 \rangle$ and also the combination of the two observables $\langle \mathcal{O}_{1,2} \rangle$ with no iteration. In the first case, the iterative procedure is stopped if the variation found in the fitted coupling is smaller than 50 times the fitted error. If the fit does not converge after 10 iterations, the iterative procedure is stopped and the observable $\tilde{\mathcal{O}}_1$ is defined at coupling equal zero.

The distributions of the number of iterations before convergence are shown in Fig. 4.5 for the different couplings and selections. It should be noted that for $\Delta\kappa_\gamma$, the coupling to which there is less sensitivity, between 14% and 16% of the experiments do not con-

verge before 10 iterations. In the purely hadronic WW decay channel, where the angular information is smeared out due to the fact that the charge of the W bosons is not unambiguously tagged, this also happens for the other two couplings λ_γ and Δg_1^Z, for which 7% and 9% of the fits do not converge, respectively.

		$e\nu q\bar{q}$ selection	$\mu\nu q\bar{q}$ selection	$q\bar{q}q\bar{q}$ selection
Δg_1^Z	$\langle\tilde{\mathcal{O}}_1\rangle_{iter}$	0.109 ± 0.003	0.107 ± 0.003	0.154 ± 0.003
	$\langle\mathcal{O}_1\rangle + \langle\mathcal{O}_2\rangle$	0.112 ± 0.003	0.108 ± 0.003	0.142 ± 0.003
$\Delta\kappa_\gamma$	$\langle\tilde{\mathcal{O}}_1\rangle_{iter}$	0.443 ± 0.010	0.408 ± 0.009	0.414 ± 0.009
	$\langle\mathcal{O}_1\rangle + \langle\mathcal{O}_2\rangle$	0.393 ± 0.009	0.381 ± 0.009	0.389 ± 0.009
λ_γ	$\langle\tilde{\mathcal{O}}_1\rangle_{iter}$	0.120 ± 0.003	0.110 ± 0.003	0.183 ± 0.004
	$\langle\mathcal{O}_1\rangle + \langle\mathcal{O}_2\rangle$	0.120 ± 0.003	0.108 ± 0.003	0.173 ± 0.004

Table 4.1: RMSs of the coupling estimator distributions for the three studied final states. The iterative procedure ($\langle\tilde{\mathcal{O}}_1\rangle_{iter}$) performance is compared to the combination of the first and second order observables ($\langle\mathcal{O}_1\rangle + \langle\mathcal{O}_2\rangle$).

The RMS of the obtained fitted coupling distributions, which estimate the expected error of the measurements, are compared in Table 4.1 for the iterative (noted $\langle\tilde{\mathcal{O}}_1\rangle_{iter}$) and first plus second order observables (noted $\langle\mathcal{O}_1\rangle + \langle\mathcal{O}_2\rangle$) fitting procedures. From these results it can be concluded that, with the available statistics, the expected errors are small enough so that both fitting techniques show essentially the same sensitivity. Furthermore, for those couplings where the iterative procedure does not converge in a sizeable fraction of the experiments ($\Delta\kappa_\gamma$ for all selections and the three couplings for the purely hadronic selection), the expected error is found to be smaller if the first and second order observables are used instead of iterating, as some sensitivity is picked up by $\langle\mathcal{O}_2\rangle$.

After seeing these results, it seems not justified to try to reach the optimal sensitivity by using the iterative fitting procedure (technically, more CPU-consuming). For this reason, in this work the TGCs have been extracted by means of the alternative method in which the mean values of both the first and second order observables, defined from the differential cross section expanded around vanishing couplings, are used.

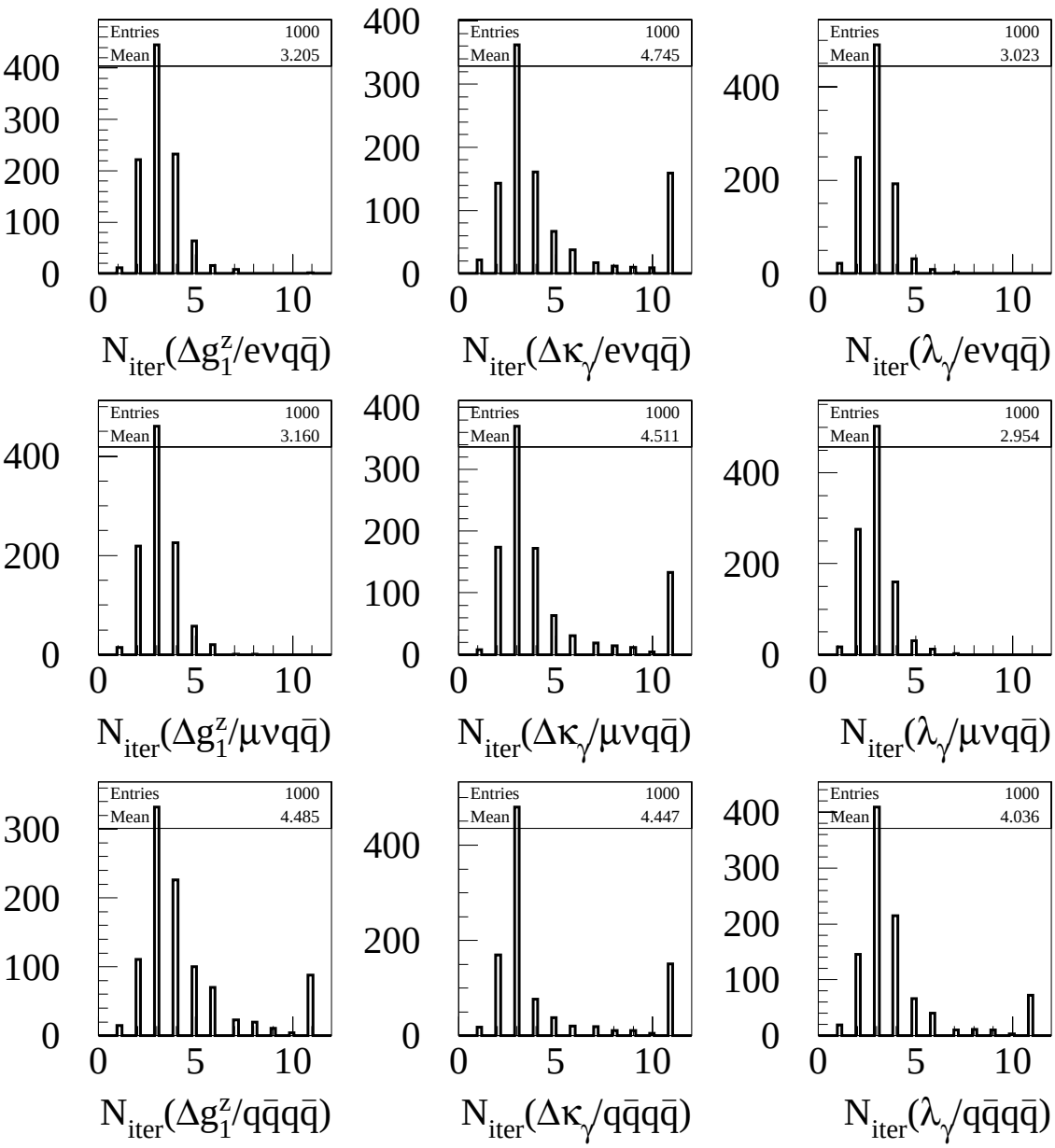

Figure 4.5: The number of iterations needed before convergence when extracting the TGCs using the *iterative procedure* described in the text. These results are obtained by fitting many Monte Carlo samples containing the same number of events as observed in the data. The selection and reconstruction procedures used are those described in Chapter 5.

4.1.3 Experimental Features in Four-fermion Final States

The goal of this analysis is to perform a direct measurement of the TGCs by using W pair decays into two different topologies:

- $e^+e^- \to W^+W^- \to \ell\nu q\bar{q}$ with $\ell = e, \mu$, referred to as semileptonic WW events throughout this thesis.
- $e^+e^- \to W^+W^- \to q\bar{q}q\bar{q}$, referred to as purely hadronic WW events.

When reconstructing a W pair event from these topologies, some ambiguities are faced, which arise due to the lack of knowledge about the quarks flavour. The quark pairs produced in $W \to q\bar{q}$ decays belong to the same family in 95% of the cases, since mixing between quark families is highly suppressed by the CKM matrix elements. For this reason, any hadronic final state in W pair events at LEP energies, must come from u, d, c or s quarks. The b production is essentially forbidden by the absence of phase space to produce t quarks.

In the semileptonic decays, the charge of the W is directly determined by the charge of the tagged lepton. Assuming that the neutrino four-momentum can be reconstructed by imposing energy and momentum conservation, the decay angles from the leptonic decay (θ_ℓ, ϕ_ℓ) are completely determined as well. For the hadronic decay, the missing knowledge about the quark flavour at the origin of each jet leads to a *two-fold* ambiguity which corresponds to swapping the quark-jet assignment

$$\cos\theta_j \leftrightarrow -\cos\theta_j \ , \qquad \phi_j \leftrightarrow \phi_j + \pi \ . \tag{4.23}$$

In the purely hadronic decays, the flavour of the four quarks in the final state is a priori unknown. This entails ambiguities in the determination of both the two W decay angles sets and the charge of the Ws. As a result, an overall *eight-fold* ambiguity holds

$$\cos\Theta \leftrightarrow -\cos\Theta \ , \qquad \cos\theta_j \leftrightarrow -\cos\theta_j \ , \qquad \phi_j \leftrightarrow \phi_j + \pi \ . \tag{4.24}$$

On the top of that, an additional uncertainty appears in this decay channel when trying to assigning jet pairs to Ws, which can be done in three different ways if no extra information is available.

The existence of these ambiguities needs to be included in the fit in order not to bias the result. In a log-likelihood fit, for instance, the original p.d.f. $\mathcal{P}$ in (4.2) must be

replaced by

$$\mathcal{P}'(\vec{\Omega}|\vec{g}) = \sum_{p=1}^{N_{perm}} \mathcal{P}(\vec{\Omega}|\vec{g})\,\omega_p \;, \tag{4.25}$$

where all the N_{perm} possible permutations of the final state fermions are considered, each one with a certain weight ω_p. This weight depends on the extra information added to distinguish among the different permutations as described in Sect. 5.2.5. If no extra information is provided, every permutation must be equally weighted, hence $\omega_p = 1/N_{perm}$.

If optimal observables are used in the fit instead, the definition of the observables has to be modified such that the existing ambiguities are considered. The first order optimal observable (4.7), for instance, must be replaced by

$$\mathcal{O}'_{1,i} \;\equiv\; \frac{S'_{1,i}(\vec{\Omega})}{S'_0(\vec{\Omega})} \;, \tag{4.26}$$

where

$$S'_{\substack{0\\1,i}}(\vec{\Omega}) = \sum_{p=1}^{N_{perm}} S_{\substack{0\\1,i}}(\vec{\Omega}_p)\,\omega_p \;, \tag{4.27}$$

The impact of these ambiguities in the TGC measurement has been studied using Monte Carlo events at the generator level. This will be useful to quantify the potential improvement that one might expect in the TGC measurement when including extra experimental information to disentangle such ambiguities (applying c-tagging and jet charge tagging algorithms, for instance).

Sets of 100000 Monte Carlo events have been generated where certain efficiencies to tag c quarks and to measure the charge of the W bosons have been artificially introduced. The TGCs have then been fitted from these event sets taking into account the c-tagging and W charge tagging efficiencies (ϵ_c and $\epsilon_{W_{ch}}$) simulated in the generation.

The results for semileptonic decays are shown in the left plots of Fig. 4.6. For these events, the only possible improvement can come from c-tagging. The ratio of the error in the TGCs for a given ϵ_c with respect to the *ideal* one obtained when perfect quark flavour tagging is assumed, is plotted versus the considered ϵ_c. First of all, the scale of the error degradation with respect to the ideal case when no quark flavour tagging is performed should be pointed out. It is found to be of the order of 30% to 50%, depending on the coupling. Secondly, it should be noticed that the potential improvement attainable by performing c-tagging amounts to 6% to 10% for $\epsilon_c = 1$.

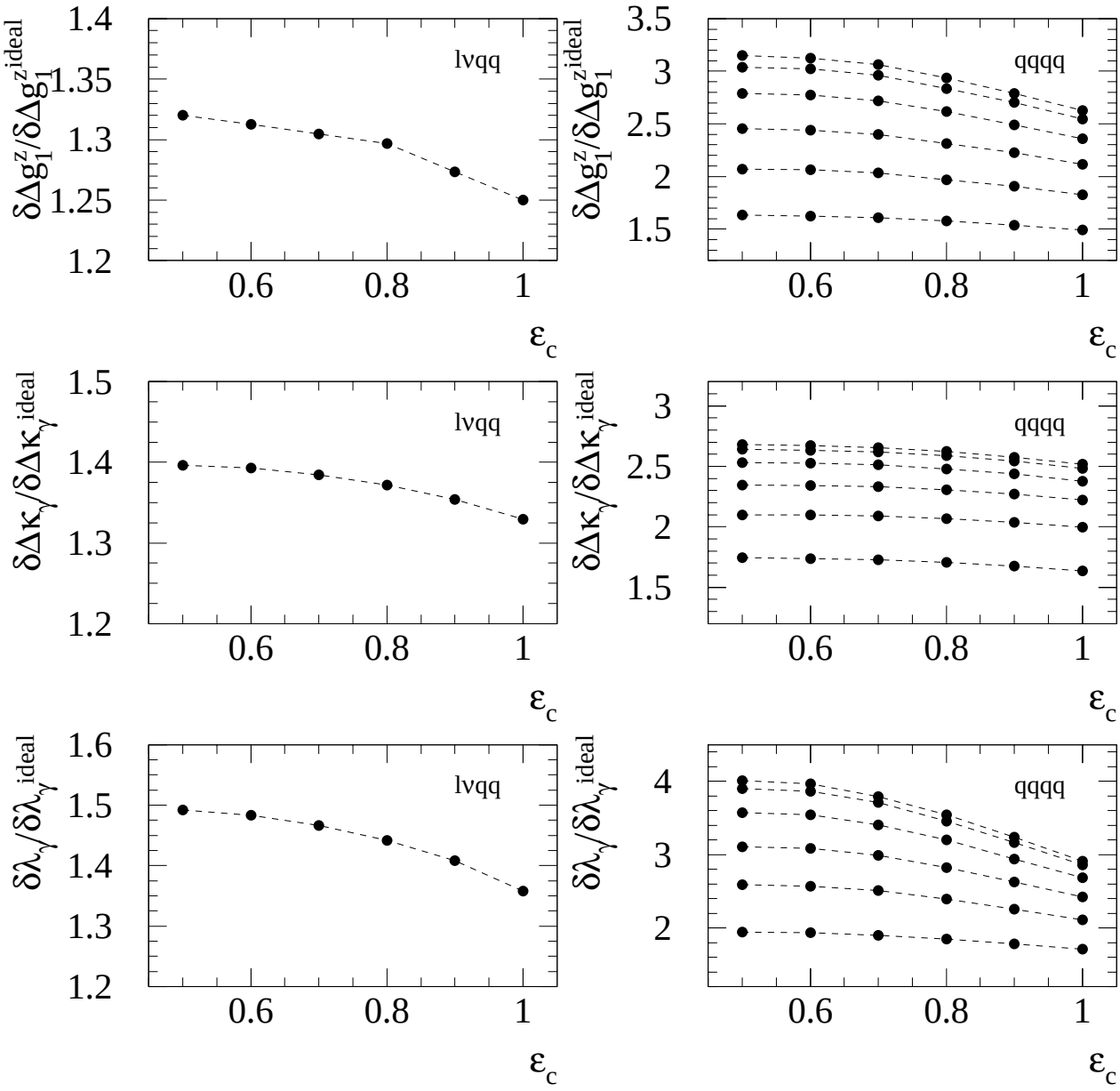

Figure 4.6: Impact of c-tagging and W charge tagging in the TGC measurement. For the purely hadronic channel plots (in the right), the W charge tagging efficiency has been increased from top to bottom: $\epsilon_{W_{ch}} = 0.5, 0.6, 0.7, 0.8, 0.9$ and 1.

The results for purely hadronic decays are shown in the right side plots of Fig. 4.6. For every TGC, the superimposed curves in the plot correspond to different values of $\epsilon_{W_{ch}}$: from 0.5 up to 1 in steps of 0.1. The error on the TGCs gets now worse by a factor ~ 3 to 4 (as compared again to the ideal case) when considering the eight possible permutations of the final state without performing any W charge or c-tagging. As seen from the plots, a big improvement can be achieved by tagging the charge of the W boson, since these numbers might be reduced by a factor ~ 2 if $\epsilon_{W_{ch}} = 1$. The improvement due to c-tagging appears to be marginal for the purely hadronic decays, specially for high values of $\epsilon_{W_{ch}}$.

From this Monte Carlo study, it can be concluded that the improvement in the TGC errors by performing c-tagging is going to be marginal (for realistic values of ϵ_c) for both the semileptonic and purely hadronic channels. However, for the latter, the W charge tagging represents a powerful tool to increase the sensitivity to the TGCs.

Jet Pairing

As already mentioned, the purely hadronic channel faces an additional experimental difficulty. For these events, the first thing one should do (before trying to tag the charge of the Ws and their decays) is to assign jet pairs to Ws, procedure referred to as *jet pairing* throughout this thesis.

A set of samples of 100000 Monte Carlo WW events have been generated, where different probabilities of missassigning jet pairs to Ws have been artificially introduced. The impact of this jet pairing inefficiency is studied by fitting the TGCs from these samples. No c-tagging and W charge tagging ($\epsilon_c = \epsilon_{W_{ch}} = 0.5$) are assumed in these experiments. The optimal observable definitions in (4.26) and (4.27) have to be now extended to include those permutations of the final state four-momenta associated to different jet pairings. Therefore, for a given jet pairing efficiency ϵ_{JP},

$$S'_{\substack{0\\1,i}}(\vec{\Omega}) = \frac{\epsilon_{JP}}{8} \sum_{right} S_{\substack{0\\1,i}}(\vec{\Omega}_p) + \frac{1-\epsilon_{JP}}{16} \sum_{wrong} S_{\substack{0\\1,i}}(\vec{\Omega}_p)\,, \tag{4.28}$$

where p runs over those permutations associated to a correct jet pairing in the first sum and to a wrong one in the second.

The ratio of the obtained errors when considering all the possible permutations with respect to the ideal ones are plotted in Fig. 4.7 as function of the assumed jet pairing efficiency. The flat dependence observed with respect to ϵ_{JP} shows that the eventual improvement in the TGC error when going from $\epsilon_{JP} = 1/3$ (no jet pairing) to a typical 80%

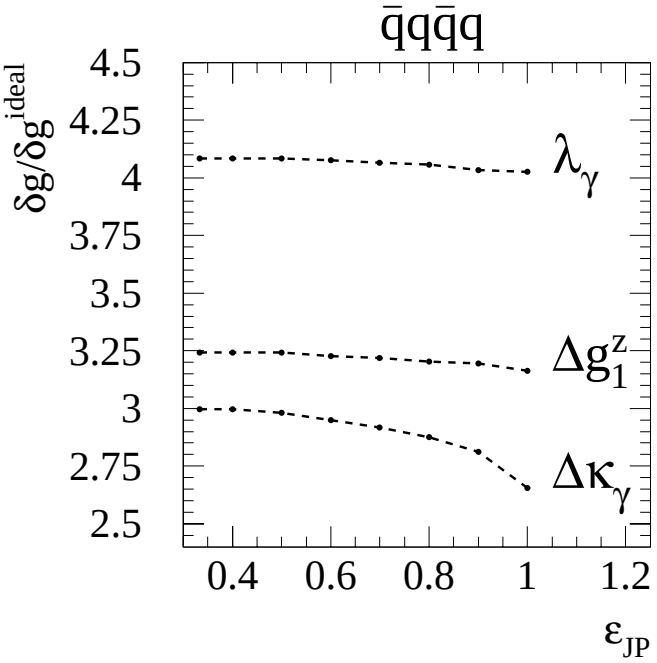

Figure 4.7: Impact of jet pairing algorithm on the TGC measurement in the purely hadronic channel. No c-tagging and W charge tagging have been assumed ($\epsilon_c = \epsilon_{W_{ch}} = 0.5$).

efficient jet pairing algorithm is very small, provided that all the possible permutations of the final state four-momenta are included in the observable definitions. For this reason, in this work no jet pairing algorithm has been used for the purely hadronic analysis.

4.2 Total cross section

The total W pair cross section obtained after integrating (4.6) over the phase space $\vec{\Omega}$, can be parameterised also as a second order polynomial in the TGCs

$$\sigma(\vec{g}) = \sigma_0 + \sum_i \sigma_{1,i}\, g_i + \sum_{ij} \sigma_{2,ij}\, g_i\, g_j \ . \tag{4.29}$$

This dependence, shown in Fig. 4.8, allows to set limits on the TGCs through a WW cross section measurement. To do so, a piece is added to the χ^2 (4.17) to account for the total cross section information

$$\chi^2(\vec{g}) = \sum_{ij} (\langle \mathcal{O}_i \rangle - E[\mathcal{O}_i])\ NV(\mathcal{O})^{-1}{}_{ij}\ (\langle \mathcal{O}_j \rangle - E[\mathcal{O}_j]) + \frac{N_{obs} - N_{exp}(\vec{g})}{\delta N_{exp}} \ . \tag{4.30}$$

The expected number of events N_{exp} for a given luminosity $\mathcal{L}_d$ has also a second order

polynomial dependence on the TGCs and it is obtained from the Monte Carlo samples as

$$N_{exp}(\vec{g}) = \left(\frac{N_{sel}^{4f}(\vec{g})}{N_{tot}^{4f}(\vec{g}=\vec{0})} \cdot \sigma_{4f}^{MC} \cdot + \sum_b \sigma_b \epsilon_b \right) \mathcal{L}_d \ , \tag{4.31}$$

where $\mathcal{L}_d$ stands for the integrated luminosity in the data sample. The sum in the second

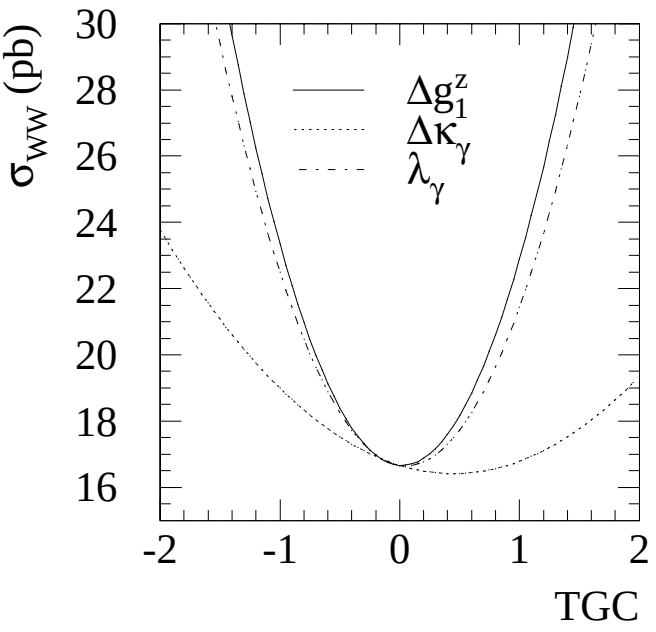

Figure 4.8: The dependence of the WW cross section on the TGCs.

term runs over the different backgrounds considered, σ_b and ϵ_b being their cross sections and efficiencies, respectively. The first term in Eq. (4.31) accounts for the expected number of four-fermion events and is computed using a sample of N_{tot}^{4f} Monte Carlo events generated at SM couplings using `KORALW-4f`, corresponding to a total cross section σ_{4f}^{MC}. The coupling-dependent term $N_{sel}^{4f}(\vec{g})$ is computed as the sum of the weights of those four-fermion events accepted by the selection

$$N_{sel}^{4f}(\vec{g}) = \sum_{sel} \omega(\vec{\Omega}; \vec{g}) \ , \tag{4.32}$$

where each event weight ω is given by Eq. (4.19).

Chapter 5

Experimental procedure

The semileptonic W pair decay channel is generally considered to be the most powerful one for the TGC extraction [26]. A part from being the second statistically dominant one ($BR_{\ell\nu q\bar{q}} \sim 29\%$), it allows to determine the charge of the Ws by tagging the lepton charge, and offers at the same time a good knowledge of the Ws direction thanks to the hadronic W decay. The situation is pretty different for the purely hadronic decay channel, where one is forced to pair the four jets into two Ws and tag the jet charges before recovering the WW event information. However, its large branching ratio ($BR_{q\bar{q}q\bar{q}} \sim 46\%$) together with the fact that it shares with the semileptonic channel some common features in the reconstruction and mainly suffers from the same background processes, justify the decision to include it in this analysis as well.

At a centre of mass energy of $\sqrt{s} = 189$ GeV, the cross section for the semileptonic and the purely hadronic W pair decay channels, is of the order of 4.8 and 7.6 pb, respectively. This is between ten and twenty times smaller than that for one of the main background processes: $e^+e^- \to \mathrm{Z}^0/\gamma \to q\bar{q}(\gamma)$. For this reason, highly discriminating selections are needed to obtain a pure sample of WW events while keeping the efficiency high.

The first section of this chapter is devoted to briefly describe the Monte Carlo samples of both signal and background used in the analysis. The selections for the two studied topologies are presented in the second section, where some of the reconstruction procedures are also described. Once the event selection and reconstruction are determined for each decay channel, fully reconstructed Monte Carlo events are used to test the fitting technique which is going to be used in the TGC extraction. The description of these tests is presented at the end of this chapter. The last section of this chapter is devoted to

describe these tests.

5.1 Event simulation

In order to evaluate background contaminations and efficiencies or, in general, compare the theoretical predictions to the experimental data, Monte Carlo simulated events are generated for every physics process relevant for this analysis.

To simulate the signal events, i.e. four-fermion final states which can come from WW production and decay, the `KORALW` generator, version 1.21 [31], is used. This program includes multi-photon initial state radiation with finite photon transverse momentum via Yennie-Frautschi-Suura exponentiation [32], final state radiation via `PHOTOS` [34] and Coulomb correction [11]. The `JETSET` [35] package takes care of gluon radiation and hadronisation. No colour reconnection effects are included. It can generate CC03 diagrams only or include four-fermion diagrams leading to WW-like final states which are computed with the `GRACE` package [33], with fixed W and Z widths. In this last case, loose cuts at the generator level are applied on the outgoing electron angle or the fermion-antifermion pair invariant masses to avoid phase space regions with poles in the cross section. The events generated in these regions would be in any case rejected by the selection.

Monte Carlo samples corresponding to integrated luminosities at least twenty times as large as that of the data are generated and fully simulated for all relevant background processes. Anihilation into quark pairs, $e^+e^- \to \mathrm{Z}^0/\gamma \to q\bar{q}(\gamma)$, is simulated with `PYTHIA` [35]. Tagged two photon processes into leptons and hadrons are generated with `PHOTO2` [36]. Dilepton final states are generated with `KORALZ` [37] and `BHWIDE` [38]. Finally, `PYTHIA` is also used for various processes leading to four-fermion final states such as $e^+e^- \to \mathrm{Z}^0\mathrm{Z}^0$, $e^+e^- \to \mathrm{Z}^0e^+e^-$ and $e^+e^- \to \mathrm{W}e\nu_e$. To avoid double counting of four-fermion events between the signal and background Monte Carlos, events with a flavour content that could originate from W pair production are explicitly removed from the background samples when needed. The cross sections and number of events generated for all these processes are listed in Table 5.1.

Process	Cross section (pb)	Number of events
$e^+e^- \to f_1\bar{f}_2\ f_3\bar{f}_4$ (WW-like)		
SM TGCs	16.92	500000
$e^+e^- \to W^-W^+$ (CC03)		
SM TGCs	16.56	450000
$\Delta g_1^Z = -0.5,\ \Delta\kappa_\gamma = \lambda_\gamma = 0$	18.26	50000
$\Delta g_1^Z = 0.5,\ \Delta\kappa_\gamma = \lambda_\gamma = 0$	18.04	50000
$\Delta\kappa_\gamma = -0.5,\ \Delta g_1^Z = \lambda_\gamma = 0$	17.44	50000
$\Delta\kappa_\gamma = 0.5,\ \Delta g_1^Z = \lambda_\gamma = 0$	16.34	50000
$\lambda_\gamma = -0.5,\ \Delta g_1^Z = \Delta\kappa_\gamma = 0$	18.16	50000
$\lambda_\gamma = 0.5,\ \Delta g_1^Z = \Delta\kappa_\gamma = 0$	17.64	50000
$\Delta\kappa_\gamma = \Delta g_1^Z = 0.5,\ \lambda_\gamma = 0$	17.35	50000
$\Delta\kappa_\gamma = 0.5,\ \lambda_\gamma = -0.5,\ \Delta g_1^Z = 0$	17.83	50000
$e^+e^- \to \mathrm{Z}^0/\gamma \to q\bar{q}(\gamma)$	99.4	495000
$e^+e^- \to \mathrm{Z}^0/\gamma \to \tau^+\tau^-(\gamma)$	8.21	150000
$e^+e^- \to \mathrm{Z}^0 e^+e^-$	965.7	3000000
$e^+e^- \to \mathrm{Z}^0\mathrm{Z}^0$	2.8	100000
$e^+e^- \to \mathrm{Z}^0 e^+e^-$	6.8	100000
$e^+e^- \to \mathrm{W}e\nu_e$	0.66	15000
$\gamma\gamma \to e^+e^-$	3800	3500000
$\gamma\gamma \to \mu^+\mu^-$	3550	3200000
$\gamma\gamma \to \tau^+\tau^-$	427	500000
$\gamma\gamma \to u\bar{u}, d\bar{d}$	487	400000
$\gamma\gamma \to c\bar{c}$	93	200000
$\gamma\gamma \to s\bar{s}$	24	40000
$\gamma\gamma \to b\bar{b}$	0.63	12000

Table 5.1: Cross sections and number of events for the signal and background Monte Carlo samples used.

5.2 Event selection and reconstruction

5.2.1 Semileptonic event selection

The semileptonic W pair decays are characterised by a high energy and isolated lepton, a hadronic system which can be associated to two or more jets and a large amount of

missing momentum due to the neutrino. The selection of such events proceeds in several steps which are described in this section.

Preselection

Because of the large amount of background as compared to the signal, a soft preselection is needed which rejects as much background as possible while keeping the signal essentially untouched. First of all, the events are required to have at least nine *good charged tracks*, which are those satisfying the following requirements:

- It should have at least four three-dimensional hits in the TPC.
- It should originate from a cylinder centered around the fitted average interaction point, with a radius of 2 cm and a length of 10 cm.
- The polar angle of the track should satisfy $|\cos\theta| < 0.95$

In addition, the total energy of all good charged tracks in the event is required to exceed 10% of the centre of mass energy.

The kinematics of radiative return events can be used to design a cut on the longitudinal missing momentum which scales automatically with the centre of mass energy. From a Monte Carlo study [39], the optimal cut to reject such kind of events is found to be[1]

$$\not{p}_L < Max \left(\begin{array}{c} \sqrt{s}(1-\frac{m_Z^2}{s}) - \sqrt{|\not{E}^2 - \not{p}_T^2|} - 6 \\ \frac{\sqrt{s}}{2}(1-\frac{m_Z^2}{s}) - 27.5 \end{array} \right) . \tag{5.1}$$

In order to eliminate the background coming from non-radiative events and, in general, events that are completely contained within the detector, the following cuts are added:

$$\not{E} > 0, \qquad \not{p} > 0, \qquad \not{p}_T > 20, \qquad \not{p} > 35 - \not{E} . \tag{5.2}$$

Finding a lepton candidate

The high energy lepton expected in a semileptonic W pair decay is found among the event good charged tracks by applying a kinematic algorithm. It is chosen to be the good charged track with the largest value of $p \cdot \sin\alpha/2$, where p is the momentum of the track,

[1] $\not{E}$ is expressed in GeV and $\not{p}$ in GeV/c units in all the preselection cuts described in this page.

and α is the angle between the track and the nearest jet clustered from the remaining good charged tracks in the event using the DURHAM [40] algorithm in the P recombination scheme [41] with $y_{cut} = 0.0003$. Using Monte Carlo WW events it has been determined that the correct lepton is found by this algorithm in 93% of the $e\nu q\bar{q}$ events and 97% of the $\mu\nu q\bar{q}$ events.

Lepton identification

Once a lepton candidate has been found, loose lepton identification criteria are applied to this track in order to separate the $e\nu q\bar{q}$ and $\mu\nu q\bar{q}$ channels.

The muon identification is based on the combined analysis of the response of the HCAL detector and the muon chambers, which is performed by the QMUIDO [23] routine. The track is identified as a muon if the identification flag is positive. In addition, those tracks pointing to an HCAL crack which failed the QMUIDO flag requirement can still be identified as a muon provided that they fulfill the following requirements:

ECAL energy associated to this track < 1 GeV
Fraction of the track energy deposited in ECAL $< 10\%$
HCAL energy associated to this track < 5 GeV
Fraction of the track energy deposited in HCAL $< 10\%$

The electron identification criteria is based on the R_T, R_L and R_I estimators described in Sect. 3.3.2. The shape of these variables for $e\nu q\bar{q}$ and $\mu\nu q\bar{q}$ WW decays is shown in Fig. 5.1. Whenever the ionisation estimator R_I is used, and to ensure a reliable dE/dx measurement, tracks are required to have at least 50 isolated wire hits.

The allowed values for these estimators depend on the ECAL region where the track is pointing to:

not in a crack region $R_I > -2.5$, $R_L > -2.5$ and $R_T > -8$,
in a crack region $R_I > -2.5$ and $N_{fired} < 10$,

where N_{fired} stands for the number of HCAL planes associated to the electron track which fired (see Sect. 3.3.2). The idea is to try to recover those tracks pointing to an ECAL crack , which can not then be recognised by the ECAL cluster-shape variables, by looking at the HCAL digital pattern behind the ECAL crack and requiring a compact electron shower in HCAL.

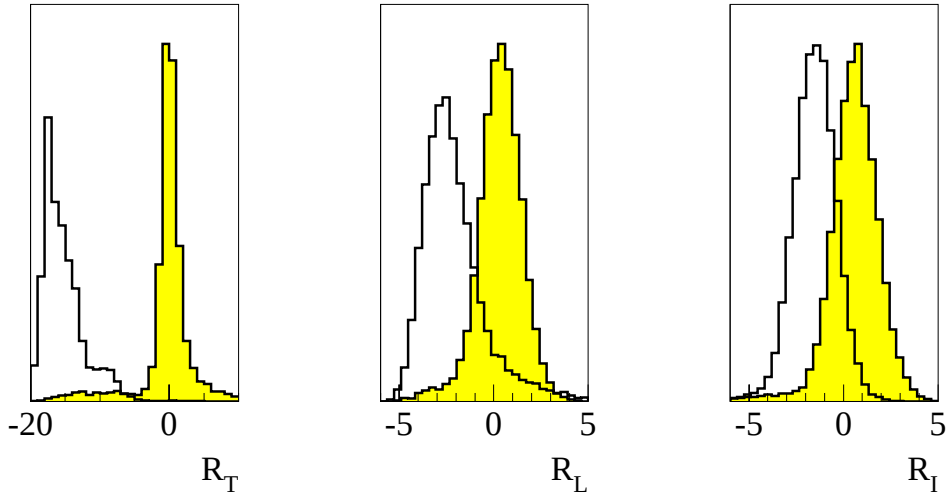

Figure 5.1: Electron identification estimators R_T, R_L and R_I for $e\nu q\bar{q}$ (shaded) and $\mu\nu q\bar{q}$ (open) Monte Carlo WW events.

The identification efficiency for both electrons and muons from semileptonic W pair decays which are correctly selected among the charged tracks in the event is around 99%. About 2% of the selected leptons satisfy both the electron and the muon identification criteria, due to the loose electron identification. In this case, the track is taken to be a muon as the probability for a real electron penetrating the HCAL is very small.

Bremsstrahlung correction

In about 40% of the $e\nu q\bar{q}$ events the electron radiates a Bremsstrahlung photon with an energy greater than 0.5 GeV. The Bremsstrahlung photons are radiated when the electron interacts with material in the detector. Most of these photons are produced in the VDET/ITC and ITC/TPC boundaries, where a higher concentration of material is found. As a consequence of this radiation, a low energy tail appears in the electron energy spectrum and its energy resolution is degraded.

It is important to recover this radiation, as the corrected full energy of the electron can be a better variable to discriminate the high energy $e\nu q\bar{q}$ signal from the background. To do so, the energy of all those ECAL clusters found within a cone of 2.5° around the electron track are summed together to make the total electromagnetic energy of the electron. To get an estimate of the original total electron energy, the tracking energy and the electromagnetic energy are then combined with weights which take into account the resolutions of the tracking and calorimetric detectors involved (this procedure is described

in detail in [42]).

In order to reduce the amount of energy added to the electron candidate track in background events, the Bremsstrahlung correction is applied only if the charged energy within a cone of 6° around the electron track is smaller than 5 GeV.

Once the electron candidate energy has been corrected, its momentum is recomputed such that the pion mass hypothesis (see Sect. 3.3.3) still holds. The direction of the original track is therefore not modified by the Bremsstrahlung correction. As most of the Bremsstrahlung radiation occurs after the electron has passed the VDET, the VDET coordinates are on the original trajectory of the electron. Due to the weight of the high precision coordinates from the VDET in the track helix fit, the best estimate for the original direction of the electron is that given by the tracking.

Final state radiation correction

The Final State Radiation (FSR) photons may be radiated at large angles with respect to the lepton, so most of them will not be recovered by the Bremsstrahlung correction but included inside some of the two jets. The misassignement of FSR photons can bias both the jets and lepton directions therefore affecting the TGC measurement.

In order to look for FSR photons in the detector, the `GAMPEX` [43] program is used. The closest `GAMPEX` photon to the lepton with an energy greater than 0.5 GeV is considered as an FSR candidate provided it is not consistent with a $\pi^0 \to \gamma\gamma$ hypothesis from `QPIODO` [44] and is not associated to any object found by the Bremsstrahlung correction.

The photon is then required to be more than 40° away from the nearest good charged track which is not the lepton and to be closer to the lepton than to any other charged track, to avoid picking up photons from the jets. Finally, and to prevent selecting ISR photons, the photon is demanded to be closer to the lepton than to the beam axis.

Then the four-vectors for the FSR candidate and the tracking estimate of the lepton are added, and the energy of the final object is recomputed such that the pion mass hypothesis still holds. This is different when compared to the Bremsstrahlung case, as the tracking measurement of the lepton direction is not anymore its best estimate. The reason is that FSR photons can be thought as being radiated at the interaction point and might therefore subtend a large angle with respect to the lepton.

The photon identification efficiency of the `GAMPEX` algorithm drops in the vicinity of

charged tracks. This is not an issue for the electron tracks, since the Bremsstrahlung correction picks up the photons close to the track. In order to improve the muon energy resolution, where no Bremsstrahlung correction is performed, any energy deposit over 2 GeV which lies inside the Bremsstrahlung region, is added to the muon energy.

Jets clustering

Once the lepton has been identified and its four-momenta corrected, the remaining objects in the event need to be clustered into two jets. Before doing that, the following objects are locked:

- The lepton track.
- All calorimetric deposits associated to the lepton by the Bremsstrahlung or FSR corrections.
- All ECAL (HCAL) deposits within 1.5° (2°) of the lepton track, provided that the lepton track has been found to be isolated.

Then, all the remaining energy flow objects are clustered into two jets by using the `DURHAM` algorithm in the `PE` recombination scheme, in which the `P` sheme is used to decide which particles are assigned to which jet, but the four momentum is computed by using the `E` scheme [41].

Multi-variable discrimination

The following set of three variables has been found to have a good discriminating power between signal and background, as shown in Fig. 5.2:

- Lepton momentum p_ℓ.
- Transverse missing momentum $\not{p}_T$.
- Lepton isolation I_ℓ, defined in terms of the angle between the lepton and both the nearest good charged track and the nearest of the two jets as

$$I_\ell \equiv \log(\tan\frac{\theta_{j\ell}}{2}) + \log(\tan\frac{\theta_{c\ell}}{2}) \; . \tag{5.3}$$

The a-posteriori probability that a generic data event point $\{\vec{\phi}\} \equiv \{p_\ell, \not{p}_T, I_\ell\}$ has originated from the signal WW process $\mathcal{P}(\ell\nu q\bar{q}|\{\vec{\phi}\})$ is an optimal variable to separate

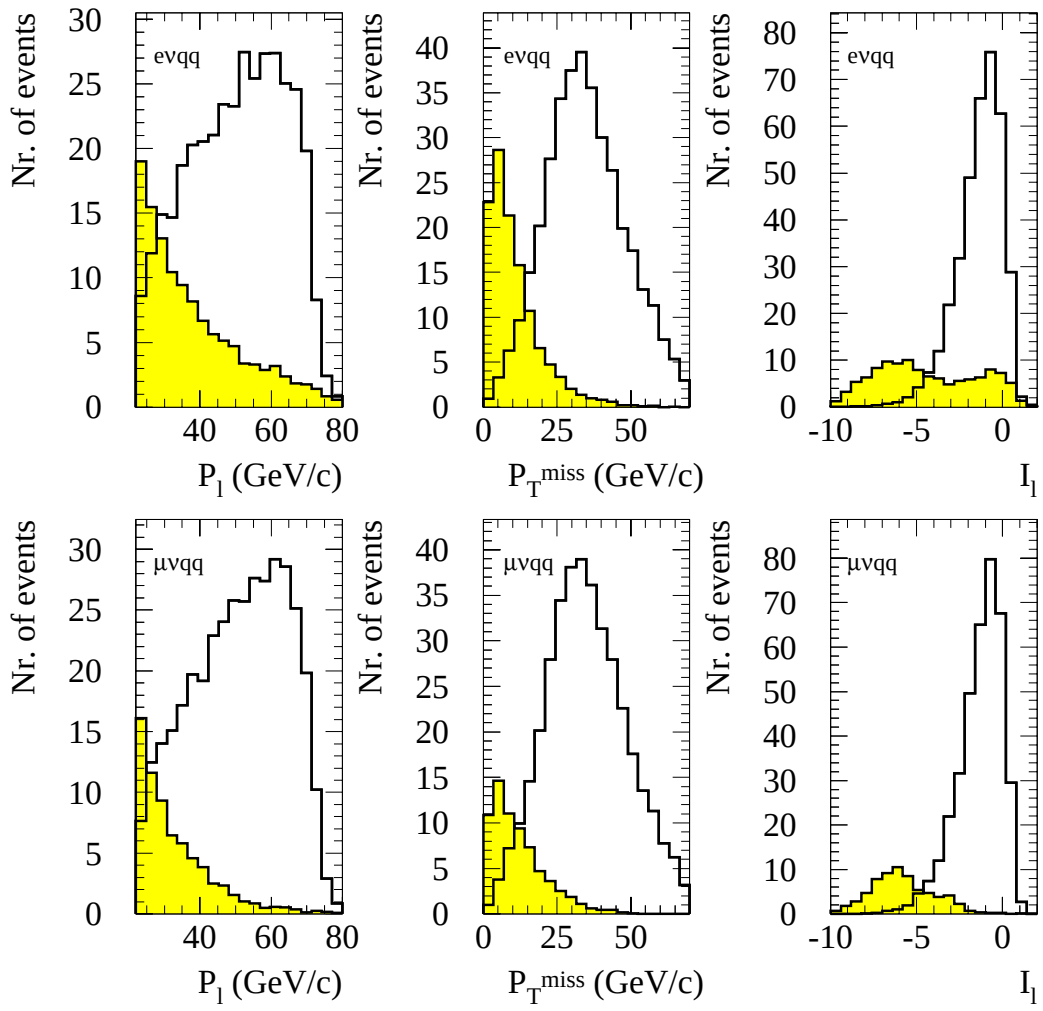

Figure 5.2: Discriminating variables used in the semileptonic selection. The open histograms correspond to the signal while the shaded ones are built by adding up the different background contributions. The histograms are normalised so that they correspond to the same luminosity as in the data sample.

preselected signal events from background ones, which takes into account the discriminating power and correlations among the three observables.

Monte Carlo distributions of preselected events can be used to estimate the three-dimensional a-priori probability density functions $\mathcal{P}(\{\vec{\phi}\}|\ell\nu q\bar{q})$ and $\mathcal{P}(\{\vec{\phi}\}|bckg)$, which can then be combined to get $\mathcal{P}(\ell\nu q\bar{q}|\{\vec{\phi}\})$ by using the Bayes Theorem [45].

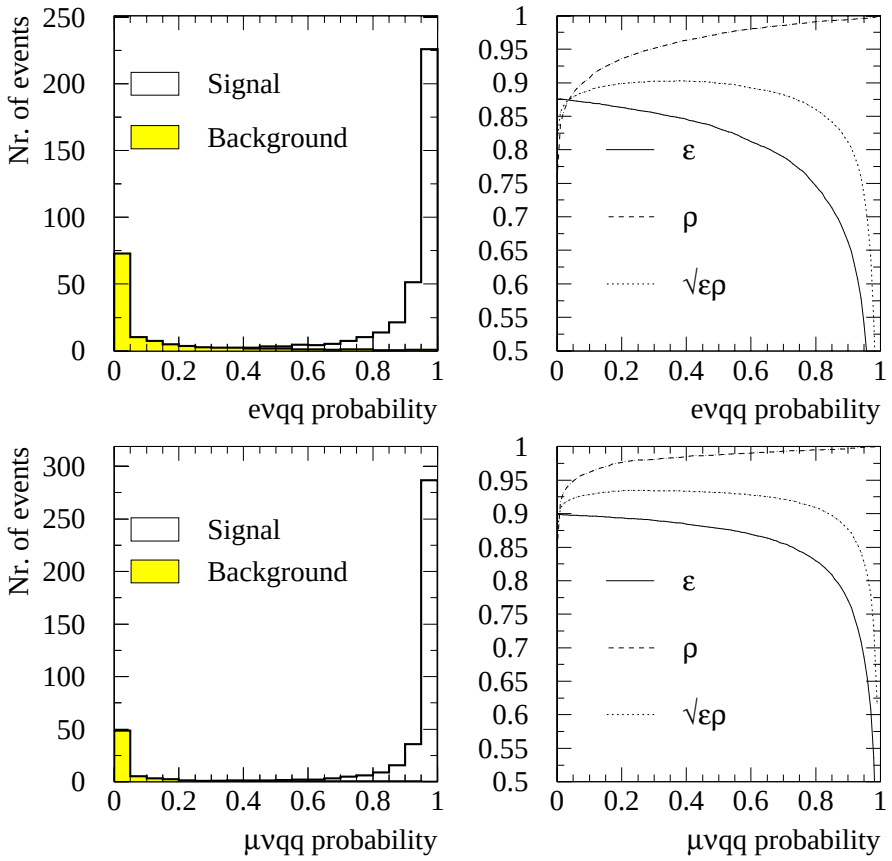

Figure 5.3: Left: performance of the $e\nu q\bar{q}$ and $\mu\nu q\bar{q}$ probabilities to separate signal and background. Right: Evolution of the efficiency ϵ and purity ρ of the selections with the lower bound in the probability.

The a-posteriori probabilities are shown in Fig. 5.3 for the $e\nu q\bar{q}$ and $\mu\nu q\bar{q}$ channels as well as the variation of the efficiency ϵ and purity ρ as the lower bound on this discriminating variable is moved. The lower bounds are chosen such that the product $\epsilon\rho$ is maximised, hence minimising the statistical error of the cross section. The obtained values are:

$$\mathcal{P}(e\nu q\bar{q}|\{\vec{\phi}\}) > 0.4\,, \qquad \mathcal{P}(\mu\nu q\bar{q}|\{\vec{\phi}\}) > 0.4\,. \tag{5.4}$$

The selection efficiencies for the different processes after these cuts are summarised in Table 5.2.

	Efficiency (%)		
Process	$e\nu q\bar{q}$ selection	$\mu\nu q\bar{q}$ selection	$q\bar{q}q\bar{q}$ selection
WW signal	82.9	87.2	88.3
WW background	0.6	0.7	0.3
$e^+e^- \to \mathrm{Z}^0/\gamma \to q\bar{q}(\gamma)$	0.03	0.03	1.32
$e^+e^- \to \mathrm{Z}^0\mathrm{Z}^0$	0.35	0.54	7.03
$e^+e^- \to \mathrm{Z}^0 e^+e^-$	0.59	0.00	0.05
$e^+e^- \to \mathrm{Z}^0/\gamma \to \tau^+\tau^-(\gamma)$	0.01	0.00	0.00
$e^+e^- \to \mathrm{W}e\nu_e$	2.0	0.09	0.00
$\gamma\gamma \to c\bar{c}$	0.01	0.00	0.00
$\gamma\gamma \to b\bar{b}$	0.07	0.00	0.00
Purity (%)	90.8	93.6	81.5

Table 5.2: Semileptonic and purely hadronic selection efficiencies for different processes.

5.2.2 Purely hadronic selection

At the centre of mass energy considered in this analysis, the main background of the process $e^+e^- \to W^+W^- \to q\bar{q}q\bar{q}$ is the $e^+e^- \to \mathrm{Z}^0/\gamma \to q\bar{q}(\gamma)$ production, followed by the $e^+e^- \to \mathrm{Z}^0\mathrm{Z}^0$ and $e^+e^- \to W^+W^- \to \ell\nu q\bar{q}$ processes. The selection of purely hadronic W pair decays proceeds mainly in two steps. A soft preselection is first applied, whose aim is to increase the purity before the multivariate analysis, which comes in the second stage.

Preselection

In the first step of the preselection, the events are required to have at least five good charged tracks and total energy of all good charged tracks exceeding 10% of the centre of mass energy. The following cuts are then applied:

- $|p_L| < 0.95(m_{vis} - m_Z)$, in order to reduce the radiative return background.
- Sphericity > 0.03, since the global shape of purely hadronic WW decays is more spherical than that of $q\bar{q}$ events (a definition of sphericity can be found in [46]).
- $y_{34} > 0.001$, y_{34} being the y_{cut} value for which the `DURHAM` jet clustering algorithm transforms the four jets into three.

After this, the event is forced to four jets by using the DURHAM algorithm in the PE recombination scheme. In order to eliminate events with an ISR photon emitted within the detector acceptance, it is also required that none of the four jets contains more than 95% electromagnetic energy.

Multi-variable discrimination

A feed-forward Neural Network (NN), trained to optimise the discrimination between signal and background using dedicated Monte Carlo event samples, is then used to project the information of 19 discriminating variables into one: the NN output. The selection is then performed by making a cut on this NN output. The 19 variables used as input for the NN are listed in Table 5.3. A more detailed description of the NN architecture and these variables can be found elsewhere [47].

Global topological variables	Fox Wolfram Moments: H_0, H_2 and H_4
	Sphericity
	Missing energy
WW kinematics	Sum of cosine of angles between jets
	Energy of most energetic jet (1st jet)
	Momentum of less energetic jet (4th jet)
	Cosine of angle between 2nd and 3rd jets
	Asymmetry between 2nd and 3rd jets
	Energy of 2nd jet
Jet properties	Number of good tracks of 1st jet
	Sum of angles between the leading and tracks of 1st jet
	Sum of angles between the leading and tracks of 2nd jet
	Maximum energy carried by one object of 1st jet
	Maximum energy carried by one object of 2nd jet
	Maximum energy carried by one object of 3rd jet
	$\sum p_T^2$ for 2nd jet
Flavour tagging	b-tag event probability

Table 5.3: Set of input variables for the NN used in the purely hadronic WW decays selection.

The performance of the NN is illustrated in Fig. 5.4, where the NN output distribution is shown for both signal and background as well as the efficiency ϵ and purity ρ versus NN output cut.

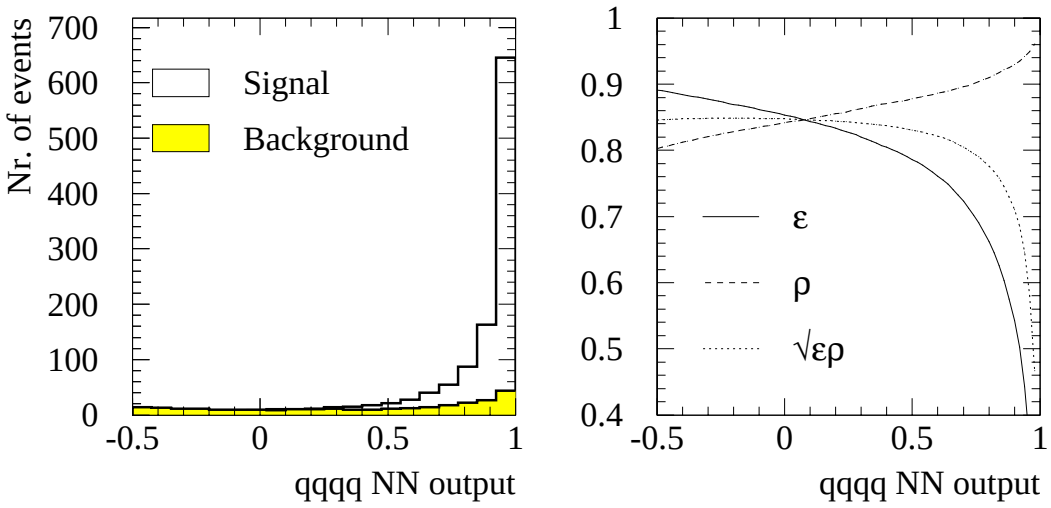

Figure 5.4: Performance of the $q\bar{q}q\bar{q}$ selection NN. Left: NN output for signal events (open histogram) and QCD background (shaded histogram). Right: Evolution of the efficiency ϵ and purity ρ of the selection with the lower bound in the NN output.

The NN lower bound is finally fixed to be 0, which is in a flat $\epsilon\rho$ region where this product is maximal. The selection efficiencies for the different processes after this cut are summarised in Table 5.2.

5.2.3 Kinematic fit

In order to improve the resolution of the measured final state four-momenta, a kinematic fit is applied to the final state by using the `ABCFIT` [48] package. The four measured momenta $\vec{p}_i^{\,meas}$ are modified within the kinematic fit by scaling them and introducing shifts in θ and ϕ to produce the corrected momenta

$$\vec{p}_i^{\,corr} = a_i \vec{p}_i^{\,meas} + b_i \vec{u}_i^{\,\theta} + c_i \vec{u}_i^{\,\phi} \,, \tag{5.5}$$

where u_i^{θ} is a unitary vector which is in the plane defined by the z axis and the jet axis and is perpendicular to the latter, while u_i^{ϕ} is perpendicular to that plane. The parameters a_i, b_i and c_i have Gaussian distributions and depend on the jet energies and directions. These variables are used to build a χ^2 and constraints are imposed by Lagrange multipliers. The minimisation of this χ^2 is done via an iterative procedure.

The jets velocities are usually very well measured quantities, since systematic effects

due to particle misassignement or loss tend to cancel in the ratio $\frac{|\vec{p}|}{E}$. In the kinematic fit they are assumed to be perfectly measured, so the corrected energies are computed as

$$E_i^{corr} = E_i^{meas} \frac{|\vec{p}_i^{\,corr}|}{|\vec{p}_i^{\,meas}|} \; . \tag{5.6}$$

Assuming the velocities are fixed to their measured values, 12 parameters are needed to define a four particles final state. In the semileptonic channel 9 of these parameters are independently measured, namely the two jets and the lepton $\{a, b, c\}$ parameters (or three-momenta). In the purely hadronic channel the three-momenta of the four jets are determined, hence the 12 parameters are independently measured. Several possibilites exist then to constrain the kinematic fit. In this analysis we concentrate on two:

i) Energy and momentum conservation are imposed (4 constraints), hence the fit is performed in the remaining 8 parameter space.

ii) Equal masses for the two reconstructed W bosons are assummed on the top of energy and momentum conservation. The fit is hence performed in a 7 parameter space.

A short notation is often adopted for these constraint configurations, which is related to the number of degrees of freedom[2] of the resulting fits. Those fits where only energy and momentum conservation are imposed are referred to as 1C or 4C depending on whether they are applied to semileptonic or purely hadronic WW decays. If the equal W masses constraint is added, the corresponding fits are denoted as 2C and 5C, respectively.

A sample of Monte Carlo WW events passed through the full ALEPH detector simulation is used to compare the performance of the different kinematic fits. The resolution of the five angles defining the event kinematics (see Chapter 2) achieved in $e\nu q\bar{q}$ events for different constraint assumptions is compared in Fig. 5.5. The first thing one notices is that the improvement in the angular resolution thanks to the kinematic fit is marginal for all the angles but for the polar angle of the leptonic decay system. Secondly, when going from a 1C to a 2C fit the improvement in the angular resolution is very small for any of the five angles. However, by adding the equal W masses constraint, the χ^2_{min} coming out from the kinematic fit can be translated into a probability for a given event to be consistent with a WW event, hence becoming a helpful variable to separate signal and

[2]The number of degrees of freedom of a fit is computed as:
Nr. degrees of freedom = Nr. measured parameters − Nr. independent parameters fitted.

background. For this reason the 2C kinematic fit is finally chosen for the semileptonic event reconstruction and a cut $\mathcal{P}(\chi^2 > \chi^2_{min}) > 0.001$ is applied in order to improve the purity of the sample (see Table 5.4).

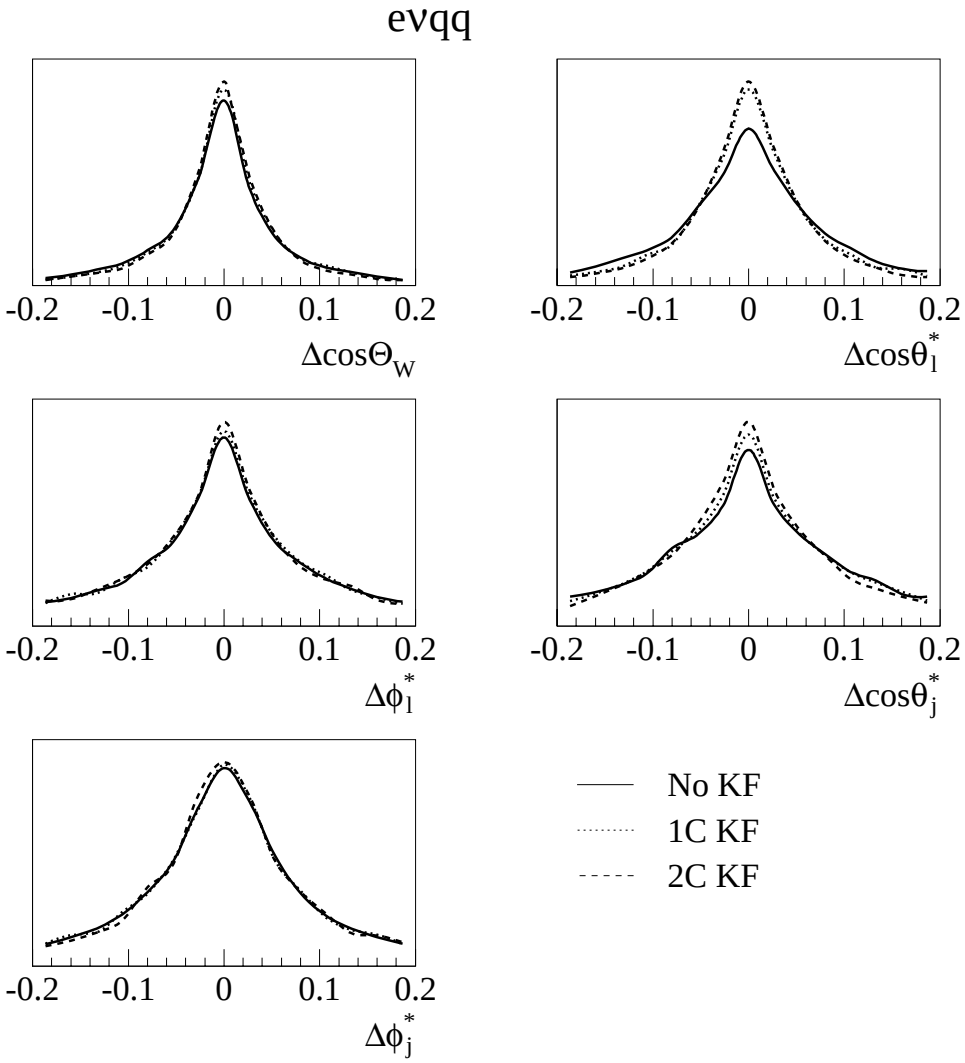

Figure 5.5: Angular resolution in $e\nu q\bar{q}$ events.

Figure 5.6 illustrates the effect of the kinematic fit on the angular resolution, when applied to purely hadronic events. It can be seen that the relative improvement on the angular resolution obtained when imposing energy and momentum conservation is, in general, larger than the one observed for semileptonic events. The cause for this is the

smaller number of degrees of freedom of the kinematic fit when it is applied to semileptonic events, arising from the use of momentum conservation to define the undetected neutrino. On the other hand, the initial resolution in the semileptonic channel is considerably better than that in the purely hadronic, where the higher multiplicity degrades the performance of the jet clustering algorithm.

As shown in Fig. 5.6, the additional constraint of equal W masses does not lead to an improvement in the angular resolution. For this reason a 4C kinematic fit is finally chosen for the purely hadronic decay channel reconstruction. It is worth to mention that, by not imposing the equal W masses constraint one avoids having to assumme any jet pairing.

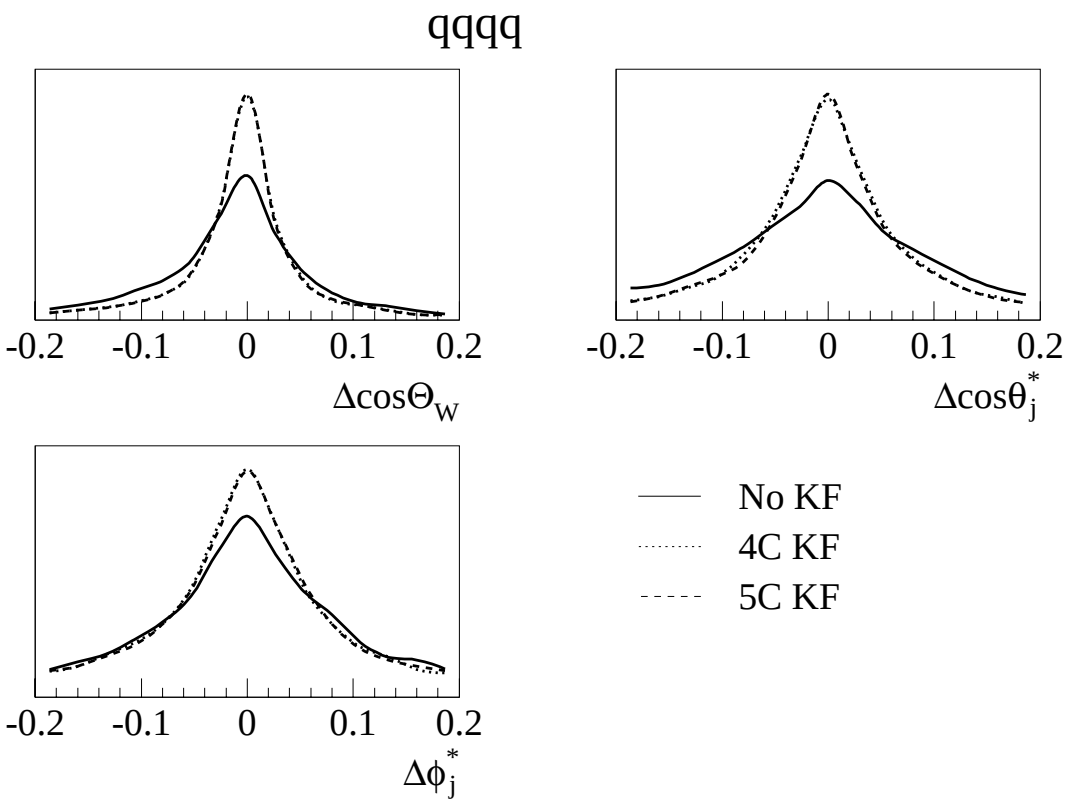

Figure 5.6: Angular resolution in $q\bar{q}q\bar{q}$ events.

5.2.4 Optimal observables window cut

The optimal observable distributions of the selected data for each of the three decay channels are shown in Figs. 5.7, 5.8 and 5.9 together with the Monte Carlo expectation for different coupling values.

Instabilities when measuring the observable mean values, which might be caused by few events falling in the tails of the distributions, are avoided by adding an extra *safety* cut in the selection: the events are required to be inside a window in the optimal observable space defined in such a way that it contains essentially 100% of the signal.

For the semileptonic events this window is defined as

$$\begin{array}{rrr} -4.0 < \mathcal{O}_{1,\Delta g_1^Z} < 5.0 & -4.0 < \mathcal{O}_{1,\Delta\kappa_\gamma} < 1.0 & -4.0 < \mathcal{O}_{1,\lambda_\gamma} < 5.0 \\ \mathcal{O}_{2,\Delta g_1^Z} < 8.0 & \mathcal{O}_{2,\Delta\kappa_\gamma} < 5.0 & \mathcal{O}_{2,\lambda_\gamma} < 8.0 \end{array}$$

while the condition imposed to the purely hadronic events is

$$\begin{array}{rrr} -1.0 < \mathcal{O}_{1,\Delta g_1^Z} < 0.5 & -0.6 < \mathcal{O}_{1,\Delta\kappa_\gamma} < 1.0 & -0.8 < \mathcal{O}_{1,\lambda_\gamma} < 0.4 \\ \mathcal{O}_{2,\Delta g_1^Z} < 4.0 & \mathcal{O}_{2,\Delta\kappa_\gamma} < 1.0 & \mathcal{O}_{2,\lambda_\gamma} < 2.0 \end{array}$$

The efficiencies and purities of the selections, taking into account these new cuts, are shown in Table 5.4 together with the number of events predicted by the Monte Carlo and those observed in the data.

		$e\nu q\bar{q}$ selection	$\mu\nu q\bar{q}$ selection	$q\bar{q}q\bar{q}$ selection
KF	Efficiency (%)	80.6	84.6	87.1
converged	Purity (%)	93.0	95.6	82.0
$\mathcal{P}(\chi^2 > \chi^2_{min})$	Efficiency (%)	78.7	82.8	87.1
cut	Purity (%)	94.9	97.3	82.0
	Efficiency (%)	78.5	82.7	83.0
$\mathcal{OO}$	Purity (%)	95.2	97.4	82.9
window	$N_{expected}$	351.0	358.3	1320.5
	$N_{observed}$	337	350	1240

Table 5.4: Semileptonic and purely hadronic selection efficiencies and purities.

For the three final states, the number of observed events in the data is found to be smaller than the one predicted by the Monte Carlo. The differences in the electron and muon semileptonic channels correspond to less than one standard deviation, therefore

compatible with being originated from a statistical fluctuation. However, in the purely hadronic channel a discrepancy of about 2.5 standard deviations is found. This discrepancy has been found in all the ALEPH analysis in which purely hadronic W pair decays are selected from the 189 GeV data sample [49, 57]. As described in [49], a large number of checks have been performed in order to guarantee that the origin of such discrepancy is not a missing or underestimated systematic uncertainty. New calculations with the Double Pole Approximation (DPA) [50] have recently appeared and two Monte Carlo programs, `YFSWW3` [51] and `RacoonWW` [52], which include them are being developed. The predicted CC03 cross section from these Monte Carlos appears to be between 1.5 and 2% lower than the `KORALW` prediction [53], therefore being in better agreement with the ALEPH WW cross section measurements. The results presented here have been obtained using the `KORALW` prediction for the WW cross section. The new DPA results have not been considered, as the final versions of these new Monte Carlos are still not available at the time of writing this thesis.

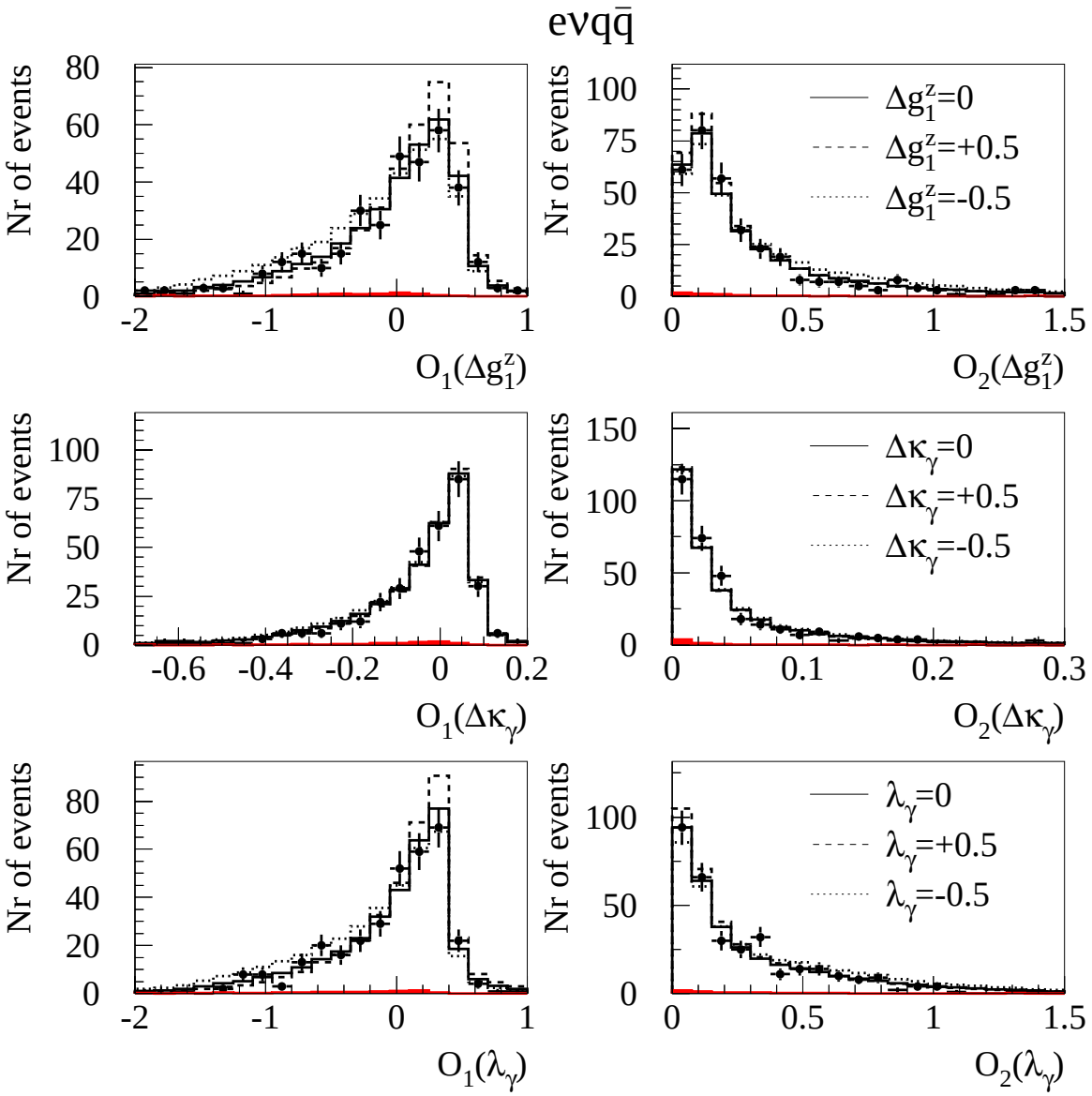

Figure 5.7: Optimal observable distributions for $e\nu q\bar{q}$ events. The data (dots) are compared to MC distributions reweighted to different TGC values. The background contribution is shown as a shaded histogram.

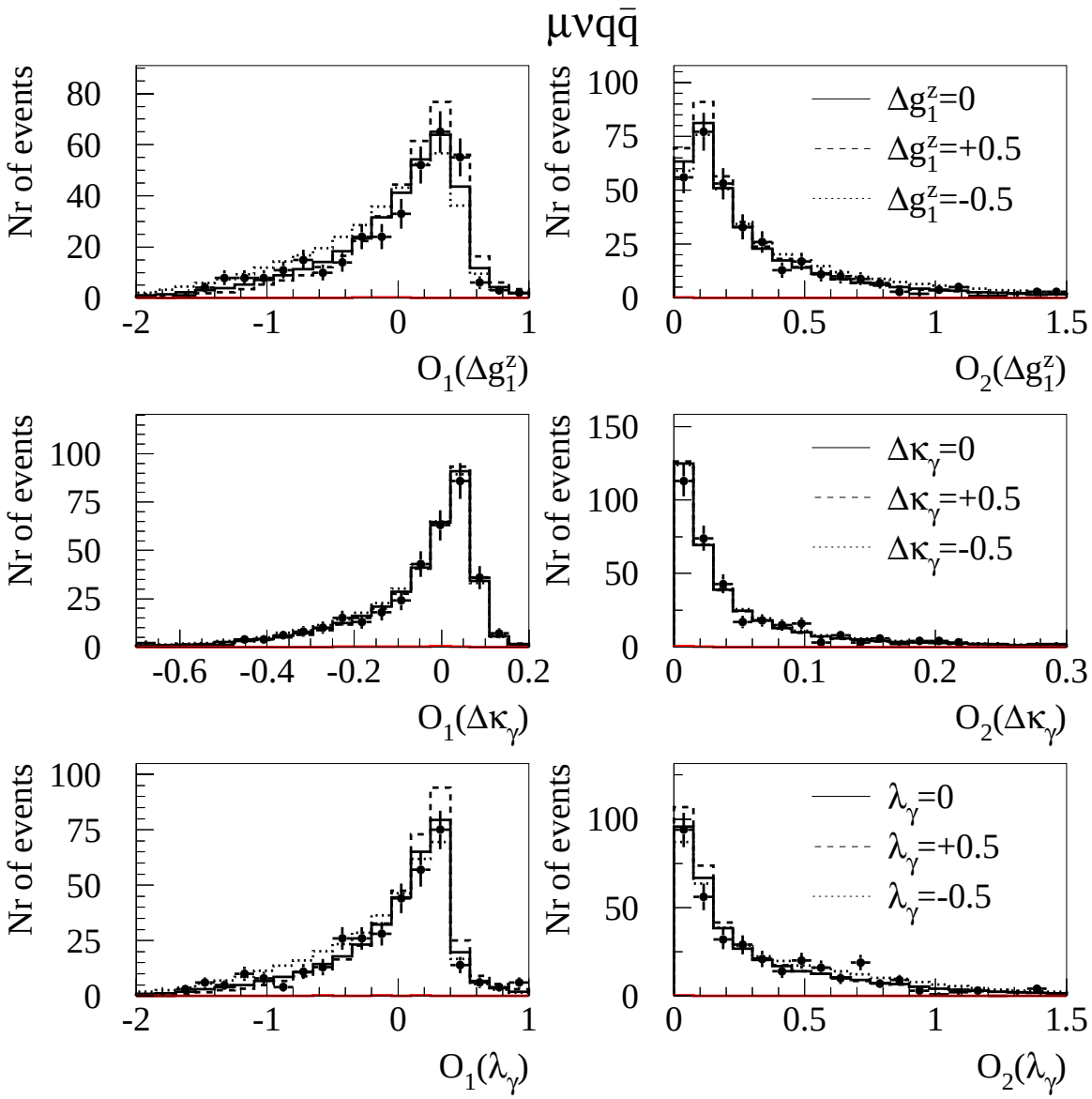

Figure 5.8: Optimal observable distributions for $\mu\nu q\bar{q}$ events. The data (dots) are compared to MC distributions reweighted to different TGC values. The background contribution is shown as a shaded histogram.

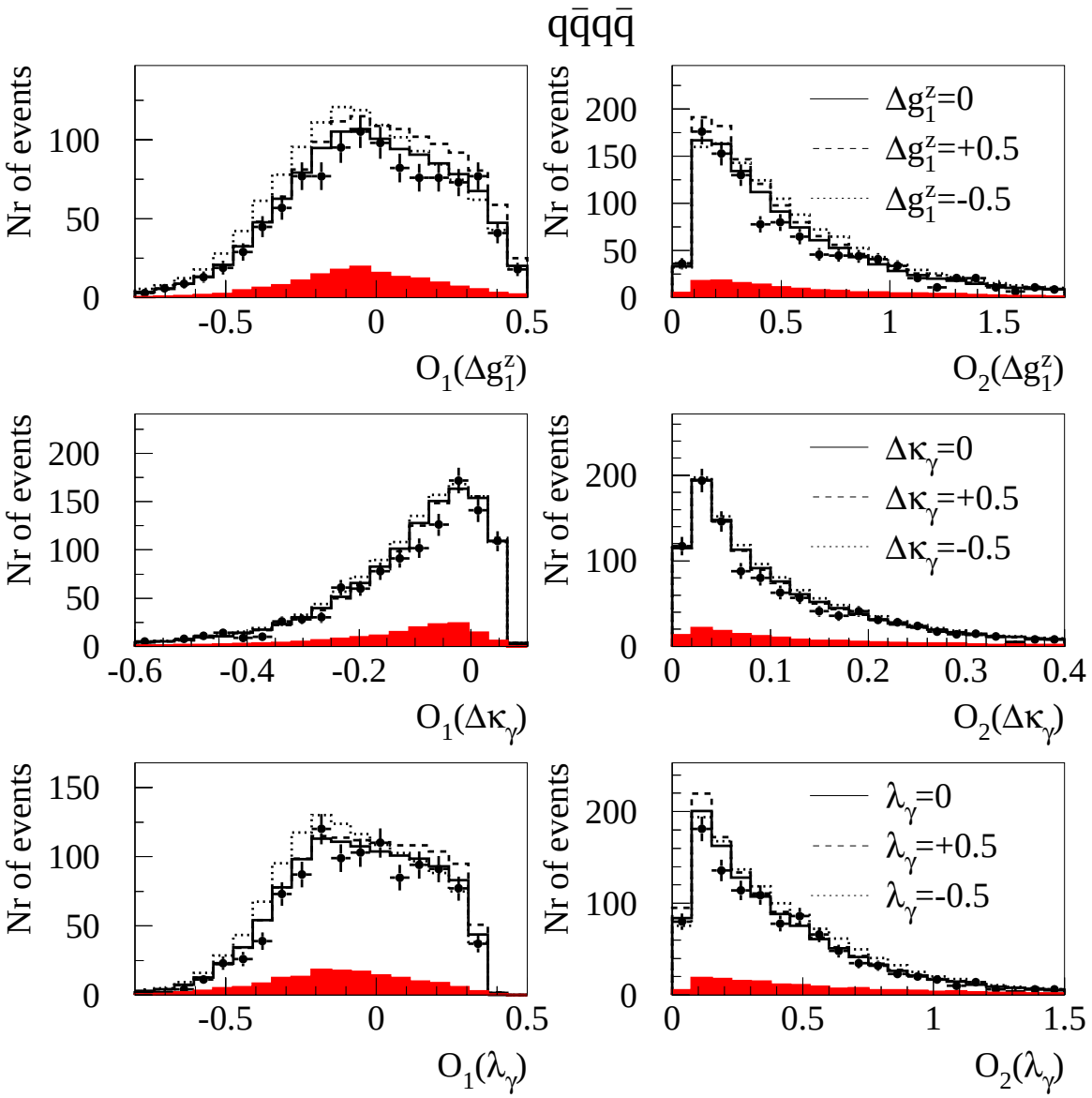

Figure 5.9: Optimal observable distributions for $q\bar{q}q\bar{q}$ events. The data (dots) are compared to MC distributions reweighted to different TGC values. The background contribution is shown as a shaded histogram.

5.2.5 W charge assignement

As already discussed in Sect. 4.1.3, it is crucial for the TGC measurement to tag the charge of the W bosons in the event. This is straightforward for the semileptonic W pair decays, where the charge of the lepton tags that of the parent W boson. However, in the purely hadronic WW decays this information is missing. Therefore, performing jet charge tagging is mandatory if one wants to recover it.

Given a certain jet pairing, a jet charge algorithm is used to assign a jet pair to the W^+ or W^-. The charge difference between the two W systems leads to a relatively high separation efficiency. The jet charge is obtained from the pseudo-rapidity weighted charge of the jet particles

$$Q_j = \frac{\sum_i q_i y_i}{\sum_i y_i} ; \qquad y \equiv \frac{1}{2}\ln\Big(\frac{E+p_z}{E-p_z}\Big) \tag{5.7}$$

where the sum runs over all those particles assigned to the jet. The difference of the charges assigned to each of the two W systems is then taken as an estimator to tag the W charges

$$\Delta Q \equiv Q_{j_3} + Q_{j_4} - Q_{j_1} - Q_{j_2} \, . \tag{5.8}$$

The a-posteriori probability that a certain jet pair $\{j_1, j_2\}$ corresponds to the W^-, $\mathcal{P}(W^-_{[j_1,j_2]}|\Delta Q)$, is an optimal variable to separate those events in which the W charge assignement has been correct from those in which it has not. Monte Carlo WW events can then be used to compute the a-priori probabilities $\mathcal{P}(\Delta Q|W^-_{[j_1,j_2]})$ and $\mathcal{P}(\Delta Q|W^-_{[j_3,j_4]})$. Since $\mathcal{P}(\Delta Q|W^-_{[j_3,j_4]}) = \mathcal{P}(-\Delta Q|W^-_{[j_1,j_2]})$, the discriminating variable is computed from the Monte Carlo distributions as

$$\mathcal{P}(W^-_{[j_1,j_2]}|\Delta Q) = \frac{\mathcal{P}(\Delta Q|W^-_{[j_1,j_2]})}{\mathcal{P}(\Delta Q|W^-_{[j_1,j_2]}) + \mathcal{P}(-\Delta Q|W^-_{[j_1,j_2]})} \, . \tag{5.9}$$

The evolution of this variable with respect to ΔQ is displayed in Fig. 5.10 as well as the distribution $\mathcal{P}(\Delta Q|W^-_{[j_1,j_2]})$ from WW Monte Carlo events.

The charge assignement efficiency for correctly paired hadronic WW events amounts to 74% for a cut on $\mathcal{P}(W^-_{[j_1,j_2]}|\Delta Q) > 0.5$.

In the analysis of the purely hadronic events, none of all the possible permutations of the final state four-momenta is discarded. Instead, they are all entering in the optimal

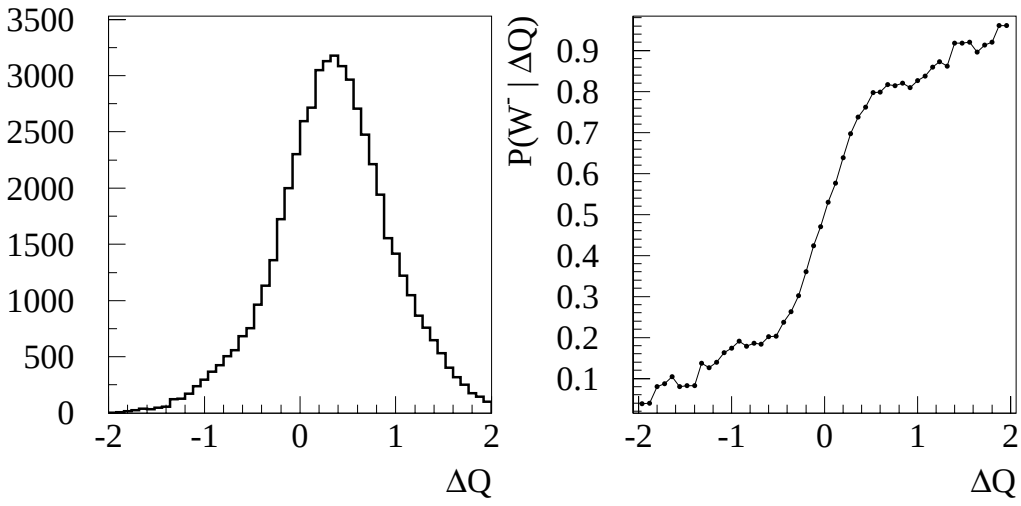

Figure 5.10: Left: $\mathcal{P}(\Delta Q|\mathrm{W}^-_{[j_1,j_2]})$ distribution for correctly paired $e^+e^- \to W^+W^- \to q\bar{q}q\bar{q}$ events. Right: Sensitive variable $\mathcal{P}(\mathrm{W}^-_{[j_1,j_2]}|\Delta Q)$ as a function of the observable ΔQ.

observable definitions with a certain weight, as described in section 4.1.3. The observable ΔQ is chosen to discriminate among the different permutations, therefore a weight

$$w_p(\Delta Q) = \mathcal{P}(\mathrm{W}^-_{[j_1,j_2]}|\Delta Q) \tag{5.10}$$

is assigned to each of them.

5.3 Monte Carlo experiments

5.3.1 Calibration curves

The reweighting method applied in this analysis to fit the TGCs is, by definition, bias free as long as there is no effect in the data sample which is not reproduced by the reference Monte Carlo.

In spite of this, the linearity of the method has been checked using dedicated WW Monte Carlo samples generated with non-vanshing couplings $g_i = \pm 0.5$ (see Table 5.1) to which background events have been added in the adequate proportion. A straight line $g_{fit} = a \cdot g_{true} + b$ is then fitted to the obtained points as illustrated in Fig. 5.11.

The results for the a and b parameters of the straight line fits are summarised in Table 5.5. No abnormal discrepancy from linearity is found in any of the studied cases.

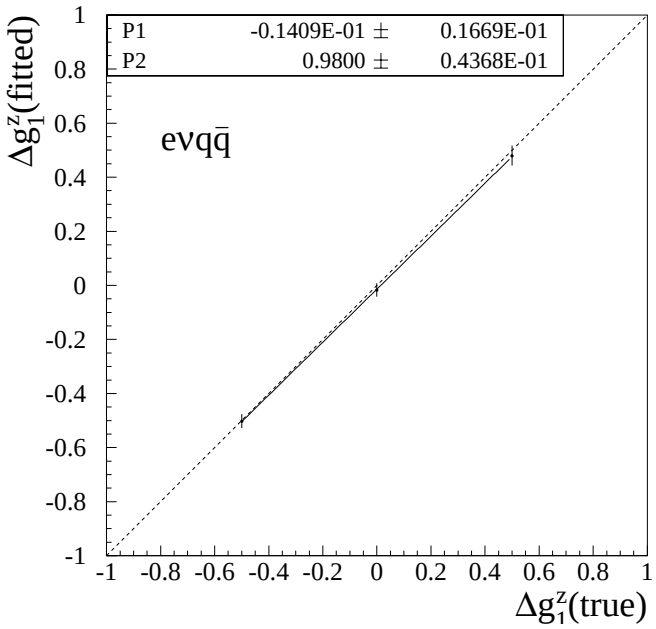

Figure 5.11: Δg_1^Z calibration curve for $e\nu q\bar{q}$ events. Only the angular information is used in the fit.

		$e\nu q\bar{q}$	$\mu\nu q\bar{q}$	$q\bar{q}q\bar{q}$
Δg_1^Z	a	0.98 ± 0.04	1.02 ± 0.04	1.00 ± 0.07
	b	-0.02 ± 0.02	0.03 ± 0.02	-0.01 ± 0.03
$\Delta\kappa_\gamma$	a	0.99 ± 0.14	0.80 ± 0.14	$0.99^{+0.19}_{-0.17}$
	b	0.05 ± 0.06	-0.03 ± 0.06	$-0.09^{+0.08}_{-0.07}$
λ_γ	a	0.91 ± 0.04	1.02 ± 0.04	0.94 ± 0.08
	b	-0.03 ± 0.02	0.00 ± 0.02	-0.03 ± 0.03

Table 5.5: Results of the calibration curves: Slope (a) and zero intercept (b)

5.3.2 Expected error

A large number of Monte Carlo samples, with equal number of events as observed in the data, generated with SM couplings is used to compute the expected error of the coupling estimators. The number of events of each class (signal and different backgrounds) per sample are allowed to vary multinomially according to their proportions.

From each of these samples, the TGCs are extracted by using only the angular information. The obtained estimator and fitted error distributions for each channel are shown in Figs. 5.12, 5.13 and 5.14. In order to test the reliability of the error estimate, the fraction of Monte Carlo samples in which the error interval contains the true value

of the coupling is computed. In all cases this fraction is found to be compatible with 68.3%, hence showing the reliability of the fitted errors. The unbiasedness of the method is checked by summing up the χ^2 curves from all the Monte Carlo experiments, which yields results compatible with the coupling values used in the Monte Carlo generation for all channels and couplings tested.

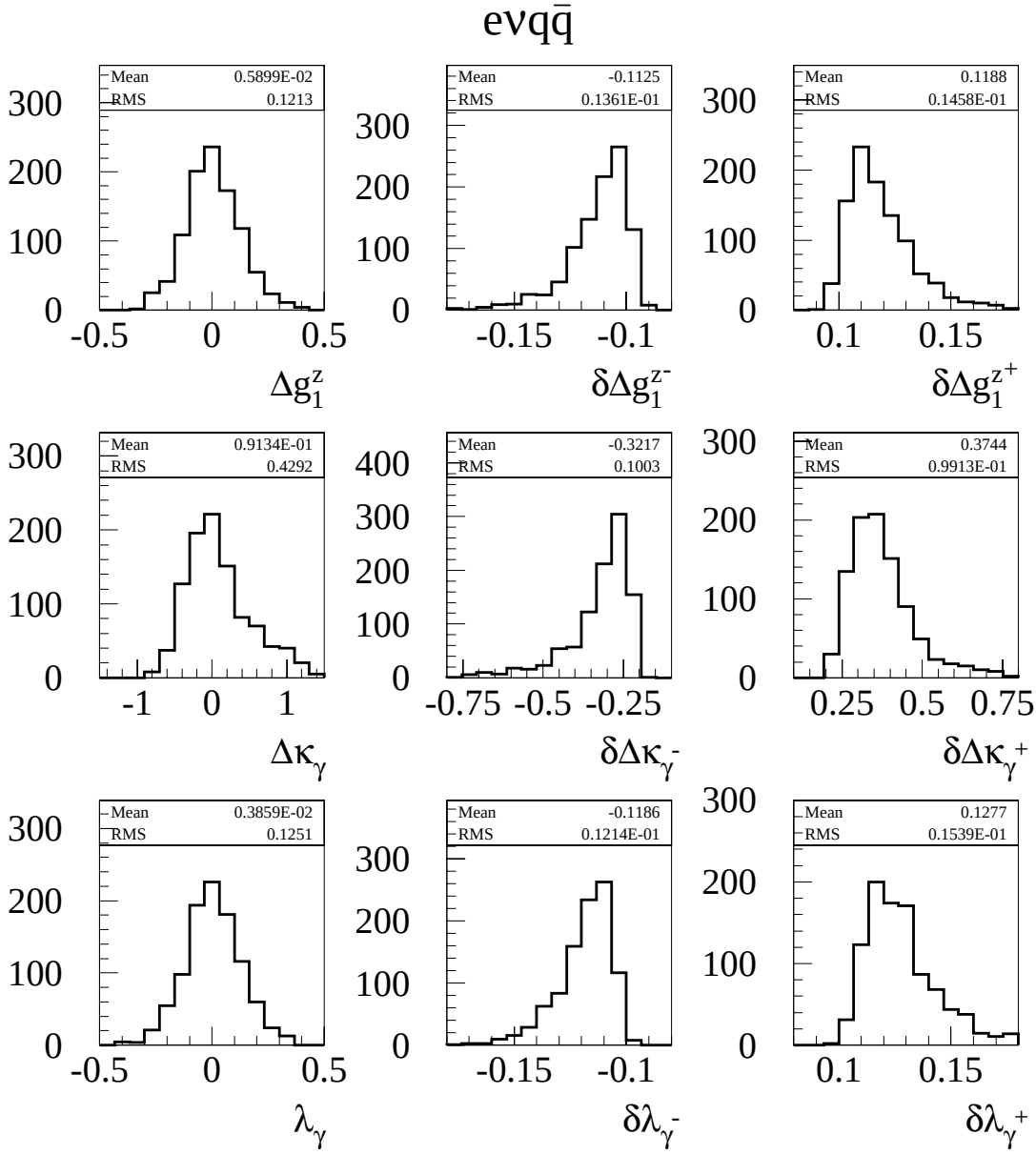

Figure 5.12: Fitted coupling and error distributions from many Monte Carlo $e\nu q\bar{q}$ samples, each one containing the same number of events as observed in the data.

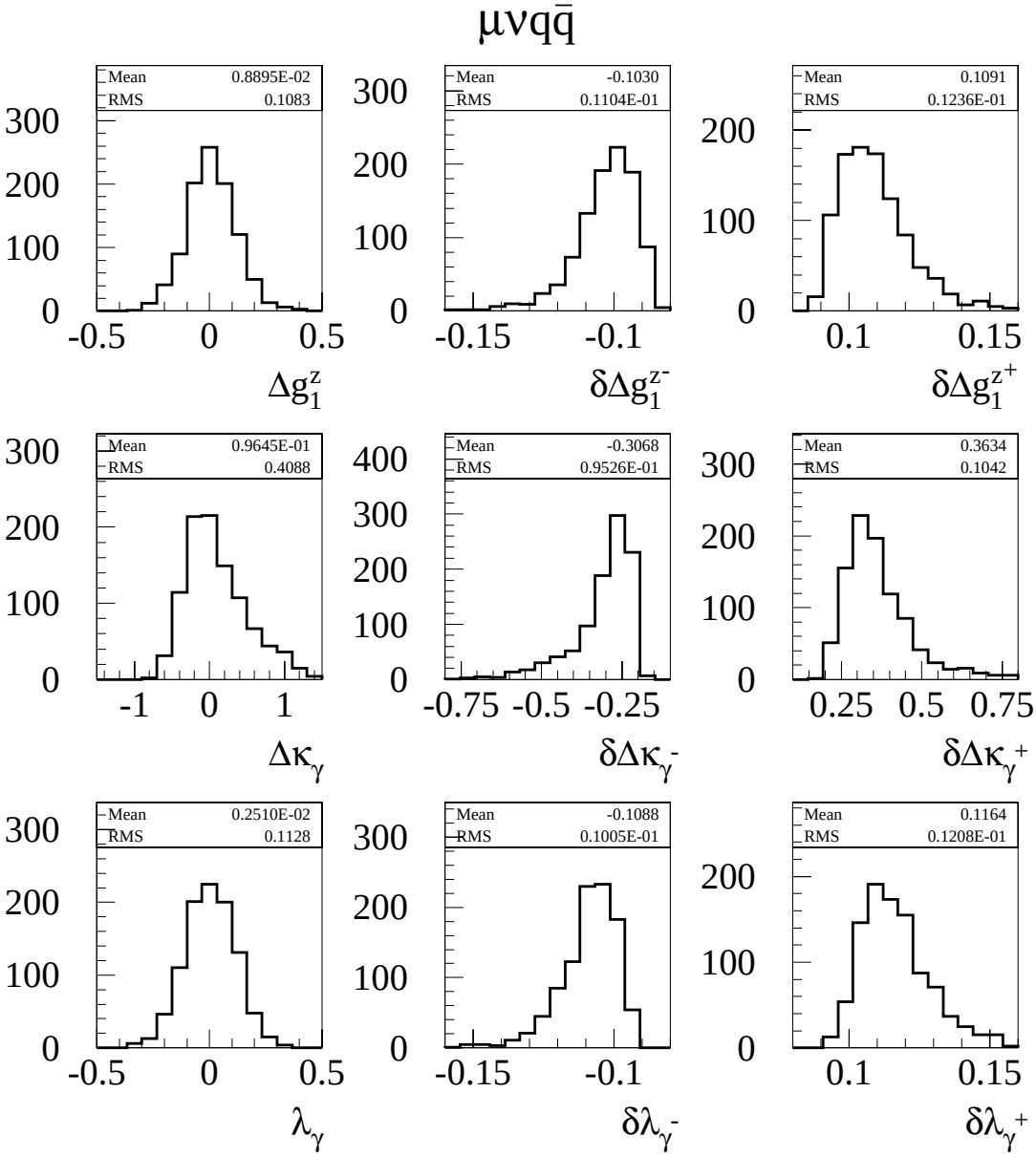

Figure 5.13: Fitted coupling and error distributions from many Monte Carlo $\mu\nu q\bar{q}$ samples, each one containing the same number of events as observed in the data.

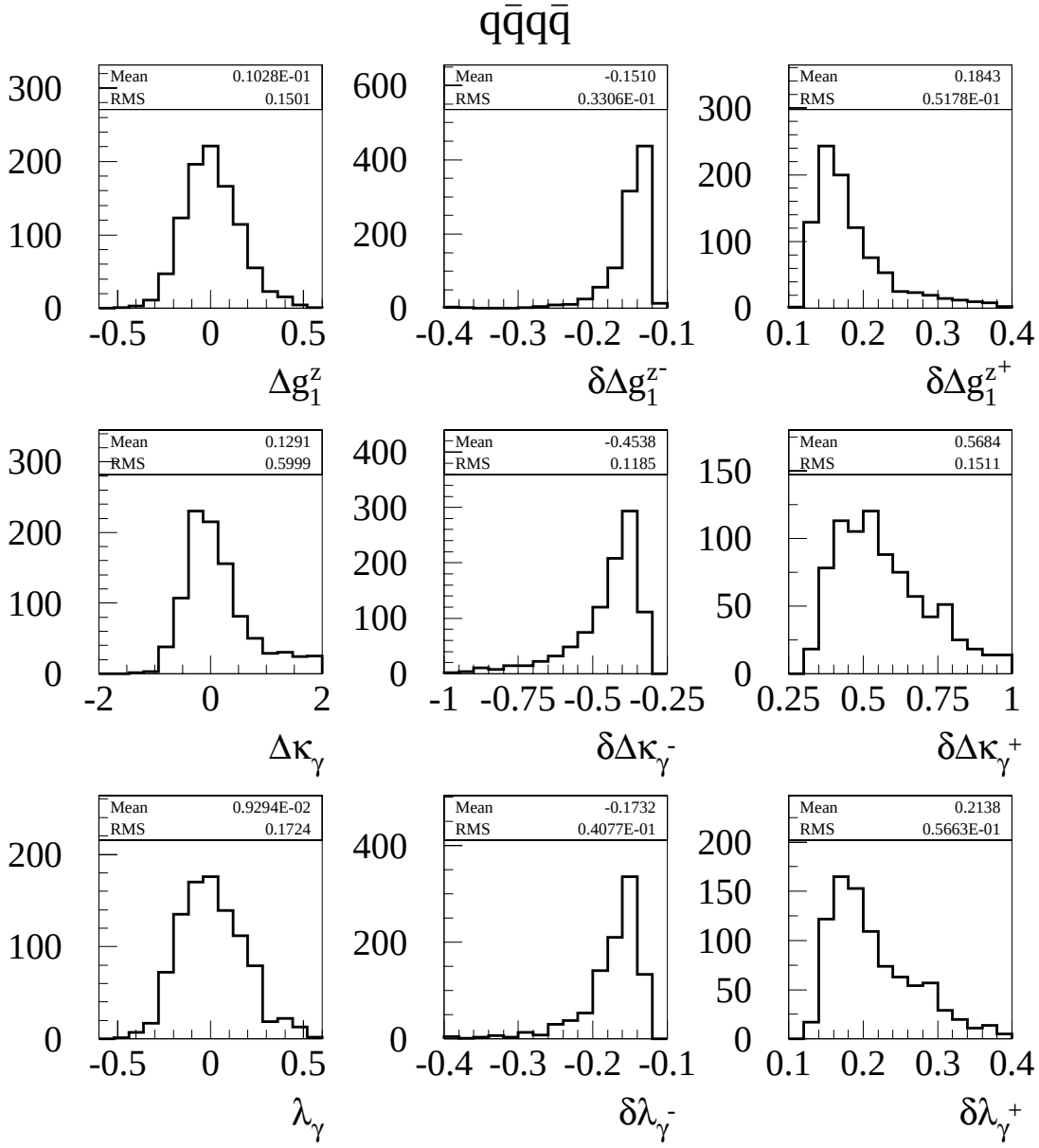

Figure 5.14: Fitted coupling and error distributions from many Monte Carlo $q\bar{q}q\bar{q}$ samples, each one containing the same number of events as observed in the data.

Chapter 6

TGC measurement

The method of optimal observables has been applied to determine the TGCs Δg_1^Z, $\Delta\kappa_\gamma$ and λ_γ using semileptonic and purely hadronic WW decays selected from the data sample collected by ALEPH during the year 1998 at a centre of mass energy of 188.6 GeV corresponding to an integrated luminosity of 174.2 pb^{-1}.

In this analysis the TGCs are extracted assuming different scenarios. Most of the results are obtained fitting each coupling separately, while the other two are fixed to their SM value. Two-dimensional and three-dimensional fits are also performed, where two or all three couplings are fitted simultaneously.

As described in chapter 4, the TGCs are extracted by means of a least squares fit, by minimising the quantity

$$\chi^2(\vec{g}) = \sum_{ij}(M_i - T_i(\vec{g}))\ (V^{-1})_{ij}\ (M_j - T_j(\vec{g}))\ , \tag{6.1}$$

where M_i denote a set of measured quantities and T_i their theoretical predictions, which are function of the parameters $\vec{g}$ to be determined.

For each decay channel, the measured quantities M_i are the number of observed events N_{obs}, and the mean values of the first and second order optimal observables $\{\langle\mathcal{O}_{1,i}\rangle, \langle\mathcal{O}_{2,i}\rangle\ ;\ i = \Delta g_1^Z, \Delta\kappa_\gamma, \lambda_\gamma\}$. When combining the information of several decay channels, one needs to extend the sum in (6.1) so that all the measurements are included in the χ^2. The combined result is the one obtained by performing a least squares fit using this global χ^2.

An advantage of this formalism is that it naturally allows to include gaussian systematic uncertainties in the measured quantities. This is done by adding systematic

components to the statistical covariance matrix

$$V_{ij} = V_{ij}^{stat} + \sum_{syst} V_{ij}^{syst} \, , \tag{6.2}$$

therefore allowing to consider some systematics being correlated among different channels.

6.1 Systematic uncertainties

The Monte Carlo reweighting procedure employed in this analysis to measure the TGCs relies on a correct simulation of both detector and physics effects. As a consequence, any effect which is not well reproduced by the simulation might be the origin of systematic uncertainties.

All the systematic errors are evaluated as uncertainties in the measured quantities, which are then used as building blocks for V_{ij}^{syst} in (6.2):

$\delta N \rightarrow$ Systematics affecting the total cross section measurement are computed as uncertainties in the number of events expected for a given channel.

$\delta\langle\mathcal{O}\rangle \rightarrow$ Systematics affecting the angular distributions of the WW decay products are computed as uncertainties in the optimal observable mean values.

The first ones are readily computed from (4.31) by error propagation. Their sources are briefly described in subsections 6.1.2 and 6.1.3 and they are listed in Table 6.2.

To estimate the uncertainties in the optimal observable mean values, two different approaches are used. Whenever it is possible, the size of the systematic $\delta\langle\mathcal{O}\rangle$ is computed by error propagation as detailed in Appendix A. The rest of systematic effects affecting the angular distributions are studied using large dedicated samples of fully reconstructed Monte Carlo events. The systematic uncertainties $\delta\langle\mathcal{O}\rangle$ are then evaluated as the shift observed in the measured $\langle\mathcal{O}\rangle$ from these samples when the different systematic effects are applied.

The different sources of systematic uncertainties considered are briefly described in the following subsections.

6.1.1 Systematics affecting the angular distributions

LEP energy

The uncertainty in the LEP energy affects the reconstruction of the WW decay products through the kinematic fit constraint. The effect that a 20 MeV uncertainty in the LEP energy [54] has on the determination of the optimal observable mean values is taken as a systematic for the TGC measurement. This is done by computing the shifts appearing in the measured $\langle\mathcal{O}\rangle$ from a large fully reconstructed Monte Carlo sample when the centre of mass energy assumed in the kinematic fit is varied around its nominal value by this amount.

W mass

Monte Carlo samples generated with different values for the W mass have been used to determine the slope $\frac{\partial\langle\mathcal{O}\rangle}{\partial M_W}$, assuming there is a linear dependence between the measured $\langle\mathcal{O}\rangle$ and the the W mass at which each sample has been generated. The uncertainty in the W mass as measured from the hadron colliders $\delta M_W = 60$ MeV [55][1] has been then translated into an uncertainty in $\langle\mathcal{O}\rangle$

$$\delta\langle\mathcal{O}\rangle = \frac{\partial\langle\mathcal{O}\rangle}{\partial M_W}\delta M_W \tag{6.3}$$

and taken as a systematic error.

Finite Monte Carlo statistics

Another source of systematic uncertainty one must take into account is the effect of limited statistics in the reference Monte Carlo sample used to predict the expected value of the optimal observables as a function of the TGCs. Since this prediction is a weighted average (see Eq. (4.18)), its variance can be analytically computed, as detailed in Appendix B, and directly included as a systematic error.

Initial state radiation

ISR is implemented in `KORALW` up to $\mathcal{O}(\alpha^2 L^2)$, i.e. up to second order in the leading-log approximation. The effect of the missing higher order terms is estimated by weighting

[1] The LEP W mass measurements are not used, since they have been obtained under the assumption of SM TGCs, whereas W production at the Tevatron does not involve the triple gauge boson vertex.

each event in a specific KORALW sample with the ratio of first to second order squared matrix elements $\mathcal{O}(\alpha^1 L^1)/\mathcal{O}(\alpha^2 L^2)$. The systematic error is then taken as the difference between the $\langle\mathcal{O}\rangle$ obtained with the weighted events and that from unweighted events.

Charged particle tracking

After the detector alignment, small distortions remain in the momentum measurement, which are absent in the Monte Carlo simulation. The main corrections for these distortions are determined by equalising the momenta of the two charged tracks in $Z^0 \to \mu^+\mu^-$ events. However, remaining distortions are also estimated using Bhabha events. These corrections are applied to all data events. Using a large sample of KORALW events, a systematic uncertainty associated to these corrections is estimated as the shift appearing in $\langle\mathcal{O}\rangle$ when these corrections are applied to the lepton track of selected semileptonic decays.

Jet energy corrections before the kinematic fit

The data collected at the Z^0 peak at the start and end of the LEP run in 1998 is used to compare the jet energies in data and Monte Carlo. The observed biases do not exceed 0.5% in the barrel region but increase up to 3.5% for $|\cos\theta_{jet}| > 0.95$. The Monte Carlo reconstructed jet energies are corrected for these biases as a function of $\cos\theta_{jet}$ before the kinematic fit is applied. The largest shift in $\langle\mathcal{O}\rangle$ observed in a large Monte Carlo sample when this correction is varied by $\pm 1\sigma$ is then quoted as the systematic uncertainty associated to this correction.

6.1.2 Systematics affecting the cross section

Luminosity

The relative error on the integrated luminosity recorded by ALEPH during the year 1998 is 0.48%. This is translated into a systematic uncertainty on the TGCs through the cross section measurement. Its size is quoted in Table 6.2.

Efficiency statistical error

The statistical uncertainty in the signal and background efficiencies used in the cross section measurement are also considered as a source of systematic error.

6.1.3 Systematics affecting the angular distributions and the cross section

WW cross section

A 2% theoretical uncertainty in the W pair cross section prediction has been assumed [59]. This directly produces a systematic uncertainty in the TGCs measured through the cross section. Moreover, the measurement of the optimal observables is also affected through the change in the purity of the selection.

Background normalisation

The cross section of the main background processes is varied in the fit in order to account for an eventual disagreement between data and Monte Carlo concerning the background normalisation. From comparisons between data and Monte Carlo, the QCD background normalisation uncertainty is taken to be 5%. The $\gamma\gamma$, Zee and ZZ cross sections are varied by $\pm 30\%$, $\pm 20\%$ and $\pm 2\%$, respectively, corresponding to the uncertainties in the simulation of these processes.

Calorimeters calibration

Another source of systematic uncertainty which has been considered is the possibility of a miscalibration in the absolute energy scale of ECAL and/or HCAL. The observed discrepancies between data and Monte Carlo lead to consider $\pm 0.9\%$ in ECAL and $\pm 2\%$ in HCAL as safe estimates of these deviations. The effect of a possible miscalibration on the measured $\langle \mathcal{O} \rangle$ is estimated by rescaling all calorimetric energy deposits independently by these amounts in a large Monte Carlo sample and determining the shifts that this produces in $\langle \mathcal{O} \rangle$. A systematic error is then assigned for each calorimeter, where the largest observed shift is taken in both cases. The uncertainty that this effect causes in the signal efficiency determination has been evaluated and used to quote a systematic error affecting the total cross section measurement.

Fragmentation

The uncertainty in the fragmentation model assumed in the W $\rightarrow q\bar{q}$ decays is investigated by comparing the nominal JETSET fragmentation with that of HERWIG [56] (both tuned to the ALEPH Z^0 data). To do so, a large sample of KORALW events is used, such that each event is hadronised by both models and then processed by the full detector simulation. The observed difference in the measured $\langle\mathcal{O}\rangle$ from these two samples is taken as a systematic error. For the cross section measurement, the difference in the selection efficiencies determined from both samples is used to assign a systematic uncertainty.

Colour reconnection

Colour reconnection effects are tested using a dedicated $W^+W^- \rightarrow q\bar{q}q\bar{q}$ Monte Carlo sample where every event is hadronised using JETSET in two different ways: one uses the standard hadronisation and the other includes colour reconnection through the SK1 model [16]. A mixed sample of reconnected and non-reconnected events is built as described in [57] such that the fraction of reconnected events in this sample is $\sim 30\%$. The observed differences in the measured $\langle\mathcal{O}\rangle$ and in the selection efficiencies from both Monte Carlo samples are again used to compute the systematic errors.

Bose-Einstein correlations

Bose-Einstein correlations effects are tested using also a dedicated $W^+W^- \rightarrow q\bar{q}q\bar{q}$ Monte Carlo sample where every event is hadronised using JETSET in two different ways: one uses the standard hadronisation and the other includes Bose-Einstein correlations through the LUBOEI [19] model. In this model the momentum of identical bosons in the final state is shifted in order to reproduce the two pion correlation function. Energy and momentum conservation is then restored through the scheme denoted BE_3 [19] which has been tuned to LEP1 Z^0 data [58]. The observed differences in the measured $\langle\mathcal{O}\rangle$ and in the selection efficiencies from both Monte Carlo samples are again used to compute the systematic errors.

6.2 Results

6.2.1 Single channel results

One-dimensional fits

One-dimensional fits to the 189 GeV data are performed for each of the three WW decay channels studied. The results are quoted in Table 6.1, where the successive effect of, first, considering the total cross section information and, second, including the systematic errors, is shown. The confidence intervals quoted in Table 6.1 correspond to the one standard deviation errors (68.3% confidence level), which are obtained by taking the TGC values where $\Delta\chi^2 = 1$ above the minimum. No significative deviation from the SM is found in these results.

		Δg_1^Z	$\Delta\kappa_\gamma$	λ_γ
$e\nu q\bar{q}$	$\frac{d\sigma}{d\Omega}$	$-0.009^{+0.101}_{-0.097}$	$0.326^{+0.346}_{-0.307}$	$-0.042^{+0.113}_{-0.107}$
	$\sigma_T + \frac{d\sigma}{d\Omega}$	$-0.007^{+0.096}_{-0.093}$	$0.329^{+0.314}_{-0.286}$	$-0.034^{+0.108}_{-0.102}$
	Including Syst.	$-0.018^{+0.097}_{-0.093}$	$0.316^{+0.326}_{-0.291}$	$-0.049^{+0.108}_{-0.102}$
$\mu\nu q\bar{q}$	$\frac{d\sigma}{d\Omega}$	$-0.068^{+0.103}_{-0.097}$	$0.031^{+0.394}_{-0.284}$	$-0.147^{+0.100}_{-0.095}$
	$\sigma_T + \frac{d\sigma}{d\Omega}$	$-0.062^{+0.100}_{-0.093}$	$0.072^{+0.382}_{-0.270}$	$-0.134^{+0.096}_{-0.090}$
	Including Syst.	$-0.063^{+0.100}_{-0.094}$	$0.067^{+0.384}_{-0.272}$	$-0.137^{+0.097}_{-0.091}$
$q\bar{q}q\bar{q}$	$\frac{d\sigma}{d\Omega}$	$-0.035^{+0.160}_{-0.135}$	$-0.130^{+0.546}_{-0.392}$	$0.121^{+0.330}_{-0.193}$
	$\sigma_T + \frac{d\sigma}{d\Omega}$	$0.000^{+0.105}_{-0.098}$	$0.304^{+0.346}_{-0.289}$	$0.076^{+0.124}_{-0.117}$
	Including Syst.	$-0.011^{+0.121}_{-0.110}$	$0.237^{+0.417}_{-0.322}$	$0.084^{+0.145}_{-0.135}$

Table 6.1: One-dimensional fit results.

The χ^2 curves corresponding to the one-dimensional fits including systematic errors are displayed in Figs. 6.1, 6.2 and 6.3. From these figures it can be seen that the TGC measurements from the semileptonic channels are clearly dominated by the angular information. In the purely hadronic channel, instead, both contributions have similar weight. This is due, on one hand, to the fact that the angular information is poorer because of the ambiguities when tagging the flavour of the fermions in the final state. On the other hand, the higher statistics of this channel, together with the fact of observing less events in the data than those predicted by the Monte Carlo, enhance the weight of the cross section contribution.

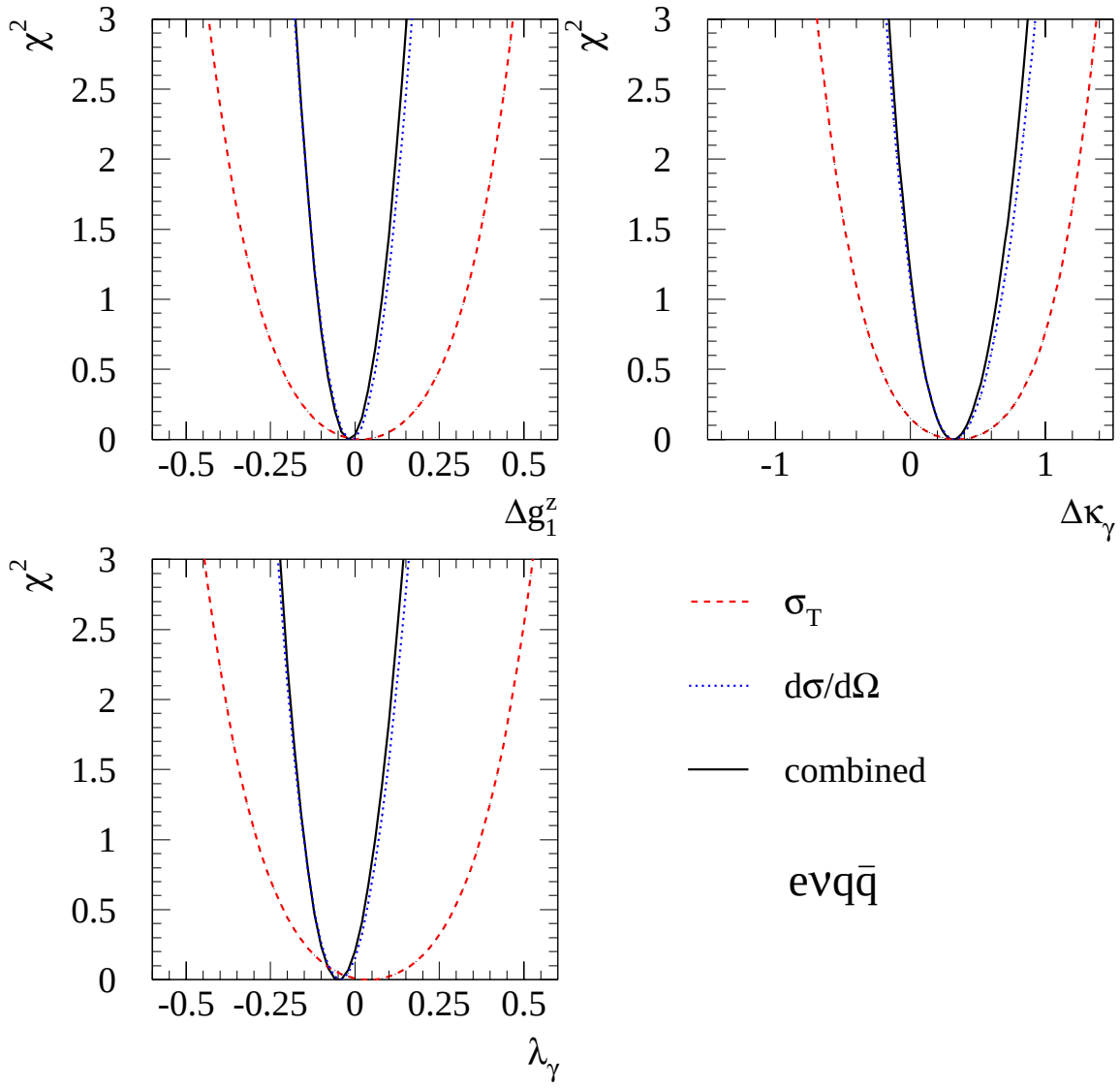

Figure 6.1: χ^2 curves obtained in one-dimensional fits to $e\nu q\bar{q}$ events. Systematic errors are included.

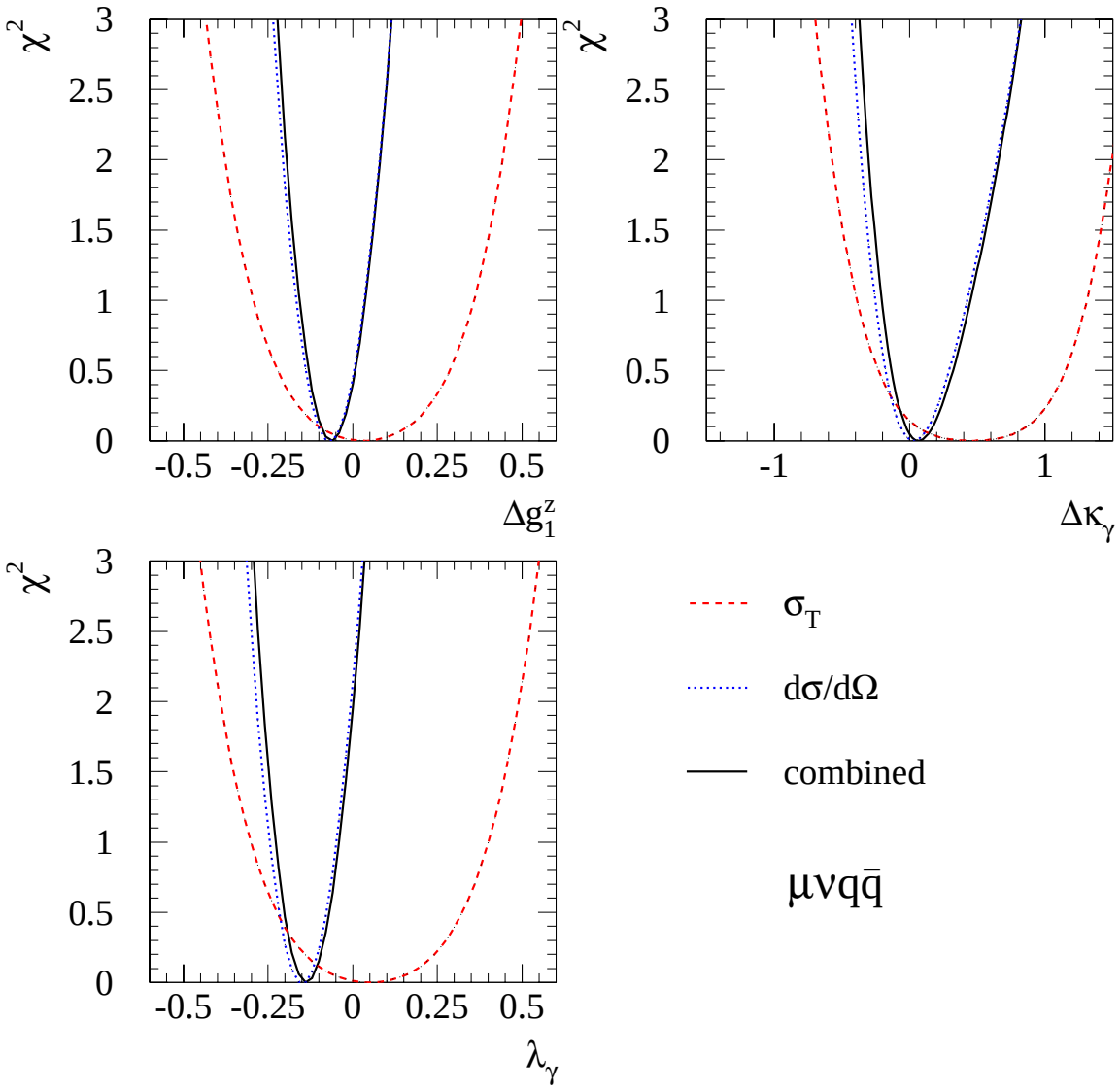

Figure 6.2: χ^2 curves obtained in one-dimensional fits to $\mu\nu q\bar{q}$ events. Systematic errors are included.

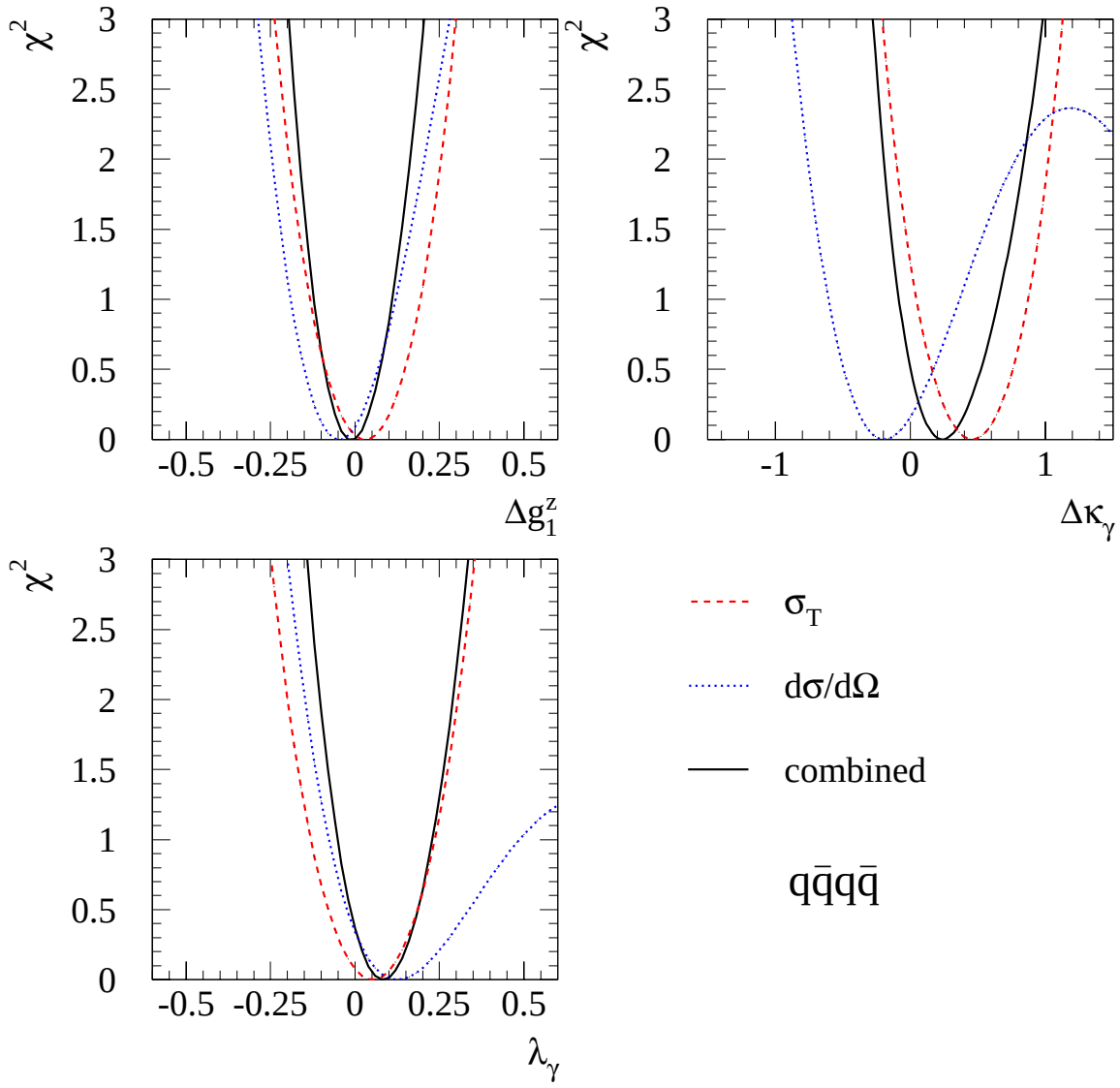

Figure 6.3: χ^2 curves obtained in one-dimensional fits to $q\bar{q}q\bar{q}$ events. Systematic errors are included.

As described in section 6.1, the systematic errors affecting the total cross section measurement are included in the fit as uncertainties in the expected number of events δN for a certain channel. Their values are listed in Table 6.2.

		$e\nu q\bar{q}$	$\mu\nu q\bar{q}$	$q\bar{q}q\bar{q}$
	$N_{expected}$	351.0	358.3	1320.5
	$N_{observed}$	337	350	1240
	σ_{WW}	6.8	7.1	22.0
	σ_{bckg}	0.4	0.0	9.7
δN	$\mathcal{L}$	1.7	1.7	6.3
Systematics	ϵ_{stat}	1.4	1.4	3.3
	Calorimeters calib.	0.6	0.5	4.5
	Fragmentation	-	-	0.9
	FSI	-	-	4.7

Table 6.2: Number of observed and expected events for each channel together with the size of the systematic errors affecting the cross section measurement (in number of events units).

Those systematics affecting the angular distributions are included in the fit as uncertainties in the mean value of the optimal observables $\delta\langle\mathcal{O}\rangle$. In order to illustrate the weight of these systematic errors in the fits, their relative size compared to the statistical uncertainty in $\langle\mathcal{O}\rangle$ is plotted in Figs. 6.4, 6.5 and 6.6. For those systematics which are determined using a finite sample of Monte Carlo events, the statistical accuracy with which the systematic shifts $\delta\langle\mathcal{O}\rangle$ are determined is shown as an error bar. When the statistical accuracy with which the systematic shift $\delta\langle\mathcal{O}\rangle$ is determined turns to be larger than the shift itself, the former is taken as the systematic error.

As it can be seen from the figures, the systematic error contribution to the total uncertainty in the semileptonic channels is going to be in general very small, as the largest systematic uncertainties appear to be $\sim 10\%$ of the statistical one. The systematic error associated to the fragmentation model is found to be one of the dominants in the three decay channels. In the semileptonic channels this error shows a large statistical uncertainty, however its size is still very small as compared to the couplings statistical uncertainties. In the purely hadronic channel, the size of this systematic error is essentially the same as the statistical uncertainty for some of the optimal observables.

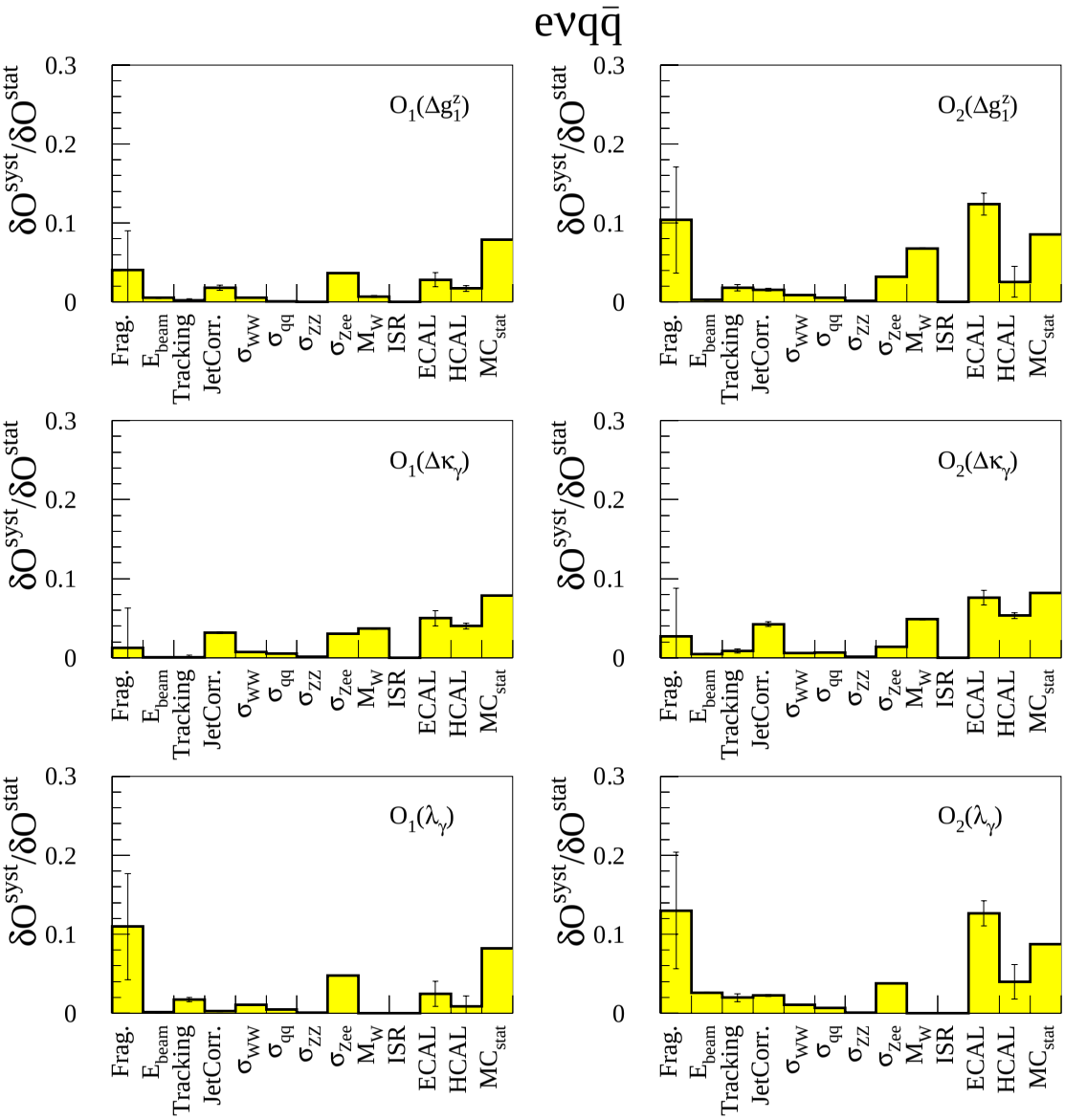

Figure 6.4: Relative size of the systematic errors affecting the measurements of the mean values of the optimal observables in the $e\nu q\bar{q}$ channel as compared to their statistical uncertainty.

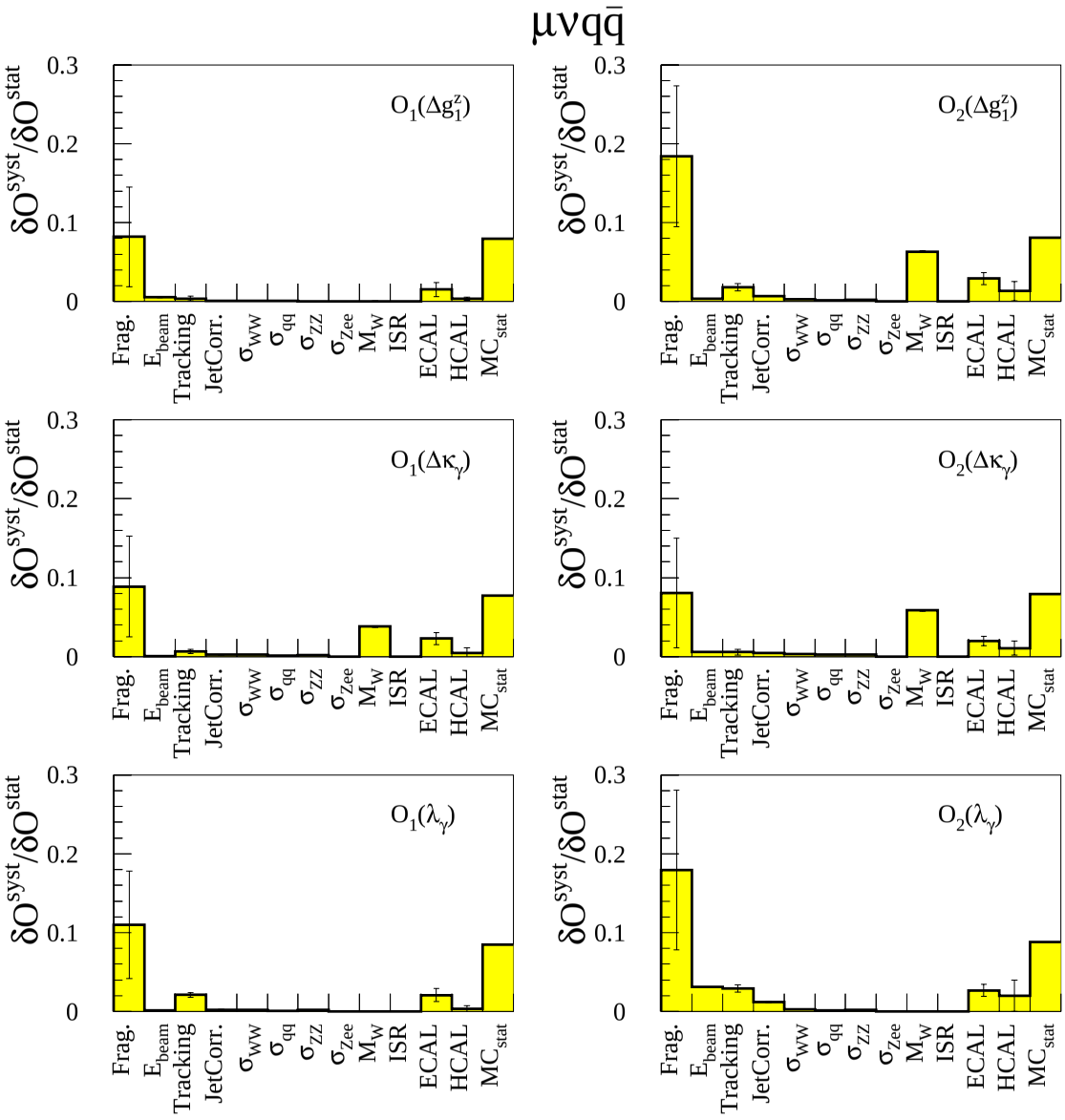

Figure 6.5: Relative size of the systematic errors affecting the measurements of the mean values of the optimal observables in the $\mu\nu q\bar{q}$ channel as compared to their statistical uncertainty.

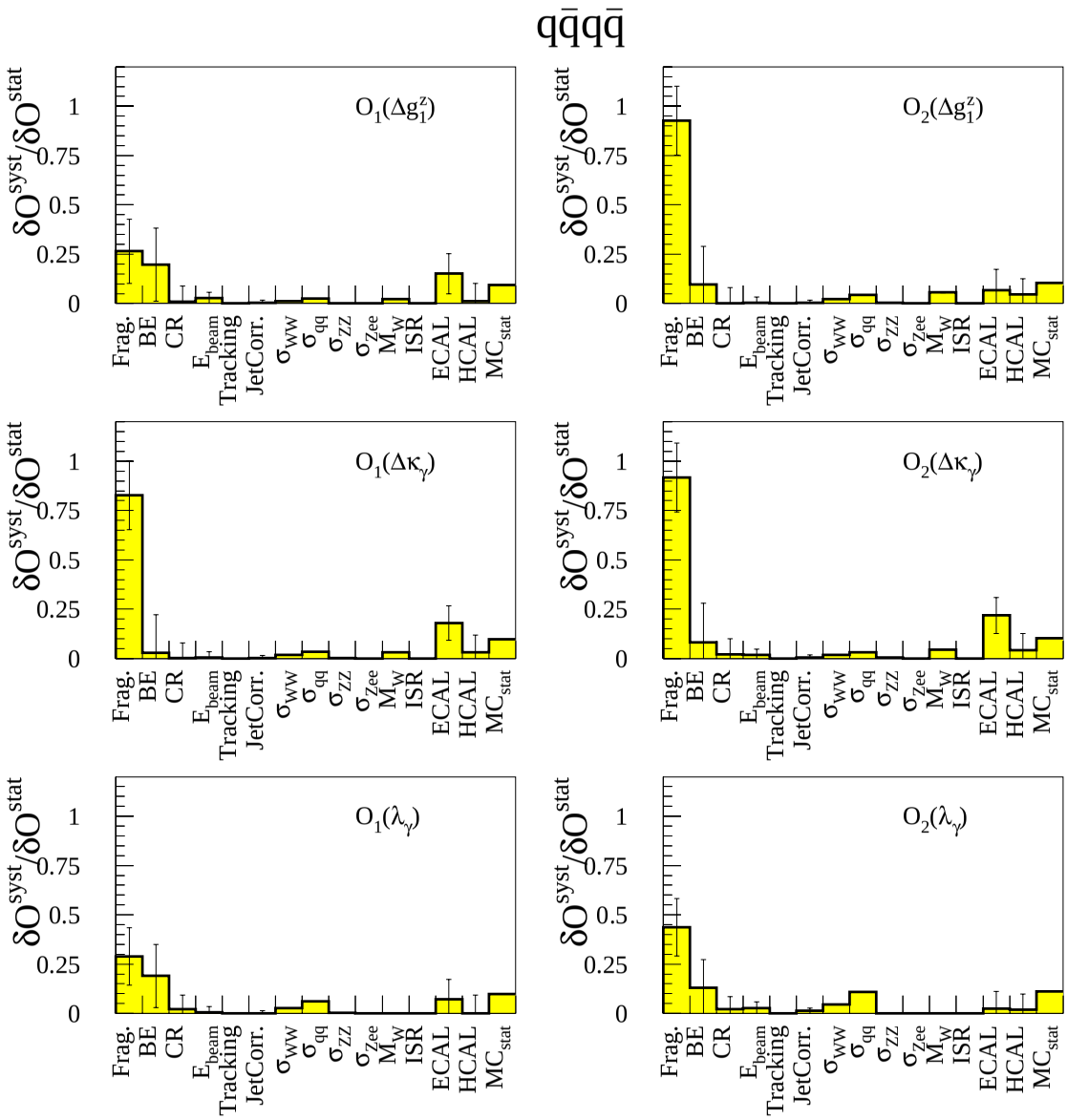

Figure 6.6: Relative size of the systematic errors affecting the measurements of the mean values of the optimal observables in the $q\bar{q}q\bar{q}$ channel as compared to their statistical uncertainty.

Multi-dimensional fits

Two-dimensional fits, where the third parameter is fixed to its SM value, are performed. The 95% confidence level contours are obtained by requiring $\Delta\chi^2 = 5.99$ and they are shown in Figs. 6.7, 6.8 and 6.9. Finally, a three-dimensional fit is performed in which the three couplings are allowed to vary simultaneously. The two-dimensional projections of the three-dimensional 95% confidence level contours, which are now obtained by requiring $\Delta\chi^2 = 7.82$, are plotted as shaded areas in Figs. 6.7, 6.8 and 6.9. The 95% confidence level intervals per coupling resulting from these multi-dimensional fits, given by the TGC values where $\Delta\chi^2 = 3.84$ above the minimum, are quoted in Table 6.3.

		Δg_1^Z	$\Delta\kappa_\gamma$	λ_γ
$e\nu q\bar{q}$		$[-0.217, 0.168]$	$[-0.218, 0.927]$	–
	2D	–	$[-0.178, 0.955]$	$[-0.279, 0.148]$
		$[-0.212, 0.238]$	–	$[-0.299, 0.209]$
	3D	$[-0.219, 0.262]$	$[-0.186, 0.963]$	$[-0.352, 0.186]$
$\mu\nu q\bar{q}$		$[-0.282, 0.13]$	$[-0.381, 0.994]$	–
	2D	–	$[-0.298, 1.102]$	$[-0.372, 0.035]$
		$[-0.203, 0.294]$	–	$[-0.404, 0.096]$
	3D	$[-0.245, 0.286]$	$[-0.304, 1.081]$	$[-0.43, 0.09]$
$q\bar{q}q\bar{q}$		$[-0.242, 0.21]$	$[-0.313, 1.069]$	–
	2D	–	$[-0.347, 1.034]$	$[-0.244, 0.347]$
		$[-0.322, 0.222]$	–	$[-0.203, 0.466]$
	3D	$[-0.323, 0.224]$	$[-0.344, 0.992]$	$[-0.26, 0.453]$

Table 6.3: Multi-dimensional fit 95% CL results.

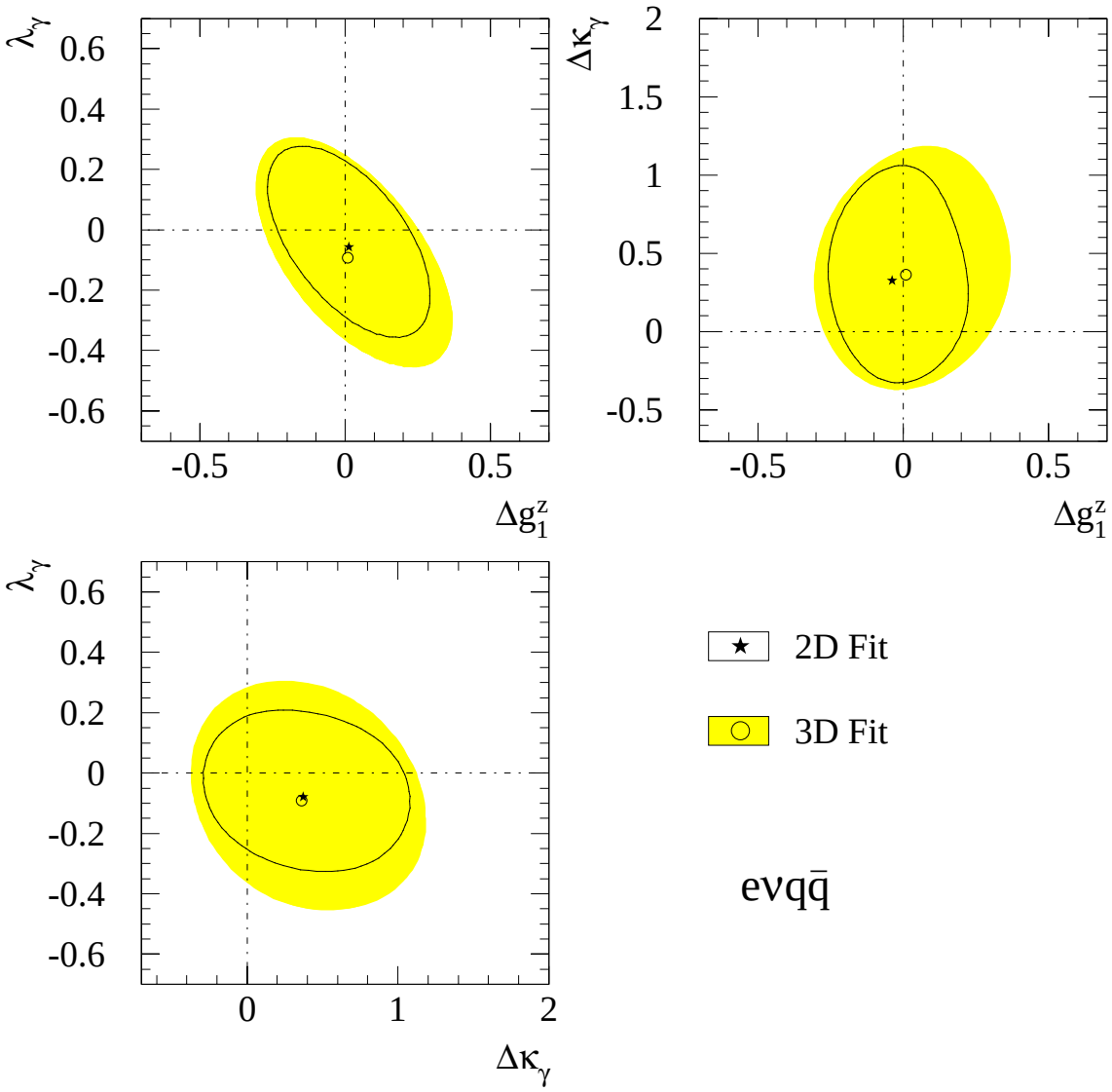

Figure 6.7: Multi-dimensional fit results for the $e\nu q\bar{q}$ channel. The 95% CL contours resulting from the two-dimensional fit are plotted as an open area. The shaded contours correspond to the two-dimensional projections of the 95% CL contour resulting from the three dimensional fit. Both the total cross section and angular information are used in the fits. The systematic uncertainties are included.

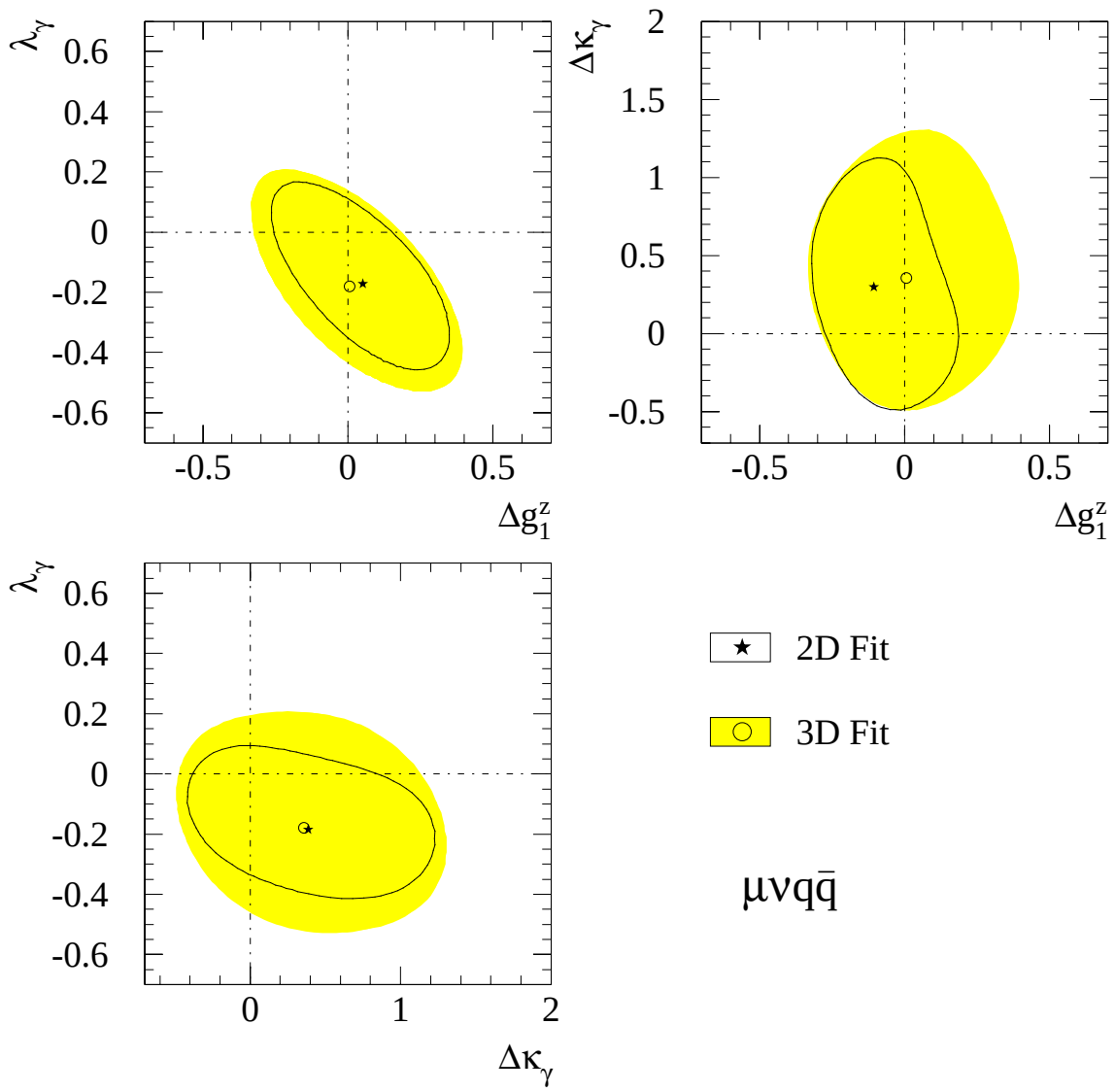

Figure 6.8: Multi-dimensional fit results for the $\mu\nu q\bar{q}$ channel. The 95% CL contours resulting from the two-dimensional fit are plotted as an open area. The shaded contours correspond to the two-dimensional projections of the 95% CL contour resulting from the three dimensional fit. Both the total cross section and angular information are used in the fits. The systematic uncertainties are included.

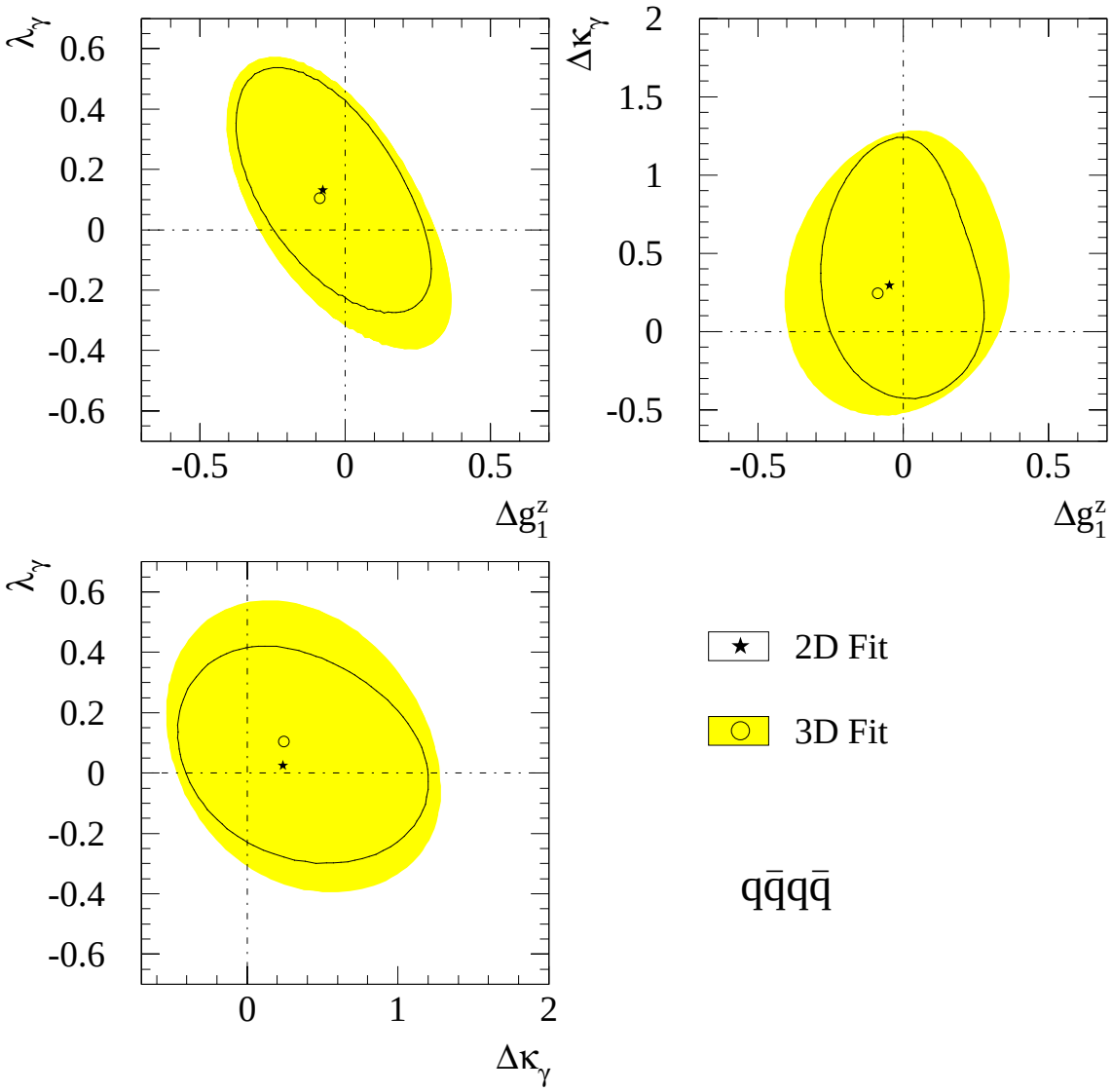

Figure 6.9: Multi-dimensional fit results for the $q\bar{q}q\bar{q}$ channel. The 95% CL contours resulting from the two-dimensional fit are plotted as an open area. The shaded contours correspond to the two-dimensional projections of the 95% CL contour resulting from the three dimensional fit. Both the total cross section and angular information are used in the fits. The systematic uncertainties are included.

6.2.2 Combination

The TGCs are also extracted by combining the information of the three WW decay channels studied in this analysis. The combined results are obtained by means of least squares fits in which all the relevant measurements from the three channels are included. Those systematic errors affecting to more than one channel and/or observable are considered to be 100% correlated in the fit.

The one-dimensional fit results are listed in Table 6.4 and the corresponding χ^2 curves are plotted in Fig. 6.10.

	Δg_1^Z	$\Delta\kappa_\gamma$	λ_γ
$\frac{d\sigma}{d\Omega}$	$-0.037^{+0.065}_{-0.062}$	$0.141^{+0.240}_{-0.200}$	$-0.068^{+0.069}_{-0.066}$
$\sigma_T + \frac{d\sigma}{d\Omega}$	$-0.023^{+0.057}_{-0.055}$	$0.253^{+0.202}_{-0.177}$	$-0.042^{+0.062}_{-0.059}$
Including Syst.	$-0.036^{+0.061}_{-0.059}$	$0.203^{+0.222}_{-0.189}$	$-0.060^{+0.066}_{-0.063}$

Table 6.4: One-dimensional fit results for the three channels combination.

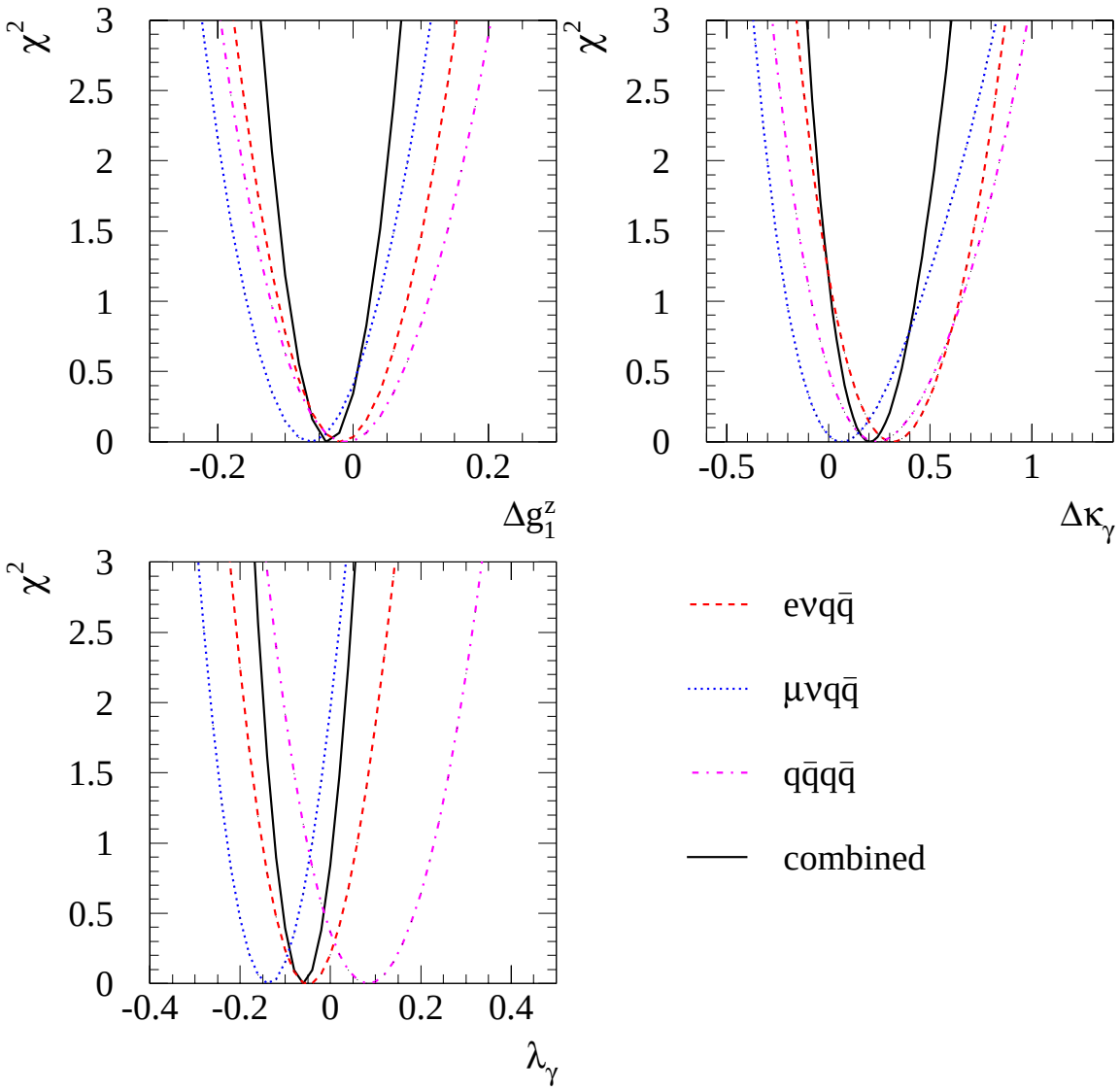

Figure 6.10: χ^2 curves corresponding to the one-dimensional fits for each single channel and their combination. Both the cross section and the angular information are used in the fit. The systematic uncertainties are included.

The three channels information is also combined in two- and three-dimensional fits. The 95% CL intervals obtained are listed in Table 6.5 and the corresponding 95% contours and two-dimensional contour projections are shown in Fig. 6.11.

	Δg_1^Z	$\Delta\kappa_\gamma$	λ_γ
	$[-0.181, 0.064]$	$[-0.101, 0.729]$	–
2D	–	$[-0.056, 0.773]$	$[-0.232, 0.034]$
	$[-0.144, 0.158]$	–	$[-0.223, 0.104]$
3D	$[-0.164, 0.15]$	$[-0.06, 0.764]$	$[-0.258, 0.081]$

Table 6.5: Multi-dimensional fit 95% CL results for the three channels combination.

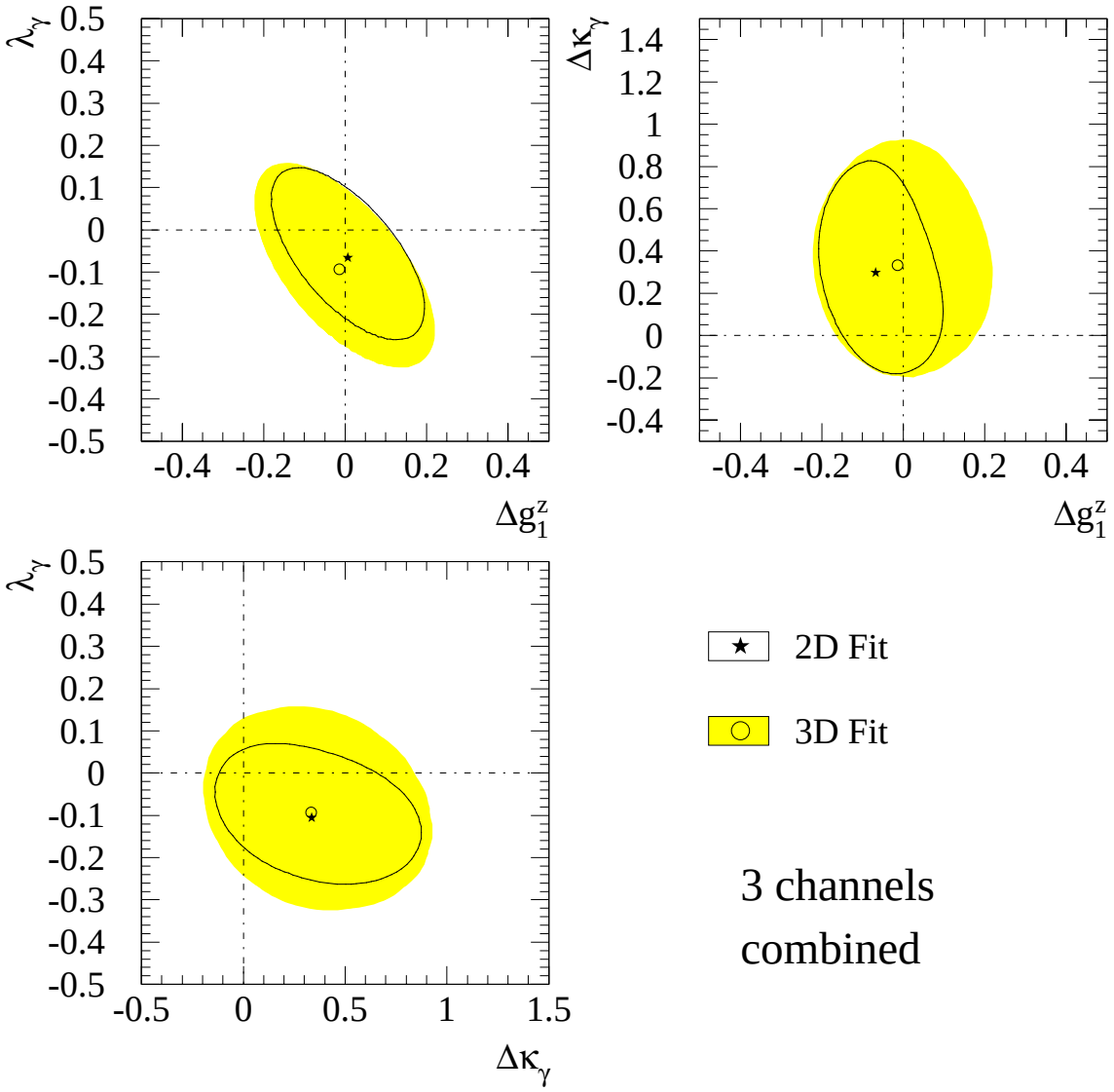

Figure 6.11: Multi-dimensional fit results for the three channels combination. The 95% CL contours resulting from the two-dimensional fit are plotted as an open area. The shaded contours correspond to the two-dimensional projections of the 95% CL contour resulting from the three dimensional fit. Both the total cross section and angular information are used in the fits. The systematic uncertainties are included.

6.3 TGC measurement at LEP

The TGCs have been extracted at $\sqrt{s} = 189$ GeV by the four LEP experiments. By the time of writing this work, only preliminary results exist which have been presented in conferences [60, 61, 62]. In Fig. 6.12, the one-dimensional TGC results obtained in this thesis (quoted as ALEPH in the plot) are compared with similar measurements carried out by the DELPHI, L3 and OPAL experiments. From the L3 experiment, only results for the semileptonic channel are shown which have been obtained from [63], as the results quoted in [61] combine the information from all the decay channels. In the results shown from the OPAL experiment, only the angular information is included, as the numbers containing cross section information quoted in [62] combine as well the data from previous years. All the numbers shown in Fig. 6.12 include systematic errors.

None of the four LEP experiments has observed any deviation from the SM TGC predictions in the 189 GeV data. It should be noticed that the sensitivities reached by the different analysis are very similar, as expected, since in all of them the information in the angular distributions is exploited through optimal observable techniques.

The $\Delta\kappa_\gamma$ and λ_γ couplings extracted by the D0 experiment [64] at Tevatron using approximately 100 pb^{-1} of integrated luminosity are also shown in Fig. 6.12. The D0 limits are obtained by performing a simultaneous fit to the data samples from three different di-boson final states: Wγ, WW and WZ production. As it can be seen from the figure, the precision achieved by each of the LEP experiments, once the information from the different decay channels is combined, is better than that of D0.

During the year 1999, LEP operated at centre of mass energies between 192 and 202 GeV. Very preliminary results have been obtained by the four LEP experiments for the data taken at these energies. The combination of TGC results based on the data collected by the four LEP experiments at LEP2 until the end of 1999 has been presented in different conferences during year 2000 [65]. The combination of the three-dimensional fit results yields:

$$\begin{aligned} \Delta g_1^Z &= -0.003^{+0.039}_{-0.036} \\ \Delta\kappa_\gamma &= +0.017^{+0.074}_{-0.071} \\ \lambda_\gamma &= -0.066^{+0.042}_{-0.045} \end{aligned} \tag{6.4}$$

where the quoted errors represent the 68.3% confidence level. No deviation from the SM predictions is seen for any of the combined TGCs.

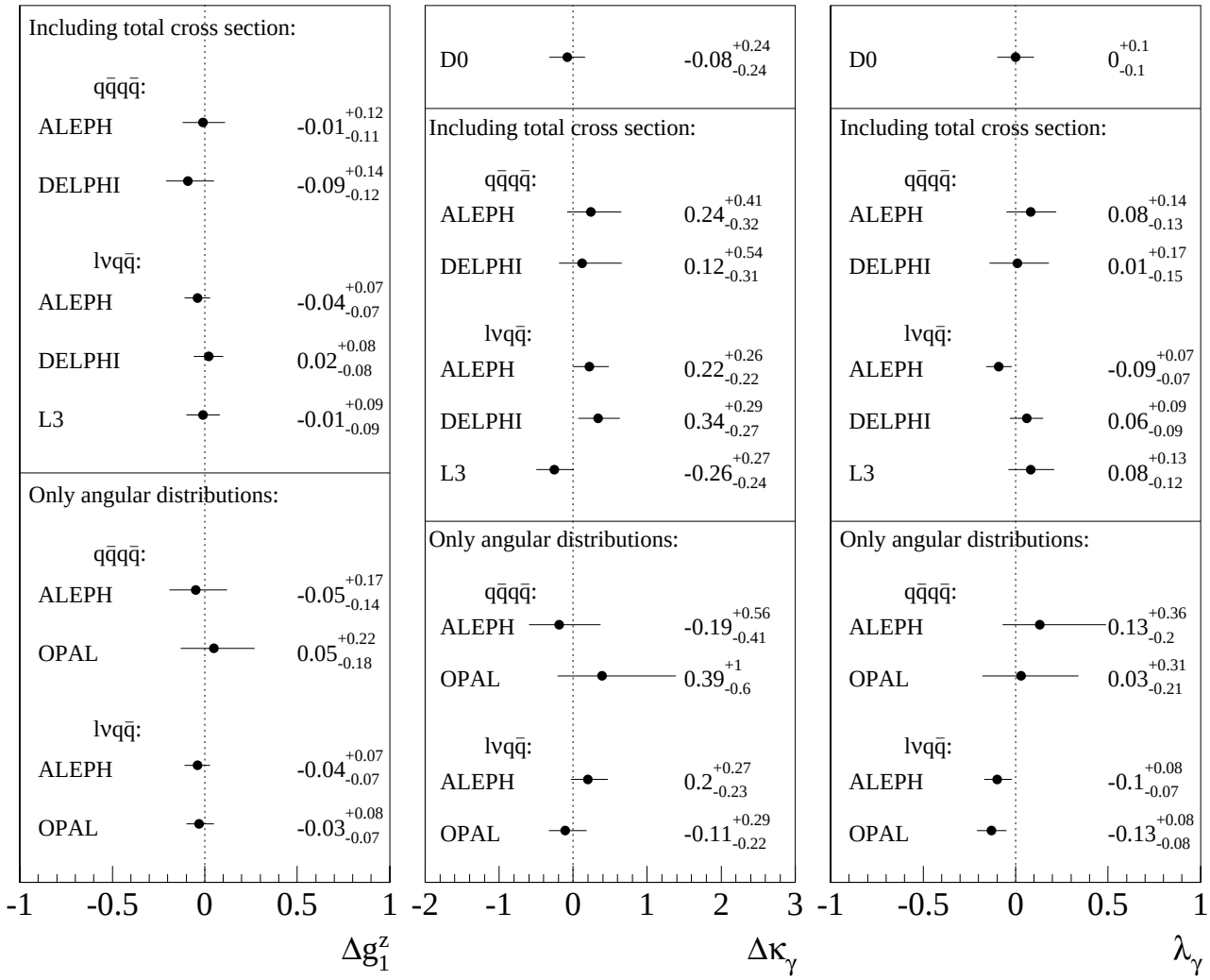

Figure 6.12: Comparison of the one-dimensional fit results obtained by the LEP collaborations using the semileptonic and purely hadronic WW decay channels at $\sqrt{s} = 189$ GeV. The D0 results for $\Delta\kappa_\gamma$ and λ_γ are also shown.

Chapter 7

Summary and conclusions

A test of the non-abelian gauge structure of the SM electroweak sector is performed by studying the ZWW and γWW triple gauge boson vertices. using $e^+e^- \to W^-W^+$ events. To do so, the strength of this vertex is parameterised in terms of three couplings: Δg_1^Z, $\Delta\kappa_\gamma$ and λ_γ, referred to as the TGCs, whose tree level value in the SM is zero.

A measurement of the TGCs using the purely hadronic and the electron and muon semileptonic W pair decay channels from the data sample collected by the ALEPH detector during the year 1998 at a centre of mass energy of 188.6 GeV is presented.

The total W pair cross section can be expressed as a quadratic function of the TGCs, hence the measurement of the event rate in each channel can be translated into a TGCs confidence interval.

The polynomial dependence of the differential cross section on the TGCs allows the multi-dimensional information in the WW decay product kinematics to be projected into one-dimensional distributions by defining a set of optimal observables. The mean values of such observables are used to extract the couplings since, in the limit of vanishing couplings, they contain the information of the full distribution. The optimal observable mean value predictions as a function of the TGCs are obtained from a reference Monte Carlo event sample generated with SM couplings which is reweighted to any other TGC values with the ratio of the squared matrix elements.

The cross section information is combined with that of the measured optimal observable mean values to extract the TGCs from every studied channel by performing one-, two- and three-dimensional fits where those couplings which are not fitted are fixed to their SM value in every case. Finally, the most restrictive TGC confidence intervals are

obtained by combining the information from the three channels.

No deviation from the SM predictions is seen for any of the measured TGCs. The results obtained in this thesis are going to be combined with those from $e^+e^- \to W^+W^- \to \tau\nu q\bar{q}/\ell^+\nu\ell^-\bar{\nu}$, $e^+e^- \to \nu\bar{\nu}\gamma$ and $e^+e^- \to \mathrm{We}\nu_e$ in an ALEPH paper which is in preparation at the time of writing this work.

Appendix A

Systematics affecting $\langle \mathcal{O} \rangle$

As detailed in Chapter 4, when extracting the TGCs from the information contained in the angular distributions of the WW decay products, the measured mean values of a series of optimal observables are compared to their theoretical predictions, which are function of the couplings. These predictions are obtained from a reference sample of Monte Carlo events. From these events, those corresponding to the signal are reweighted with the squared matrix elements ratio in order to mimic the behaviour of a sample of events generated with non-vanishing couplings. On the other hand, the background events in the reference Monte Carlo sample have also a certain weight, which is in general different from one, so that they correspond to the same integrated luminosity as the signal sample. Therefore, the optimal observable mean values theoretical prediction takes the form of a weighted average

$$\langle \mathcal{O} \rangle = \frac{\sum_{i=1}^{N_s} \omega_s(\vec{\Omega}_i|\vec{g})\mathcal{O}_i + \sum_{b=1}^{n_{bcks}} \sum_{j=1}^{N_b} \omega_b \mathcal{O}_j}{\sum_{i=1}^{N_s} \omega_s(\vec{\Omega}_i|\vec{g}) + \sum_{b=1}^{n_{bcks}} \sum_{j=1}^{N_b} \omega_b} , \tag{A.1}$$

where N_s stands for the number of signal events, n_{bcks} for the number of background types considered, and N_b the number of events of a certain background type. As indicated in (A.1), the signal event weights ω_s depend on both the event kinematics $\vec{\Omega}_i$ and the TGCs value $\vec{g}$ where the sample is being reweighted to. The background weights ω_b instead, depend only on the background type and provide the proper internormalisation among processes, therefore being

$$\omega_b = \frac{\mathcal{L}_s}{\mathcal{L}_b} = \frac{\sigma_b}{N_b^{gen}} \frac{N_s^{gen}}{\sigma_s} . \tag{A.2}$$

The theoretical uncertainties in the signal and background processes cross sections discussed in Sect. 6.1.3 are therefore introducing a systematic error in the determination of the background weights $\delta\omega_b$ such that

$$\left(\frac{\delta\omega_b}{\omega_b}\right)^2 = \left(\frac{\delta\sigma_b}{\sigma_b}\right)^2 + \left(\frac{\delta\sigma_s}{\sigma_s}\right)^2 \tag{A.3}$$

which can then be translated into an uncertainty in the optimal observable mean value theoretical predictions

$$\delta\langle\mathcal{O}\rangle^2 = \sum_{b=1}^{n_{bcks}} \left(\frac{\partial\langle\mathcal{O}\rangle}{\partial\omega_b}\right)^2 \delta\omega_b^2 \,. \tag{A.4}$$

Appendix B

Variance of a weighted average

Let us assume we have a sample of N measurements of a certain observable $\{\mathcal{O}_i \ ; \ i = 1, N\}$ and we are measuring its average

$$\langle \mathcal{O} \rangle = \frac{\sum_{i=1}^{N} \mathcal{O}_i}{N} \tag{B.1}$$

where we first consider that every event has weight one, for simplicity. If we are now interested in knowing what is the variance of this average $\langle \mathcal{O} \rangle$, we can make use of the *bootstrapping* procedure to do this. We start out with our particular data set $\{\mathcal{O}_i \ ; \ i = 1, N\}$, from this we can create a large number of comparable *pseudo-data sets* (the bootstrap operation) by picking N events from the data sample with *replacement*, meaning that every event has the same probability $1/N$ of getting picked every time. From each of these pseudo-data sets the average $\langle \mathcal{O} \rangle$ can be computed, so a collection of averages can be readily obtained which can be viewed as

$$\langle \mathcal{O} \rangle = \frac{\sum_{i=1}^{N} k_i \, \mathcal{O}_i}{\sum_{i=1}^{N} k_i} \tag{B.2}$$

where $\{k_i \ ; \ i = 1, N\}$ is a collection of N Poisson distributed numbers with average one so that

$$\langle k_i \rangle = V(k_i) = 1 \ , \tag{B.3}$$

$$\sum_{i=1}^{N} k_i = N \ . \tag{B.4}$$

The variance of (B.2) can be now computed by considering k_i as the random variable instead of $\mathcal{O}_i$

$$V(\langle \mathcal{O} \rangle) = \sum_{j=1}^{N} \left(\frac{\partial \langle \mathcal{O} \rangle}{\partial k_j} \right)^2 V(k_j) = \frac{1}{N} \sum_{j=1}^{N} (\mathcal{O}_j - \langle \mathcal{O} \rangle)^2 \ , \tag{B.5}$$

so that the well known expression for the variance of an average is recovered.

If a certain weight ω_i is assigned to each event, the average (B.2) is transformed into a *weighted average* which can be read as

$$\langle \mathcal{O} \rangle = \frac{\sum_{i=1}^{N} k_i \, \omega_i \mathcal{O}_i}{\sum_{i=1}^{N} k_i \, \omega_i} \, . \tag{B.6}$$

The variance of (B.6) can be now computed as done in (B.5)

$$\begin{aligned} V(\langle \mathcal{O} \rangle) &= \sum_{j=1}^{N} \left(\frac{\partial \langle \mathcal{O} \rangle}{\partial k_j} \right)^2 V(k_j) = \sum_{j=1}^{N} \frac{\omega_j^2}{(\sum_{i=1}^{N} \omega_i)^2} \, (\mathcal{O}_j - \langle \mathcal{O} \rangle)^2 \\ &= \frac{1}{N_{eq}} \sum_{j=1}^{N} \frac{\omega_j^2}{\sum_{i=1}^{N} \omega_i^2} \, (\mathcal{O}_j - \langle \mathcal{O} \rangle)^2 \end{aligned} \tag{B.7}$$

where N_{eq} is the so-called *equivalent number of events*, as defined in [66]

$$N_{eq} = \frac{(\sum_{i=1}^{N} \omega_i)^2}{\sum_{i=1}^{N} \omega_i^2} \, , \tag{B.8}$$

which corresponds to the number of *unweighted* events which have the same statistical significance as the N *weighted* events, so that

$$\frac{\delta(\sum_{i=1}^{N} \omega_i)}{\sum_{i=1}^{N} \omega_i} \equiv \frac{\delta N_{eq}}{N_{eq}} = \frac{1}{\sqrt{N_{eq}}} \tag{B.9}$$

It is worth to note from (B.7) that the variance of a weighted average is not readily obtained just by substituting N by N_{eq} at (B.5), as one might be temptated to do. This is illustrated in Fig. B.1, where the variance of the weighted average $\langle \mathcal{O}_{1,\Delta g_1^Z} \rangle$ for $\mu\nu q\bar{q}$ events is plotted versus the Δg_1^Z coupling value where the Monte Carlo events are reweighted to. The dots with error bars in the Figure represent the RMS of the weighted average distributions, as computed from several Monte Carlo event samples. To compute each RMS in Fig. B.1, the same Monte Carlo events have been used, reweighted to different Δg_1^Z values, therefore the errors shown are correlated.

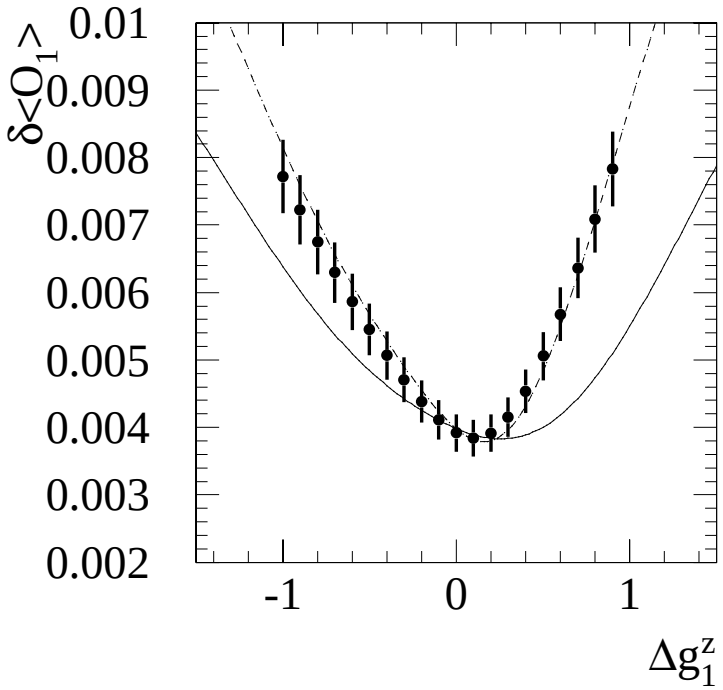

Figure B.1: The variance of the weighted average $\langle \mathcal{O}_{1,\Delta g_1^Z} \rangle$ for 20000 Monte Carlo $\mu\nu q\bar{q}$ events as a function of the Δg_1^Z coupling value where the events have been reweighted to. The dashed line corresponds to the expression (B.7) while the solid line prediction is computed as $V(\langle \mathcal{O} \rangle) = \sum_{j=1}^{N} (\mathcal{O}_j - \langle \mathcal{O} \rangle)^2 / N_{eq}$. The dots represent the actual $\langle \mathcal{O}_{1,\Delta g_1^Z} \rangle$ variance, and are computed as the RMS of the weighted average $\langle \mathcal{O}_{1,\Delta g_1^Z} \rangle$ values measured from several samples.

Bibliography

[1] S.L. Glashow, Nucl. Phys. **B22** (1961) 579;
S. Weinberg, Phys. Rev. Lett. **19** (1967) 1264;
A. Salam, *Elementary Particle Theory*, ed. N. Svartholm, Almqvist and Wiksell, Stockholm (1968) 367;
S.L. Glashow, J. Iliopoulos and L. Maiani, Phys. Rev. **D2** (1970) 1285.

[2] H. Fritzsch and M. Gell-Mann, Proc. XvI Int. Conf. on High Energy Physics, eds. J.D. Jackson and A. Roberts (Fermilab 1972).

[3] G.'t Hooft, Nucl. Phys. **B33** (1971) 173.

[4] The LEP Collaborations, the LEP Electroweak Working Group and the SLD Heavy Flavour and Electroweak Groups, *A combination of preliminary electroweak measurements and constraints on the Standard Model*, CERN-EP-2000-016, January 21, 2000.

[5] M. Bilenky, J.L. Kneur, F.M. Renard and D. Schildknecht, Nucl. Phys. **B409** (1993) 22.

[6] C. Caso *et al.*, Eur. Phys. J. **C3** (1998) 1.
Partial update for the 2000 edition available at `http://pdg.lbl.gov`

[7] T. Muta, R. Najima and S. Wakaizumi, Mod. Phys. Lett. **A1** (1986) 203.

[8] D. Bardin *et al.*, in *Physics at LEP200 and Beyond*, eds. J. Blümlein and T. Riemann (North-Holland, Amsterdam, 1994), p. 148.

[9] W. Beenakher, in e^+e^- *Collisions at 500 GeV: The Physics Potential*, ed. P.M. Zerwas (DESY 92-123, Hamburg, 1992), part A, p. 195.

[10] F.A. Berends, R. Pittau, R. Kleiss, Nucl. Phys. **B426** (1994) 344.

[11] V.S.Fadin, V.A.Khoze, A.D.Martin, Phys. Lett.B31193311;
D.Bardin, W.Beenakker, A.Denner, Phys. Lett.B31793213;
A.Chapovsky, V.S.Fadin, V.A.Khoze, A.D.Martin, Phys. Rev.D52951377.

[12] *Z Physics at LEP 1*, G. Altarelli, R. Kleiss and C. Verzegnassi eds., CERN 89-08 (1989), Vol. 1.

[13] M. Böhm, A. Denner and S. Dittmaier, Nucl. Phys. **B376** (1992) 29; Erratum: Nucl. Phys. **B391** (1993) 483.

[14] J. Fleischer, F. Jegerlehner and M. Zralek, Z. Phys. **C42** (1989) 409;
F. Jegerlehner in *Radiative corrections: Results and Perspectives*, eds. N. Dombey and F. Boudjema, NATO ASI Series, Plenum Press, New York (1990), p. 185.

[15] D. Bardin *et al.*, Comput. Phys. Commun. **104** (1997) 161.
`GENTLE` is available at `http://www.ifh.de/theory/publist.html`

[16] T. Sjöstrand and V. A. Khoze, Z. Phys. **C62** (1994) 281, Phys. Rev. Lett. **72** (1994) 28, CERN-TH/98-74 (hep-ph/9804202).

[17] G.Gustafson and J.Häkkinen, Z. Phys. **C64** (1994) 659.
L. Lönnblad, Z. Phys. **C70** (1996) 107.
Š. Todorova–Nová, DELPHI Internal Note 96-158 PHYS 651.
J. Ellis and K. Geiger, Phys. Rev. **D54** (1996) 1967, Phys. Lett. **B404** (1997) 230.
B.R. Webber, J. Phys. **G24** (1998) 287.

[18] S. Jadach and K. Zalewski, *W mass Reconstruction from Hadronic Events in LEP2: Bose-Einstein effect*, CERN-TH/97-29, February 1997.

[19] L. Lönnblad and T. Sjöstrand, *Modelling Bose-Einstein correlations at LEP2*, Eur. Phys. J. **C2** (1998) 165.

[20] S. Myers and E. Picasso. *The design, construction and comissioning of the CERN Large Electron Positron collider.* Contemporary Physics **31** (1990) 387.

[21] Lep Design Report, vol. 1: *The LEP Injector Chain.* CERN-LEP/83-29 (1983);
Lep Design Report, vol. 2: *The LEP Design Report.* CERN-LEP/84-01 (1984).

[22] D. Decamp *et al.* (ALEPH Collaboration). *ALEPH: a detector for electron-positron annihilations at LEP.* Nucl. Inst. and Meth. **A294** (1990) 121.

[23] D. Buskulic *et al.* (ALEPH Collaboration). *Performance of the ALEPH detector at LEP*. Nucl. Inst. and Meth. **A360** (1995) 481.

[24] C. Bowdery, ed. (ALEPH Collaboration). *The ALEPH Handbook*, vol. 1 (1995); vol. 2 (1997). Published by CERN.

[25] R. Frühwirth, HEPHY-PUB 503/87 (1987).

[26] Working Group on the TGCs determination, in *Physics at LEP2*, G. Altarelli, T. Sjöstrand and F. Zwirner eds., CERN 96-01 (1996), Vol. 1, 525.

[27] M. Davier, L. Duflot, F. Le Diberder and A. Rougé. Phys. Lett. **B306** (1993) 411.

[28] M. Diehl and O. Nachtmann, Z. Phys. **C62** (1994) 397.

[29] G. K. Fanourakis, D. Fassouliotis and S. E. Tzamarias, Nucl. Inst. and Meth. **A412** (1998) 465; Nucl. Inst. and Meth. **A414** (1998) 339.

[30] M. Diehl and O. Nachtmann, hep-ph/9702208

[31] M. Skrzypek, S. Jadach, W. Placzek and Z. Wąs, Comput. Phys. Commun. **94** (1996) 216.

[32] M. Skrzypek *et al.*, Phys. Lett. **B372** (996) 289.

[33] MINAMI-TATEYA group. *GRACE Manual: Automatic generation of tree amplitudes in Strandard Models: Version 1.0*. KEK report 92-19 (1993).

[34] E. Barberio and Z. Wąs, Comput. Phys. Commun. **79** (1994) 291.

[35] T. Sjöstrand, Comput. Phys. Commun. **82** (1994) 74.

[36] ALEPH Collaboration, Phys. Lett. **B313** (1993) 509.

[37] S. Jadach, B.F.L. Ward and Z. Wąs, Comput. Phys. Commun. **79** (1994) 466.

[38] S. Jadach et al.,"Event Generators for Bhabha Scattering", in *Physics at LEP2*, eds. G. Altarelli, T. Sjöstrand, F. Zwirner, Yellow Report CERN 96-01 (1996), Vol. 2, 229; e-Print Archive: hep-ph/9602393.

[39] S. Dhamotharan, *Study of the triple gauge-boson vertex in W-pair production at LEP2*, PhD thesis, Rupertus Carola University of Heidelberg, 1999.

[40] N. Brown and W.J. Stirling, Phys. Lett. **B252** (1990) 657.

[41] Working Group on QCD, in *Z Physics at LEP 1*, G. Altarelli, R. Kleiss and C. Verzegnassi eds., CERN 89-08 (1989), vol.1, 373.

[42] P. Azzurri, ALEPH Note 96-137 PHYSIC 96-125 (1996).

[43] A. Rougé, ALEPH Note 94-057 PHYSIC 94-051 (1994).

[44] C. Batagnani, G. Calderini, J.P. Lees and M. Maggi, ALEPH Note 93-095 SOFTWR 93-078 (1993).

[45] ALEPH Collaboration, *Measurement of the W mass in e^+e^- collisions at production threshold*, Phys. Lett. **B401** (1997) 347.

[46] T. Sjöstrand, *PYTHIA 5.7 and JETSET 7.4 Physics and Manual*, hep-ph/9508391.

[47] G. Guicheney *et al.*, ALEPH Note 98-078 PHYSIC 98-031 (1998), `http://alephwww.cern.ch/~guichene/ww_tools/qnnwtag.html`.

[48] ALEPH Collaboration, *Measurement of the W mass by Direct Reconstruction in e^+e^- collisions at 172 GeV*, Phys. Lett. **B422** (1998) 384.

[49] ALEPH Collaboration,*Measurement of W-pair production in e^+e^- collisions at 189 GeV*, ALEPH Note 99-064 CONF 99-038.

[50] W. Beenakker, F. A. Berends and A. P. Chapowsky, Nucl. Phys. **B548** (1999) 3.

[51] S. Jadach, W. Placzek, M. Skrzypek, B.F.L. Ward and Z. Was, Phys. Lett. **B417** (1998) 326. CERN-TH/99-222, UTHEP-98-0502.

[52] A. Denner, S. Dittmaier, M. Roth and D. Wackeroth, *$\mathcal{O}(\alpha)$ corrections to $e^+e^- \to WW \to 4\ fermions(+\gamma)$: first numerical results from RacoonWW*, BI-TP 99/45, hep-ph/9912261 (1999).

[53] ALEPH Collaboration,*Measurement of W-pair production and W branching ratios in e^+e^- collisions at $\sqrt{s}$ = 192 to 202 GeV*, ALEPH Note 2000-005 CONF 2000-002.

[54] LEP energy working group, *Evaluation of the LEP centre-of-mass energy above the WW production threshold*, CERN-EP/98-191, submitted to Eur. Phys. J. **C**.

[55] A. Straessner, talk given at the *XXXV Rencontres de Moriond*, March 2000.

[56] G. Marchesini *et al.*, Comput. Phys. Commun. **67** (1992) 465.

[57] ALEPH Collaboration, *Measurement of the W Mass and Width in e+e- Collisions at 189 GeV*, CERN EP/2000-045, submitted to Eur. Phys. J. **C**.

[58] ALEPH Collaboration. *Bose-Einstein correlations in W-pair decays*, CERN-EP/99-173, submitted to Phys. Lett. **B**.

[59] W. Beenaler *et al.*, in *Physics at LEP2*, G. Altarelli, T. Sjöstrand and F. Zwirner eds., CERN 96-01 (1996), Vol.1, 525.

[60] DELPHI Collaboration, *Measurement of Trilinear Gauge Boson Couplings in e^+e^- Collisions at 189 GeV*, DELPHI 99-63 CONF 250 (1999).

[61] L3 Collaboration, *Preliminary Results on the Measurement of Triple-Gauge-Boson Couplings of the W boson at LEP*, L3 Note 2378 (1999).

[62] OPAL Collaboration, *Measurement of triple gauge boson couplings from* W^+W^- *production at LEP energies up to 189 GeV*, OPAL Physics Note PN425 (2000).

[63] C. Palomares, *Estudio del Proceso $e^+e^- \to W^+W^- \to \ell\nu q\bar{q}$ en LEP*, PhD thesis, Universidad Autónoma de Madrid, 1999.

[64] ALEPH, DELPHI, L3, OPAL and D0 TGC Combination Group, *A Combination of Preliminary Measurements of Triple Gauge Boson Coupling Parameters Measured by the LEP and D0 Experiments*, LEPEWWG/TGC/98-02 (1998).

[65] ALEPH, DELPHI, L3, OPAL and the LEP TGC Working Group, *A Combination of Preliminary Results on Triple Gauge Boson Couplings Measured by the LEP Experiments*, LEPEWWG/TGC/2000-02 (2000).

[66] G. Zech, *Comparing Statistical Data to Monte Carlo Simulation - Parameter Fitting and Undfolding*, DESY 95-113 June 1995.